

# POLITECNICO DI TORINO

Collegio di Ingegneria Chimica e dei Materiali

**Master of Science Course  
in Materials Engineering**

Master of Science Thesis

**Synthesis and characterization of Iron-doped hydroxyapatite nanoparticles with  
superparamagnetic behaviour.**



## **Tutors**

*Signature of the Tutors*

João Paulo Borges  
Enrica Vernè

## **Candidate**

*Signature of the candidate*

Fabio Mesturino

September 2018



## Summary

Sommario italiano .....	I
1. <i>Introduzione</i> .....	I
2. <i>Procedura sperimentale e risultati</i> .....	II
Abstract .....	VIII
Introduction .....	IX
1 Theoretical background.....	1
1.1 <i>Bone</i> .....	1
1.2 <i>Hydroxyapatite</i> .....	3
1.3 <i>Synthesis method: panorama</i> .....	4
1.4 <i>Sol-gel process</i> .....	7
1.5 <i>Nanometer size</i> .....	9
1.6 <i>Magnetism, general introduction</i> .....	10
1.7 <i>Super-paramagnetism</i> .....	14
1.8 <i>Magnetic hyperthermia</i> .....	19
1.9 <i>Iron doped Hydroxyapatite: state of art</i> .....	22
2 Materials and methods .....	29
2.1 <i>Fe – doped hydroxyapatite synthesis</i> .....	29
2.1.1 <i>Synthesis precursors</i> .....	29
2.1.2 <i>Experimental procedure</i> .....	30
2.2 <i>Characterization technique</i> .....	31
2.2.1 <i>X-Ray diffraction</i> .....	31
2.2.2 <i>Fourier transformed infrared spectroscopy (FTIR)</i> .....	32
2.2.5 <i>Vibrating sample magnetometer (VSM)</i> .....	34
2.2.6 <i>Magnetic hyperthermia analysis</i> .....	34
2.2.7 <i>Bioactivity test</i> .....	35
2.2.8 <i>Citotoxicity test</i> .....	36
3. Results and discussion .....	41
3.1 <i>Visual characterisation</i> .....	41
3.2 <i>X-Ray analysis (XRD)</i> .....	41
3.2.1 <i>Crystallinity</i> .....	45
3.2.2 <i>Crystallite diameter</i> .....	46
3.2.3 <i>Cell parameters</i> .....	47
3.2.4 <i>Phase percentage HAp/<math>\beta</math>-TCP</i> .....	50
3.3 <i>FTIR analysis</i> .....	50
3.4 <i>Vibrating Sample Magnetometer (VSM) analysis</i> .....	54
3.4 <i>Magnetic thermal hyperthermia</i> .....	60

3.5 <i>Bioactivity test</i> .....	61
3.6 <i>Cytotoxicity test</i> .....	75
4. Conclusions.....	77
Bibliography.....	79

## Sommario italiano

### *1. Introduzione*

Il cancro è considerata la malattia causa del maggiore numero di morti nella società moderna. Il numero di soggetti affetti è in aumento ogni anno, mostrandosi come uno dei problemi più seri della medicina moderna. Potendosi presentare sotto molte forme diverse ed in diverse aree del corpo umano, il suo trattamento si dimostra sempre essere molto complicato. In questo senso, giocano ruolo fondamentale la prevenzione (che purtroppo spesso non risulta sufficiente) e l'individuazione di cellule cancerogene all'interno dell'organismo. Per questo motivo, l'ingegneria lavora da tempo con l'obiettivo di migliorare la sensibilità dei macchinari utilizzati per la diagnosi. Inoltre, fondamentale è anche lo sviluppo di trattamenti, materiali e nuovi macchinari che consentano di trattare ed eliminare le cellule tumorali nelle più diverse forme.

Questo progetto di tesi è pertanto focalizzato sullo sviluppo di una tecnologia innovativa, economica e biocompatibile utilizzabile per il trattamento del cancro osseo. Quest'ultimo è una tipologia di tumore che può avere due tipologie differenti di sviluppo: può essere infatti direttamente sviluppato sull'osso malato oppure può essere un focolaio secondario determinato dalla propagazione di un'altra tipologia di tumore, per esempio ai polmoni.

Per il trattamento di alcune tipologie di tumori (compresi quello osseo) è utilizzata la tecnica dell'ipertermia magnetica. Essa consiste nel determinare il riscaldamento di un corpo previamente inserito a diretto contatto con il tumore all'interno dell'organismo fino alla temperatura di poco superiore a 42°C. Infatti, a questa temperatura i processi enzimatici che mantengono viva la cellula smettono di funzionare, portando alla morte della stessa. Le cellule sane, sono in grado di sopportare questa temperatura molto meglio e più a lungo delle cellule malate e questo ha come conseguenza l'eliminazione selettiva delle sole cellule tumorali quando sottoposte a temperature elevate. Per questa tipologia di trattamento sono utilizzate nanoparticelle di materiali superparamagnetici, in grado di determinare l'aumento desiderato di temperatura rapidamente in presenza di un campo magnetico. Un materiale super-paramagnetico infatti presenta la peculiarità di aumentare rapidamente di temperatura quando sottoposto ad un campo magnetico esterno e a smagnetizzarsi altrettanto rapidamente fino ad uno stadio non magnetizzato quando il campo viene rimosso. Quest'ultima proprietà risulta altrettanto fondamentale, infatti una non magnetizzazione delle particelle porta a ridurre il rischio di agglomerazione delle stesse, salvaguardando l'organismo da spiacevoli e pericolose conseguenze.

Storicamente, le più utilizzate sono le nanoparticelle di ossido di ferro, in grado di mostrare comportamento super-paramagnetico quando la granulometria è sufficientemente piccola.

Esse però sono materiali non biocompatibili e pertanto non la scelta ottimale per l'applicazione all'interno del corpo, avendo limitazioni sulla permanenza nell'organismo e le quantità introdotte. Per questa ragione, negli ultimi anni la ricerca si sta orientando verso l'utilizzo di altre tipologie di materiali, superparamagnetici e biocompatibili.

In questo senso, di grande interesse e conseguentemente molto investigato al giorno d'oggi è il caso dell'idrossiapatite dopata con ferro. Infatti, questa tipologia di materiali è in grado di mostrare comportamento super-paramagnetico accompagnato da ottima biocompatibilità dovuto alla struttura del minerale, lo stesso che compone le ossa del corpo umano.

In letteratura sono presenti varie investigazioni a riguardo di questa tipologia di materiale, che può essere sintetizzato con processi differenti. Tra questi, il più utilizzato è sicuramente la precipitazione o una sua variante la co-precipitazione. Questo processo presenta un certo grado di difficoltà dovuto alla grande quantità di parametri differenti che possono influenzare il risultato ed è di difficile conduzione. È pertanto un processo costoso ed elaborato e richiede la presenza di operatori esperti per avere un risultato il più possibile vicino a quello inizialmente programmato.

Obiettivo di questa tesi è appunto realizzare la sintesi di idrossiapatite dopata con ferro, utilizzando il processo sol-gel per la sintesi. Esso infatti presenta parametri più facilmente controllabili nonché un processo più economico e di facile attuazione.

In questo progetto vengono pertanto sintetizzate ed analizzate nanoparticelle di idrossiapatite dopata con ferro. Per la sintesi sono utilizzate due diverse quantità di precursori di ferro che determinano due differenti composizioni per ciò che riguarda la quantità di ioni sostituenti nel reticolo dell'idrossiapatite.

Inoltre, entrambe le tipologie di campioni vengono trattate termicamente (con conseguente parziale sinterizzazione delle polveri) alle temperature di 600°C, 700°C e 800°C.

I risultati principali del progetto sono brevemente trattati in seguito. Quando ritenuto necessario, saranno accompagnati da una trattazione teorica, di modo da comprendere al meglio l'argomento.

## 2. Procedura sperimentale e risultati

Il materiale analizzato viene sintetizzato seguendo il normale processo di sintesi sol-gel normalmente applicato per la produzione di standard idrossiapatite, adattato di modo da ottenere il dopaggio desiderato.

In fig. 2.1 è riportato un esempio del generale processo sol-gel.

I precursori utilizzati per il processo sono calcio nitrato tetraidrato ( $\text{Ca}(\text{NO}_3)_2 \cdot 4\text{H}_2\text{O}$ , *Panreac*), pentossido di fosforo ( $\text{P}_2\text{O}_5$ , *Sigma - Aldrich*), cloruro di ferro(II) tetraidrato ( $\text{FeCl}_2 \cdot 4\text{H}_2\text{O}$ , *Sigma-Aldrich*) e cloruro di ferro(III) esaidrato ( $\text{FeCl}_3 \cdot 6\text{H}_2\text{O}$ , *Sigma-Aldrich*).

Questi ultimi due sono responsabili del dopaggio del materiale finale e per questo motivo la loro quantità viene pesata con cura. In particolare, in tabella 2.2 è riportato la quantità scelta per ambo le due composizioni considerate. Queste risultano in differenti valori del rapporto tra ioni positivi e ioni negativi ( $\text{Ca}^{2+} + \text{Fe}^{3+} + \text{Fe}^{2+} / \text{P}$ ) nelle polveri realizzate. Questo rapporto è fondamentale per il comportamento dell'idrossiapatite, in particolare se maggiore di 1,5 il minerale si mostra insolubile, mentre diventa solubile per valori inferiori a 1,5. In questo senso, il campione 1 mostra un rapporto di 1,67 mentre il campione 2 un rapporto di 1,80.

A parità di contenuto di calcio e fosforo, un aumento del rapporto mostra anche un aumento della quantità di ioni ferro presenti nell'idrossiapatite.

La sintesi è realizzata in differenti passaggi. Per prima cosa, sono preparate due soluzioni in 10 ml di etanolo assoluto rispettivamente di nitrato di calcio tetraidrato e di pentossido di fosforo. Dopo circa 10 minuti di agitazione magnetica delle soluzioni, sono inseriti i due precursori degli ioni ferro, uno per soluzione. In seguito le due soluzioni così preparate sono collocate sotto agitazione magnetica per altri 10 minuti. Non appena le polveri sono completamente dissolte, le due soluzioni sono collocate in bagno d'olio a 90°C, fino alla formazione di un gel che richiede circa 1 ora.

Dopodiché le due soluzioni sono calcinate in forno ad 80°C per 24 ore.

Infine, entrambe le polveri sono trattate termicamente a 3 temperature differenti : 600°C, 700°C e 800°C.

Dopo la preparazione dei 6 campioni, essi vengono sottoposti a differenti analisi. La prima riportata è l'analisi ai raggi X. Tramite questa analisi è possibile ottenere informazioni circa la composizione delle polveri (comparando a spettri noti rinvenibili in letteratura). Inoltre, è anche possibile calcolare il diametro dei cristalliti presenti all'interno del materiale, così come i parametri reticolari, la percentuale di cristallinità ed il rapporto tra l'idrossiapatite e gli altri fosfati presenti per ciò che riguarda la composizione delle polveri.

Tramite l'analisi dei picchi degli spettri dei campioni è possibile ottenere informazioni riguardo la composizione delle polveri analizzate. Per prima cosa è analizzato il campione 1 trattato a 600°C,

facendo riferimento alla fig. 3.2. Come è possibile notare, benchè il materiale presenti i principali picchi dell'idrossiapatite, presenta anche altri picchi significativi. Questa è indicazione della composizione delle polveri che differisce a livello strutturale dall'idrossiapatite standard.

In particolare, alcuni picchi sono etichettati come espressioni della presenza di fosfato di dicalcio anidro nelle polveri e di  $\beta$ -TCP, una tipologia di fosfato che può formarsi sotto determinate condizioni nella sintesi di idrossiapatite.

La presenza di queste apatiti secondarie può essere invece dovuto sia alla tipologia di trattamento termico cui è sottoposto il materiale, che può infatti risultare nella produzione di fosfati di calcio come prodotti secondari, sia al valore del rapporto Ca/P maggiore di 1,67, come avviene nel caso delle polveri studiate.

Nel considerare il campione 2 – 600°C, riferendosi alla fig. 3.4, è possibile notare la similitudine netta con uno spettro di una normale idrossiapatite con rapporto Ca/P uguale a 1,67.

Da questa prima analisi, si può concludere che l'introduzione di maggior ferro nella struttura porti alla formazione di più composti secondari. Trattasi comunque di considerazione che possono verificarsi approfondendo ulteriormente le analisi delle polveri in questione.

Interessante può essere anche paragonare tra loro i diversi spettri relativi a materiali di uguale composizione ma trattati a temperature differenti. In particolare risulta interessante comparare tra loro gli spettri relativi al campione 2, per il quale probabilmente la temperatura del trattamento determina maggiormente le caratteristiche delle polveri.

Infatti, come si può vedere dalla fig. 3.6, due sono le principali differenze evidenziabili al crescere della temperatura. In primo luogo, il picco relativo al piano cristallografico (202) diventa sempre più significativo al crescere della temperatura, mostrando come questo piano si sviluppi di più a temperature maggiori. Infine, all'aumentare della temperatura di trattamento un picco a  $28,5^\circ$  si va via via più evidente. Basandoci sulla letteratura questo potrebbe essere un segno della presenza di ematite nelle polveri, essendo quello un tipico picco dell'ematite. Questo inoltre spiegherebbe il graduale cambio di colorazione delle polveri che si fanno più rosse al crescere della temperatura: il rosso che è infatti segno della presenza di ossidi di ferro.

Svolgere i trattamenti termici in atmosfera di azoto, potrebbe essere una buona soluzione per limitare la presenza di ematite all'interno dell'idrossiapatite sintetizzata.

Come detto anteriormente, è possibile avere indicazione delle percentuali di cristallinità del materiale analizzando gli spettri di diffrazione e utilizzando l'equazione 3.2.

Come si può notare dalla tabella 3.1 dove tutti i dati sono raccolti, in generale il campione 1 caratterizzato da un maggior tenore di ferro al suo interno, mostra una percentuale generalmente più alta rispetto al campione 2. Inoltre il campione 2 mostra un andamento della cristallinità che risulta diminuire all'aumentare della temperatura selezionata per il trattamento.

Per ciò che riguarda il diametro dei cristalliti, come si vede dalla fig. 3.8, mentre non sembra esserci correlazione tra le dimensioni di cristallito e la temperatura del trattamento, si può intuire che al crescere del tenore di ferro incorporato nel reticolo, il diametro aumenta. Infatti, comparando il campione 1 e 2 per qualsiasi temperatura di trattamento, il campione 1 mostra sempre un diametro maggiore.

È possibile inoltre ottenere informazioni sui parametri reticolari dei vari campioni e pertanto sulla loro struttura.

Come evidenziato in fig. 3.9 and fig. 3.10, è evidente come il campione 1 mostri sempre valori dei parametri superiori a quelli del campione 2 per qualsiasi temperatura del trattamento termico. Questo consente di concludere che un aumento del tenore di ferro può determinare un aumento dei parametri reticolari. In particolare, in letteratura è possibile incontrare vari esempi con risultati in contrasto tra loro. Infatti *Trinkunaite-Felsen et al.*[63] mostrano come all'aumentare del tenore di ferro si abbia una coincidente diminuzione dei parametri reticolari, essendo questo in contrasto con il risultato espresso pocanzi.

In particolare è interessante analizzare il variare dei parametri reticolari, perchè offrono indicazioni sulla struttura del reticolo e quindi sulle proprietà finali del materiali sintetizzato. È interessante in questo senso cosa esprimono *Gomes et al.* [49] i quali evidenziano una espansione dell'asse *c* con conseguente diminuzione del parametro *a*. La variazione dei parametri si ottiene a temperature comprese tra 1000 e 1100°C e il suo tenore dipende dalla concentrazione di ioni ferro.

Infine è possibile ottenere indicazione sulla composizione di fase per ciò che riguarda il rapporto tra la quantità di idrossiapatite presente e gli altri fosfati. Utilizzando l'equazione 3.3 è pertanto possibile ottenere l'andamento della percentuale di rapporto tra i fosfati presenti, per quanto riguarda il campione 1 trattato alle 3 differenti temperature. Si può notare come, seppur non in grandi proporzioni, ci sia un aumento della percentuale di fase al crescere della temperatura.

Attraverso l'analisi FTIR è possibile avere ulteriori informazioni circa la composizione e la struttura chimica delle polveri analizzate. Infatti l'energia dei raggi infrarossi inviati sul materiale determinano movimenti dei gruppi funzionali all'interno, della tipologia rappresenta in fig. 2.4. Come al solito, per primo viene analizzato il campione 1-600°C, il cui spettro è presentato etichettato nella fig. 3.12.

Come si può notare, tutti i picchi tipici dell'idrossiapatite sono presenti. Infatti i due picchi a 1090  $\text{cm}^{-1}$  e 1040  $\text{cm}^{-1}$  così come la spalla a 960  $\text{cm}^{-1}$  sono rispettivamente lo stretching asimmetrico e simmetrico degli ioni fosfato  $\text{PO}_4^{3-}$ . A 3600  $\text{cm}^{-1}$  un piccolo picco fa riferimento alla vibrazione di OH. Non è però un picco molto intenso, questo a causa della presenza di  $\text{CO}_3^{2-}$  che può entrare nel reticolo sostituendo ioni idrossido e ioni fosfato. La sua presenza è evidenziata anche dalla presenza dei picchi a 1400  $\text{cm}^{-1}$ , 1500  $\text{cm}^{-1}$  e 873  $\text{cm}^{-1}$ . Quest'ultimo in letteratura viene anche assegnato alla presenza di  $\beta$ -TCP la cui esistenza sembra confermare le informazioni già rinvenute nell'analisi dello spettro dei raggi X del campione.

Infine, altri picchi degni di nota sono quelli a 1200  $\text{cm}^{-1}$ , 1160  $\text{cm}^{-1}$  e 730  $\text{cm}^{-1}$  che sono tipici della presenza di un altro fosfato, il fosfato di calcio anidro (DCPA,  $\text{Ca}_2\text{HPO}_4$ ).

Nell'analizzare lo spettro ottenuto per il campione 2-600°C, presentato in fig. 3.13 è possibile rinvenire gli stessi picchi principali dell'idrossiapatite ritrovabili nel caso del campione 1, così come i picchi relativi alla presenza di ioni carbonato e idrossido. Allo stesso modo sono individuabili i picchi relativi alla DCPA. Non sono invece presenti i picchi relativi al fosfato tricalcico, che non è pertanto presente, come confermato anche dall'analisi dello spettro dei raggi X.

Nell'analizzare gli spettri dei 3 campioni 1 trattati termicamente a 3 differenti temperature è possibile notare come il picco a 1000  $\text{cm}^{-1}$  sia via via più intenso al crescere della temperatura di trattamento, evidenziando un aumento di cristallinità delle polveri, come mostrato già nell'analisi XRD.

Come detto, l'obiettivo del progetto è quello di riuscire a sintetizzare idrossiapatite dopata con ferro in grado di esibire comportamento super-paramagnetico. Per questa ragione, fondamentale è l'analisi di magnetometria del campione vibrante (VSM). In questa prova è possibile ottenere le curve di magnetizzazione in funzione del campo magnetico applicato a determinate temperature pre-selezionate. Valutando il valore del campo coercitivo è possibile infine stabilire se si ha a che fare con polveri ferromagnetiche ( $H_c > 0$ ) oppure con polveri super-paramagnetiche ( $H_c = 0$ ).

È inoltre possibile sottoporre le prove a test di FC e ZFC, in cui FC sarebbe a campo applicato e ZFC a campo non applicato. Queste prove consistono in variare la temperatura e valutando il momento magnetico del campione in esame. È possibile con questa tipologia di prova valutare eventuali transizioni magnetiche e la temperatura di Block. Come è evidente dalle fig. 3.17 e 3.19, i campioni 1 trattati rispettivamente a 600°C e 700°C sono in grado di esibire un comportamento che è super-paramagnetico dove il campione 2-700°C dimostra un comportamento più marcatamente super-paramagnetico.

Lo stesso tipo di risultato è possibile conseguire analizzando i grafici relativi ai campioni 2, sinterizzati a 600°C e 800°C. Come si vede bene dalle figure 3.17 e 3.22.

Infine è interessante analizzare l'analisi FC e ZFC del campione 2-800°C, rappresentato in fig.3.23. Infatti, in questa curva è possibile evidenziare una transizione magnetica a 50K (da approfondire ulteriormente in investigazioni future) e la sovrapposizione delle curve a 100K. Quest'ultima caratteristica del grafico identifica la temperatura di Block a 100K, punto di inizio della sovrapposizione.

Fondamentale ai fini della applicazione finale del materiale e l'analisi dell'ipertermia magnetica delle polveri. Per questo risultato, 3 repliche per ciascun campione sono preparate ed inserite in etanolo, per essere poi sottoposte ad un campo magnetico alternato con l'obiettivo di registrare un eventuale aumento di temperatura dovuto al comportamento magnetico delle polveri.

Per condurre la prova, si sceglie un tempo di analisi di 10 minuti, intervallo nel quale un campo magnetico alternato viene applicato sul campione inserito nel macchinario. Il campione è prodotto inserendo polveri di un singolo campione in etanolo assoluto con una concentrazione di 5% m/V.

Il risultato desiderato sarebbe quello di incrementare la temperatura fino ad un valore compreso tra 41 e 43°C, partendo da una temperatura di base che è quella corporea : 38°C. Il tutto in un arco di tempo di 10 minuti. Sfortunatamente, nessuno dei materiali sintetizzati è in grado di mostrare sufficiente aumento di temperatura nel tempo di 10 minuti e con la concentrazione utilizzata. Però ai fini della ricerca alcune delle polveri si rivelano comunque promettenti, meritevoli essere approfondite in futuri lavori. Infatti aumentando la concentrazione di polveri considerata per la prova o prolungando la durata di applicazione del campo esterno, le polveri potrebbero rivelarsi idonee ad esprimere il desiderato aumento di temperatura. I risultati sono raccolti nel grafico in fig. 3.24.

In particolare, nel caso del campione 1, tutte e 3 le polveri trattate alle 3 differenti temperature mostrano un incremento di temperatura quando sottoposte ad un campo magnetico al crescere della temperatura del trattamento. Tra questi, il campione trattato a 700°C mostra il maggiore aumento, mostrando al contempo la minore cristallinità, il minore diametro di cristallito e i parametri reticolari minori quando paragonato agli altri campioni 1.

Curioso è il caso del campione, per cui solo quello trattato a 800°C mostra un incremento in temperatura, che è anche il maggiore in assoluto. Essendo anche il campione in cui l'analisi XRD ha evidenziato la presenza di ematite, diventa fondamentale analizzare la sua biocompatibilità per eventuali sviluppi futuri.

Questo si dimostra pertanto un materiale promettente per quanto riguarda i trattamenti di ipertermia magnetica, come si capisce anche da molti esempi ritrovabili in letteratura. Per esempio, *Hou et al.* [46] mostrano risultati promettenti dopo aver trattato per 15 giorni il tumore di un topo di laboratorio, con ipertermia magnetica.

Fondamentali sono i risultati ottenuti dai test di bioattività per l'applicabilità del materiale nell'organismo umano senza determinare tossicità o effetti collaterali.

Per svolgere l'analisi di bioattività, per prima cosa viene preparato un fluido capace di simulare l'ambiente dell'organismo umano. Per realizzarlo, i precursori elencati in tabella 2.4 sono miscelati nel giusto ordine e quantità secondo ricette che sono comodamente trovabili in letteratura.

In seguito le polveri sono formate nelle sembianze di dischetti sottili che sono poi inseriti all'interno del SBF (dall'inglese "simulated body fluid", fluido del corpo simulato), per 3 tempi differenti : 1 giorno, 3 giorni e 7 giorni.

Dopodichè i campioni sono analizzati al SEM di modo da valutare l'andamento delle reazioni chimiche sulla superficie. In questo è possibile valutare in modo qualitativo la biocompatibilità di ciascun campione.

Nell'analizzare il campione 1 – 600°C è pertanto possibile osservare l'avanzare della reazione di formazione di cristalli di idrossiapatite sulle superficie dovuti alla bioattività delle polveri nelle fig. 3.26, fig. 3.27 e fig. 3.28.

In particolare su alcune delle particelle la reazione bioattiva che porta alla formazione dello strato di idrossiapatite superficiale sembra essere maggiormente avanza. Questo può essere causato da una riduzione della taglia delle particelle considerate (aumento della reattività al crescere dell'area specifica) o da una variazione di composizione a livello locale, che può rendere il materiale localmente più o meno suscettibile alla reazione.

È interessante notare inoltre come col passare del tempo la reazioni interessi sempre maggiori porzioni di materiale, nonostante sia comunque sufficientemente rapida da sviluppare un layer di idrossiapatite superficiale già dopo 24 ore.

La prima impressione quando si paragona il campione 1- 700°C al campione 1-600 C è di una maggiore coalescenza delle polveri, dovuto al trattamento termico di temperatura maggiore. Per ciò che riguarda il comportamento in SBF, il campione 1-700°C, pur mostrando la stessa evoluzione temporale del campione 1-600°C, mostra una reazione che interessa una porzione superiore di superficie dopo 7 giorni di immersione.

Pertanto il campione 2 a 700°C mostra un comportamento più bioattivo sul lungo termine quando comparato al campione 1-600°C.

Nello svolgere lo stesso tipo di analisi per il campione 2-600°C è possibile valutare nelle fig. 3.35, fig. 3.36 e fig. 3.37 l'andamento della reazione per tempi di esposizione sempre più elevati. Come si può notare, pur mostrando un decorso simile al campione 1, mostra in generale una reazione di bioattività che procede più a rilento ed interessando una minore porzione di superficie. In questo senso il campione 2 sembra mostrare inferiore bioattività, tendenza inoltre confermata analizzando gli altri campioni 2 a 700°C e 800°C.

Questo può essere dovuto dalla minore presenza di ferro dopante. Conclusione confermata dalla letteratura, infatti *Ereibe et al.* [71] hanno raggiunto la stessa conclusione.

È interessante sottolineare come il campione 2-700°C mostri la minore bioattività, questo forse a causa della maggiore presenza di fosfato tricalcico quando paragonato agli altri campioni di uguale composizione.

Risulta interessante valutare la bioattività del campione 2-800°C essendo il più promettente per quanto riguarda l'ipertermia magnetica. Dopo 7 giorni di immersioni, apatite è deposta lungo tutta la superficie, mostrando una bioattività superiore quando comparato ai campioni 2 trattati a 600°C e 700°C. Comunque la bioattività è inferiore quando comparato con tutti e 3 i campioni 1.

Interessante notare come in entrambi i campioni relativi alle polveri di composizione 2 e trattati ad 800°C si evidenzia la presenza di strutture allungate di non chiara composizione. Si ipotizza che l'elevata temperatura di trattamento abbia fornito energia sufficiente a crescere una struttura ordinata oppure sono determinati dalla presenza dell'ematite evidenziata in questa polvere tramite l'analisi XRD.

Infine i campioni sono sottoposti ad analisi di citotossicità ponendo le polveri in soluzione in contatto con cellule Vero. Le polveri dei materiali così come le cellule sono inserite all'interno di pozzetti riempiti con un mezzo fluido, in cui viene inserita resazurina. Essa ha la caratteristica di cambiare colore quando in contatto con cellule vive, essendo esse in grado di processarla e trasformarla in resofurina. Queste due sostanze sono contraddistinte da due assorbanze distinte e valutandole entrambe è possibile determinare la percentuale di viabilità di ciascun pozzetto. In questo modo è poi possibile realizzare il grafico in fig. 3.44 in cui si evidenziano in un grafico a barre la viabilità delle soluzioni. In particolare, maggiore è il valore percentuale registrato, meno tossico è il materiale. Inoltre l'esperimento viene svolto con concentrazioni differenti.

In particolare, si può notare come nel caso del campione 1, al crescere della temperatura la tossicità delle polveri aumenta, mostrando come al crescere della temperatura più facilmente si formino composti potenzialmente tossici. In generale però i campioni 1 presentano meno tossicità dei campioni 2, mostrando maggiore biocompatibilità cosa già evinta dalle analisi di bioattività dei campioni.

Infine, interessante il caso del campione 2-700°C, essendo quello che mostra maggiore tossicità con valori alla concentrazione nominale  $C_0$  di circa il 60% di cellule vive. Percentuale molto bassa, che conferma la scarsa bioattività del campione 2-700°C già evidenziata nell'analisi della sua bioattività.

Per concludere, è pertanto utile sottolineare come variazioni anche piccole dei parametri di sintesi abbiano grande influenza sulla struttura finale del materiale, facendo variare in modo netto molti valori quali ad esempio i parametri reticolari. Da questa possibile grande varietà di valori sono stati sintetizzati 6 diversi campioni in cui ognuno di essi mostra caratteristiche peculiari. Curioso quindi come caratteristiche a volte anche sorprendente differenti possano essere originate da piccole variazioni nel processo di sintesi. In questo senso è emblematico cosa accade con i campioni di composizione 2, per cui si registra la maggiore attività quando esposto a campo magnetico con il campione trattato a 800°C, ma anche la minore con gli altri due.

Siccome i parametri affettano molto il risultato finale, diventa interessante per i prossimi studi valutare come i cambiamenti di alcune condizioni possano affettare i risultati finali.

Per questo motivo può essere interessante performare la sintesi in atmosfera controllata andando così a ridurre il rischio di formazione di ematite residua a causa della reazione tra ferro ed ossigeno atmosferico.

Siccome la struttura reticolare determina in modo pesante il dopaggio degli ioni ferro, saper predire come al variare del tenore di dopante inserito variano i parametri reticolari può essere fondamentale per future applicazioni. Per questo motivo può essere utile eseguire analisi con *Analisi Rietveld* e spettrometria Mossbauer per avere indicazioni sulla struttura cristallina al variare della quantità di ferro inserito e al variare della temperatura del trattamento termico.

In questo progetto si è utilizzata una tecnica di sintesi sol-gel la quale è contraddistinta da un tempo di invecchiamento che è possibile performare sulle polveri. Può essere interessante per sviluppi futuri capire come questo possa influenzare le proprietà finale del materiale sintetizzato.

Infine, è interessante notare come con questo lavoro si è provato un aumento di bioattività al crescere della quantità di ferro inserita come dopante. Questo risulta in una minore tossicità delle polveri al crescere della quantità di ferro introdotto nella struttura.

Questo risultato, corroborato da simili risultati riscontrabili in letteratura, può essere fondamentale anche per l'utilizzo di questo materiale in altri ambiti quali ad esempio il rilascio controllato di farmaci in loco, attività per la quale una alta bioattività è fondamentale.

Nell'intervallo di 10 minuti e con la concentrazione selezionata non è stato determinare nelle polveri un riscaldamento sufficiente ad essere utilizzate per applicazioni di ipertermia, il comportamento super-paramagnetico evidenziato con il test VSM rende queste polveri un ottimo candidato per ulteriori analisi e sviluppi. Infatti, aumentare il tempo di prova o la concentrazione, potrebbe già essere sufficiente ad ottenere i risultati sperati.

Risulta quindi necessario in futuro approfondire e potenziare il metodo di sintesi, indagando più a fondo come i parametri incidono sulle proprietà finali. In questo modo da controllare maggiormente il risultato del processo, affinando al contempo il processo produttivo utilizzato.

Per concludere, questo materiale dunque si presenta come uno dei più interessanti per futuri sviluppi nell'ambito dei materiali super-paramagnetici per applicazioni biocompatibili, avendo mostrato i requisiti magnetici e di biocompatibilità richiesti.

## Abstract

Cancer is regarded as the disease that killed more people in the last decade, with an increasing number of victims from year to year. Beneath all possible forms of it, in this work the focus is on bone cancer, not so common but still accounting a lot of victims.

Several investigations are nowadays performed to increase the chances of detection and prevention, this being always the best way to deal with cancer cells. However, it is not always easy to detect and sometimes medical intervention to cure the pathology is needed. For this reason, a big branch of research is focus on the discovery of new medical solution able to deal with different kind of cancer.

For what concerns bone cancer, one of the main investigated cure deals with hyperthermia treatment.

This treatment relies on cancer cells weaker resistance to high temperature and x-rays when compared to viable one. Indeed, with a permanence of a temperature higher than 42°C enzymatic process that keep cells alive stop working, determining the selective death of cells.

Therefore, oxide nanoparticles are used to treat some types of cancer. These particles are injected into the blood and then guide using the magnetic field to the application site where using an alternate magnetic field they are heated up until the temperature needed to kill tumoral cells. These particles are able to show super-paramagnetic behaviour which is essential to fulfil the proper increase of temperature in a required range of time. In fact, high temperature can determine the death also of healthy cell on the long term.

Another crucial aspect to be considered is that super-paramagnetic particles are able to switch off their magnetization instantly when the external field is removed, avoiding the risk of particles agglomeration which could heavily damage the organism. It is therefore important to use a biocompatible material, this being a crucial aspect in application when the material is in contact with human body.

The perfect candidate should show biocompatibility and super-paramagnetic behaviour. For this purpose, iron doped hydroxyapatite is synthesized, in different composition and varying the sintering temperature studying how these two parameters influence final properties of the synthesized material.

The process chosen for the production is the sol-gel process, this being an easy-controllable, not complicate and more economic process when compared to precipitation of microwave assisted.

In this sense, particles are investigated through several tests, carried on with the object of testing the actual possibility of material application in hyperthermia treatment as well as the composition and structure of the final product.

None of the synthesized powders is able to show the required super-paramagnetic behaviour, not guaranteeing the desired increase in temperature till 42°C, in the timeframe of 10 minutes and with the concentration used. However, increasing the concentration or the timeframe could enough to attain the desire result. This because particles prove themselves in the VSM to show the super-paramagnetic required for hyperthermia treatment application, along with biocompatibility.

Moreover the research proved to be useful also for other important discoveries. Firstly, varying the composition of powder by changing the quantity of reagents used in the beginning of the sol-process it is possible to influence biocompatibility of material. In fact, increasing the amount of iron incorporated inside hydroxyapatite it is possible to increment the biocompatibility of samples produced.

This being very interesting and important also in case of other iron doped hydroxyapatite where biocompatibility is a high requirement, in drug delivery for instance.

The main goal of this project has been reached: iron doped – hydroxyapatite with super-paramagnetic behaviour has been successfully synthesized.

It is therefore important improve and analyse deeper the process, in order to control better properties of the synthesized powders. For this reason, it can be useful for further works to investigate how the sintering process could affect the final properties and the material.

In the same way, it is interesting to analyse how varying ageing time of hydroxyapatite in the sintering process could affect the final results, this not being investigated in this project in particular.

## Introduction

Cancer is one of the major causes of death in the 21<sup>st</sup> century, killing 8.9 million of people just in 2016. Beside of being difficult to be detected, it can affect different part of the bodies in various ways: it is for this reason that doesn't exist a specific treatment able to stop the proliferation of cancer cells. Each situation needs its own therapy and the success of it largely depends on how the body of the patient responds to the cycle of treatments applied.

Aside from all the researches performed in medical field on detection, prevention and cure of different forms of cancer, several studies are carried on in engineering field as well, to improve the quality of the technology available for its treatment.

Specifically, the main focus of this thesis is on bone cancer, less common than others but still accounting a large number of victims, especially younger ones.

Bone cancer comprises primary malignant tumor, which develop directly on the bone site, or secondary malignant tumor due to metastasis from other primary cancer such as breast, prostate and lung[1].

An early detection of the cancer can heavily simplify the cure process and improve the life quality of the patient. In particular in bone cancer pain, that is one of the most common symptom in oncological patients, appears soon in the disease evolution and easily evolved into hyperalgesia[1].

Once detected, the cure process can start and can follow different paths according to the health situation involved.

Cure usually relies on the aspect that cancer cells are more sensitive to X-rays or temperature increase, this being the principle at the basic of magnetic hyperthermia treatment.

In fact, above the temperature of 42°C the enzymatic processes that keep cancer cells alive are destroyed, allowing this way their selective killing[2].

For some kind of cancer, iron oxide used nanoparticles are carried on site and by applying an external alternate magnetic field they warm up till the required temperature starting killing tumoral cells. Nanoparticles in general are largely used due to their very small size they are able to arrive and interact directly with sick cells exploiting their thermal effect on the spot and to the possibility of being carried inside the human body, always exposing a large surface area that obviously facilitates the process.

Super-paramagnetic nanoparticles are particularly suited for this kind of application, being able to quickly interact with the applied magnetic field, with magnetization dropping to zero after the applied field is removed, which is good to avoid some health problem in the patient, due to aggregation of the nanoparticles after the treatment[2].

At the same time, a biocompatible type of material is required for this kind of application.

For all these reasons Hydroxyapatite can be a possible candidate for healing bone cancer, if properly doped in order to show paramagnetic behaviour.

That is the main goal of this thesis project: synthesize iron-doped hydroxyapatite nanoparticles able to show a super-paramagnetic behaviour.

For this objective, it is used a sol-gel process that has the advantage of being simple and with parameters that can be easily controlled.

Two different hydroxyapatites are produced, with different contents of Iron, to see how different quantities of iron inserted into the lattice affect the final product.

In parallel, also the influence of the thermal treatment is investigated: 3 different sintering temperature are used (600,700,800°C) for both types of iron-doped hydroxyapatite.

Before discussing the results of the project, a theoretical introduction is presented and to achieve this all the main topics are treated singularly, with a focus on what is related to the thesis main topic.

## 1 Theoretical background

As the target for the nanoparticles produce within this project is to use them in magnetic hyperthermia treatment on bones, the first paragraph of this summary is about the bone and its structure.

### 1.1 Bone

The bones of the skeleton provide mechanical support for joints tendons and ligaments, protect vital organs and act as a storage for calcium and phosphate [4].

Bone passes through several passages of remodelling and reconstruction within its life due to reparation and reinforcement.

In human body can be found two different structural types of bones: cortical bones and trabecular or cancellous (known also as spongy) bones.

Cortical bones (fig.1.1) are stiffer and much heavier than trabecular one: they contributed to more than 80% bones' total weight. They are composed of Haversian systems, which consists of lamellar bones that surround a central canal containing blood vessels [4]. Typical examples of these kind of bones are usually long bones such as femur.

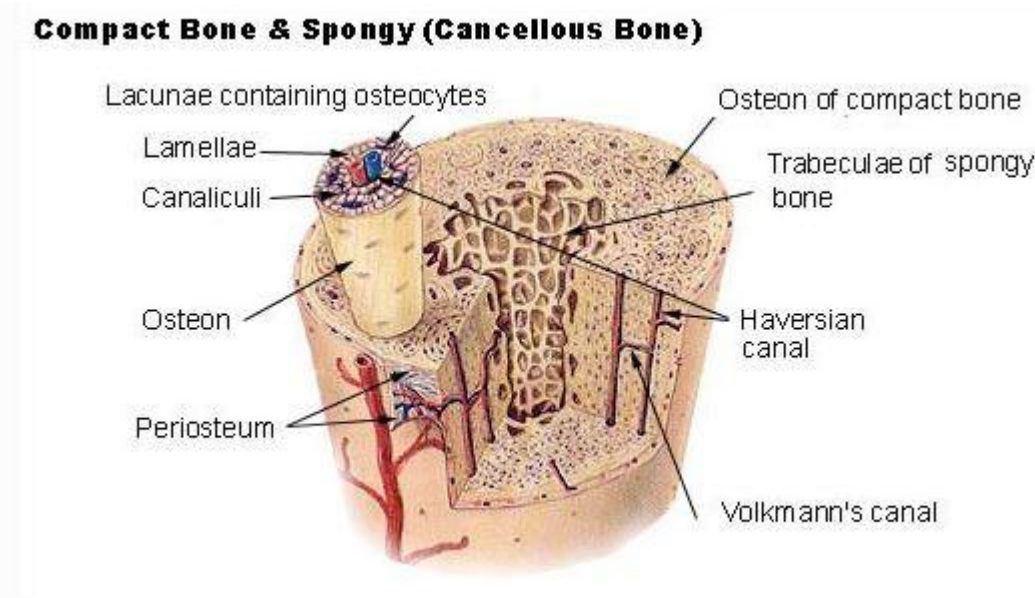


Fig. 1.1 Section of cortical bone (exterior) and focus on haversian canal [5].

Spongy bones (fig. 1.2) show a lower density but in the same time a larger surface, due to high porous structure. Made of interconnected bones trabeculae, the empty space inside is filled with bone marrow responsible for new blood cells production [4].

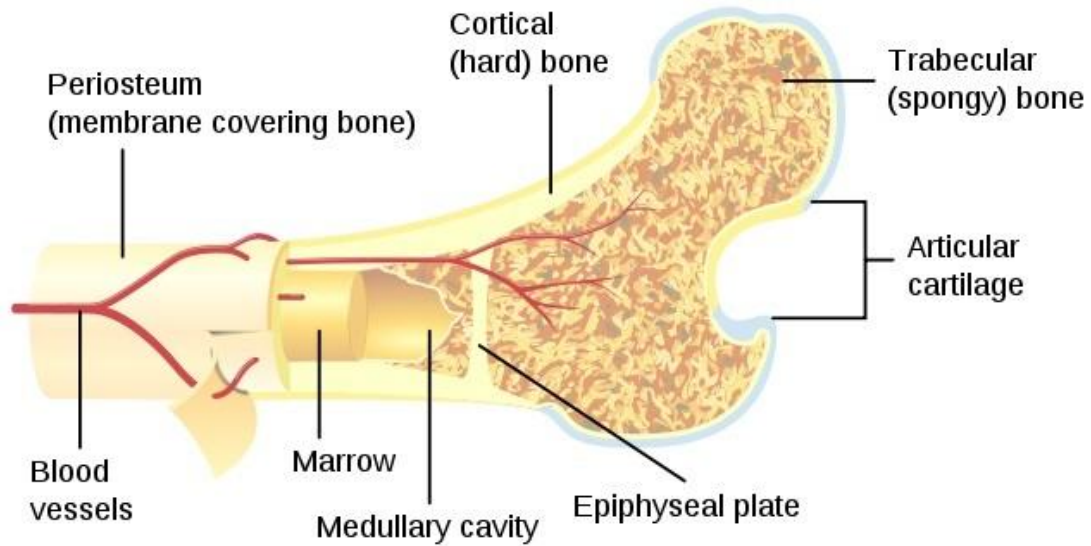


Fig. 1.2 Spongy bone section[6].

The light weight of spongy bones balances out the heavier cortical bones and facilitates muscles in movements. Cancellous bones form predominantly along lines of stress giving the bone strength and flexibility. Meanwhile they act as shock absorber for the body when we walk, run or jump [6]. In the fig. 1.3 we can see a comparison between spongy bones and cortical bone.

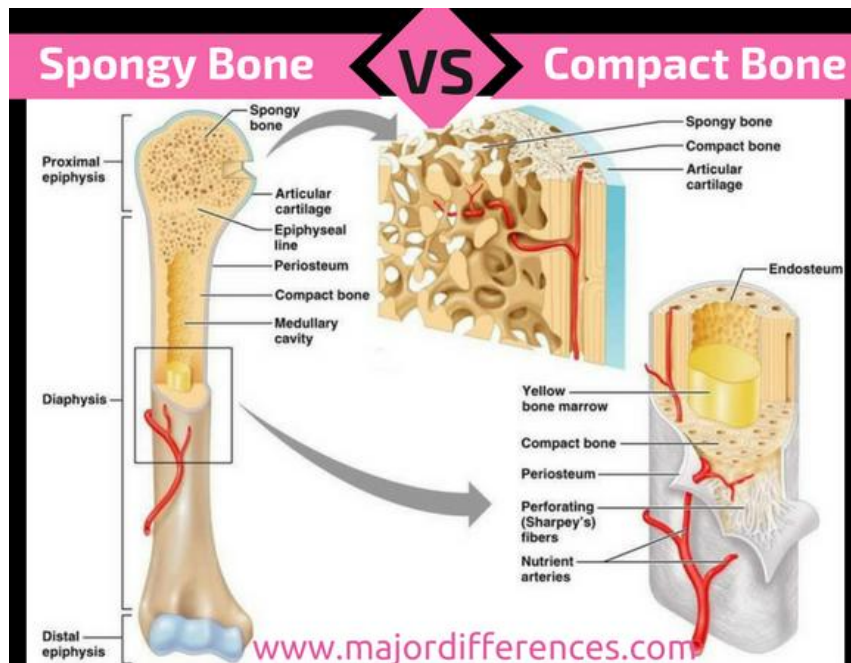


Fig. 1.3 Structure compared of both spongy and compact bone [7].

As can be seen from the fig.3, both type concur in the structure of bones, by being the compact at the exterior and the spongy in the interior.

As for composition, the bone can be considered a composite material by having an organic part, principally a fibrillar protein shaped into a triple helix: type I collagen.

The organic component of bones forms a matrix upon which mineralization occurs. Mineralization provides rigid component to bones that balanced the tensile strength and elasticity that comes from bone collagen. Bone minerals are mainly composed by calcium and phosphate laid down in the form of hydroxyapatite ( $\text{Ca}_{10}(\text{PO}_4)_6(\text{OH}_2)$ )[4].

Defects in mineralization can led to several problems connected to insufficient amount of calcium and phosphate storage and consequently to health problems.

## 1.2 Hydroxyapatite

Being an orthophosphate and a type of apatite, Hydroxyapatite (HAp) is a crystalline mineral with the chemical composition  $\text{Ca}_{10}(\text{PO}_4)_6(\text{OH}_2)$  and is widely used as bone substituent and for other heal intervention on bones because of its similar composition to the inorganic component of human bones and bioactivity.

The Ca/P ratio characterizes each type of hydroxyapatite determining the solubility of the mineral considered. The critical value of ratio is 1.5: below this value is soluble, on the other hand above the value it gets more and more insoluble as the ratio increases [7].

Strength varies with Ca/P, in particular it increases till the ratio of 1.67 and suddenly start decreasing for higher value. Usually the composition is chosen to show a ratio of 1.67, so not totally soluble and with the highest strength possible[7][8].

Characterised by a hexagonal lattice cell, Hydroxyapatite shows cell parameters  $a=b=9,41 \text{ \AA}$  and  $c=6,88 \text{ \AA}$ .

As we can see in fig. 1.4, the crystalline structure is quite complex, with phosphate ions ( $\text{PO}_4^{3-}$ ) coordinating 4 hydroxyl ions ( $\text{OH}^-$ ) into the shape of a tetrahedron[9][10].

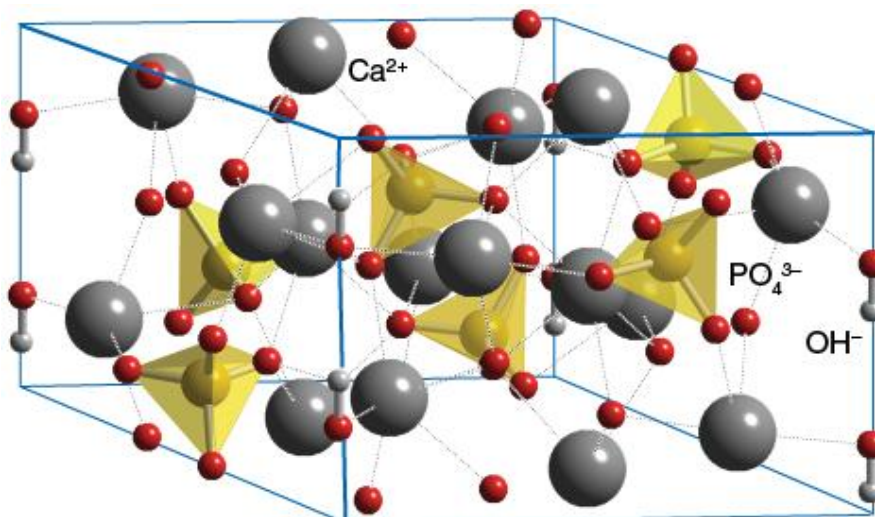


Fig. 1.4 Hydroxyapatite cell structure[11].

It is possible to have ionic substitution inside Hydroxyapatite, altering several properties of the biomaterial.

In order to understand which kind of substitution is possible, it is necessary to consider the general formula of apatite:  $\text{Me}_{10}(\text{XO}_4)_6\text{Y}_2$ . Considering the formula, in the table 1.1, all the possible ionic substitution are presented.

**Table. 1.1** Possible ions substitution in Hydroxyapatite [12].

$\text{Me}^{2+}$	$\text{Ca}^{2+}$	$\text{Sr}^{2+}$	$\text{Ba}^{2+}$	$\text{Cd}^{2+}$	$\text{Pb}^{2+}$
$\text{XO}_4^{3-}$	$\text{PO}_4^{3-}$	$\text{AsO}_4^{3-}$	$\text{VO}_4^{3-}$		
$\text{Y}^-$	$\text{OH}^-$	$\text{F}^-$	$\text{Cl}^-$	$\text{B}^-$	

Every ions can affect cell parameters of the lattice and properties of the final materials, such as Sr that increases a-axis and c-axis dimension, while increasing crystallinity and affecting osteoclast activity[12].

Synthesized in nanoparticles, hydroxyapatite offers a wider surface area at the same volume, that allows a better interaction with tissues and bones. On addition to that by working on nanoscale it is possible to shape materials at the atomic scale, preparing an adequate porosity and chemical composition together with a functionalised surface, crucial for a best interaction with bone [13].

Polymer Functionalization can be implemented for drug-delivery application, exploiting nanometric porosity of hydroxyapatite, which offers a wide surface area that can be coated [14][15]. Drug-delivery application can also require magnetic properties of the particles in order to manage in a more accurate way the release of medicine directly in situ [2].

There are several synthesis processes that can be possibly used, being precipitation and sol-gel method the most appealing nowadays for the scientific community[16].

In the next chapter possible synthesis methods are presented, focusing on the sol-gel method that was selected for the project.

### **1.3 Synthesis method: panorama**

Hydroxyapatite can be used for several biomedical applications, ranging from prosthesis, which require a massive component able to simulate bone structure and properties, to nanoparticles to enhance hyperthermia process or other.

After synthesis, the material can be shaped in different way according to the final application.

To form it as a prosthesis, the mineral is shaped through different processes.

For records, it is presented one possible way to produce a scaffold of HAp, which can replicate the cortical-spongy structure of bones, passing through 2 different treatments.

The impregnation of a polymeric scaffold by slurry enabled the formation of a porous network that determine the inside core of the final product, replicating the spongy bone. After that, processing with ice templating is pursued to form the shell, very similar to compact bone[17].

Techniques such as co-precipitation, emulsion techniques, sol-gel method, mechanochemical method, electrochemical deposition and hydrothermal process, are used to produce hydroxyapatite nanoparticles. None of these methods can be used for industrial scale production, due to the involvement of expensive materials, complicated process, aggregation problems and numerous impurities (e.g. undesired crystal phases,  $\beta$ -TCP, tricalcium phosphate) [18].

Precipitation process is one of the main used due to the easiness of the process, that doesn't require high specific equipment, even though it is not easy to be controlled.

Level of pH needs to be checked all along the process and an expert operator is needed to mix different solutions with the correct timing, by adding them drop-wise with a high level of care. In fig. 1.5 is displayed a possible precipitation process, which lead to the formation of a white precipitated that needs to pass through a specific mill to break up the agglomeration and produce an ultrafine – nanometre sized HAp [18].

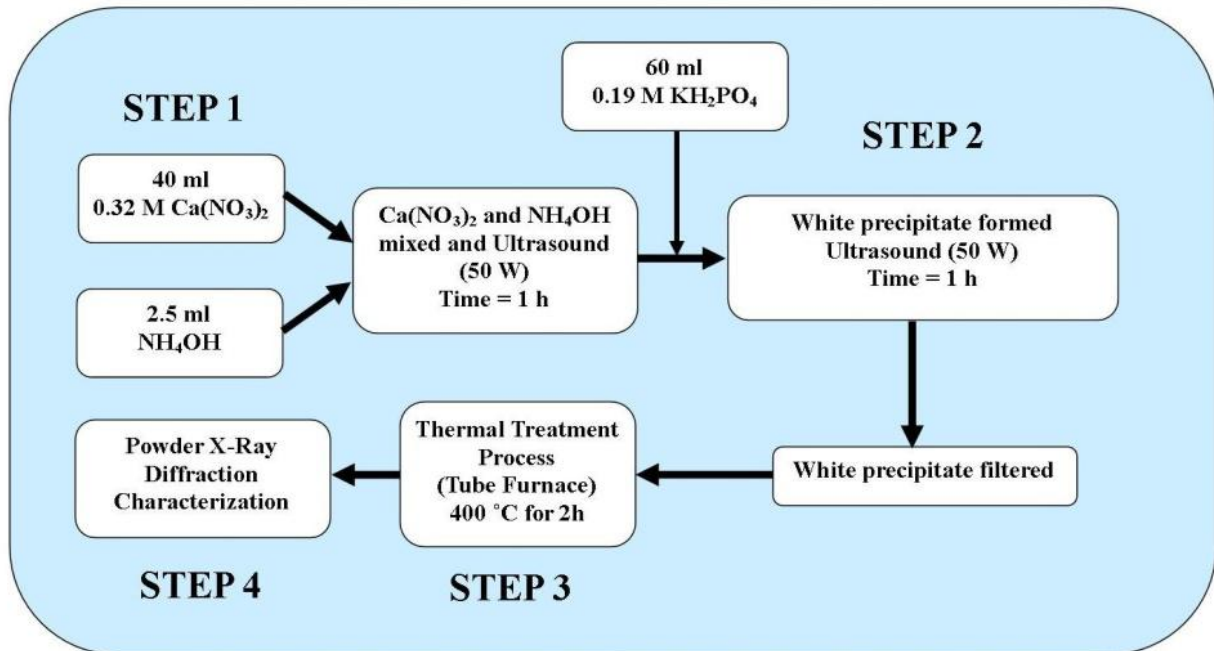


Fig. 1.5 Example of a precipitation process for the synthesis of HAp nanoparticles[18].

Precipitation defines a big group of different processes, by changing some parameters or adding new passages, the resulted HAp can be different in particle size, particle shape, stoichiometry and final properties. As a consequence, all the process should be followed and all the parameters accurately controlled to achieve reproducibility of the same HAp powders with the same properties [20].

The main synthesis process itself plays an important role in properties of the final bioceramic, determining specific surface area, particle shape and size, crystallinity and agglomeration degree (big or small, hard or soft). For this reason, the synthesis process gains importance [21].

Below a combination of precipitation and spray drying process is presented, with the aim of producing HAp nanopowders with very high specific area as soft spherical granules in very small size.

The two precursors (Ca(NO<sub>3</sub>)<sub>2</sub>·4H<sub>2</sub>O and (NH<sub>4</sub>)<sub>2</sub>HPO<sub>4</sub>) are dissolved separately in different quantities of ethanol. The 2 solutions obtained, are finally mixed together adding a solution of NH<sub>4</sub>(OH) drop-wise to adjust the pH at 9, taking care it remains at the same level along the all process.

The precipitate is finally filtered and washed and finally dispersed again in another solvent. This fine dispersed solution like milk is dried with a spray dryer which has a nozzle system to atomize the suspension [21]. The overall process, more specifically explained, is presented in fig. 1.6.

All the precipitation process has a common critical point: taking care of the agglomeration of the suspension is vital for the final result and has to be carefully checked.

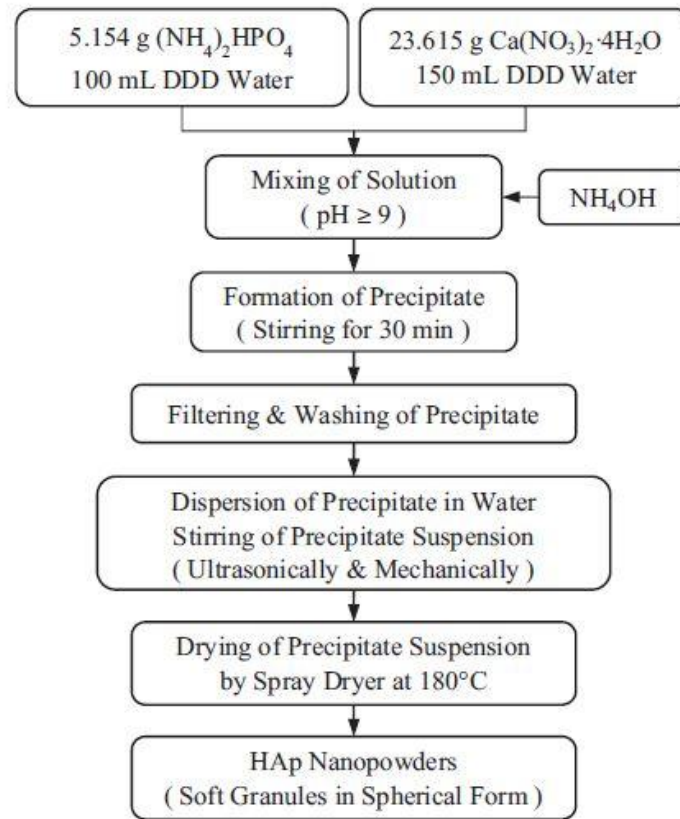


**Fig. 1.6** Precipitation – spray drying process for the formation of spherical size hydroxyapatite [21].

Another interesting process that deserved to be present here is the biomimetic process. It is simply a type of precipitation, completed using simulated body fluid (SBF) instead of a standard solvent. This process offers more bioactive, biocompatible and stable products when compared to conventional methods. It is also possible to improve HAp properties by controlling important parameters of the precursors such as particle shape and size, particle distribution and agglomeration [22]. In fig. 1.7 is displayed an example of this process.

As already stated, different process possibly leads to different shape and functionality of the final product. Pulsed electrochemical deposition is used to determine the formation of a HA coating which can be used to cover metallic alloy such as magnesium alloy for example. In this kind of process the parameters involved to be controlled to have the desired result are pulsed voltage, deposition time and electrolyte additive. They can all influenced the properties of final product, such as microstructure, composition, coating thickness, morphology and porosity.

These last 2 in particular are very important for the performance of the coating. In fact, being usually implemented to enhance the bon growth and osteoblast adhesion, a higher porosity ensures better results [23].

As can be easily understood from the panorama of processes presented, HAp is a highly versatile material that can be shaped in different forms with different properties characterised by a huge variety of different final application. Now the process chosen for the project presented through this thesis is introduced: the sol gel- method.

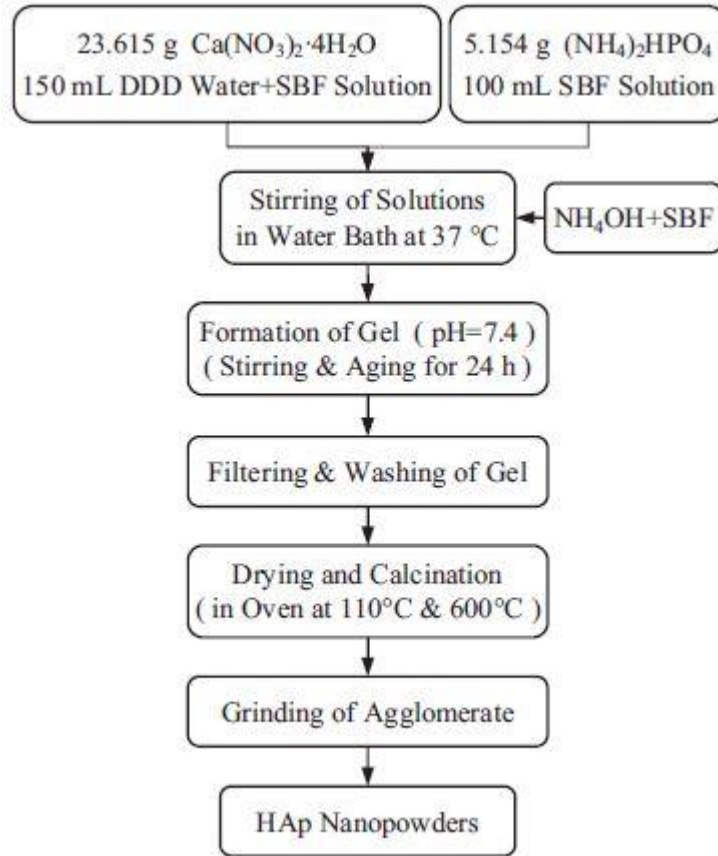


Fig. 1.7 Example of biomimetic process[21].

#### 1.4 Sol-gel process

Sol – gel process is a versatile technique that can be used for a large number of different materials. It can be described as a formation of an oxide network through polycondensation reaction of molecular precursors in a liquid medium. In particular, the “sol” is a stable dispersion of colloidal particles or polymers into a liquid. The gel is a continuous network which is originated by the interconnection between colloidal particles or polymers, that could be determined by van der Waals forces or hydrogen bonds. In some cases the network is formed through chemical reactions between particles.

The main idea behind the sol-gel process is to dissolve precursors of the final material into a solution and then, mixing at the atomic level, results into small particles, easily sinterable [25].

This kind of process can be easily implemented to produce HAp with the desired Ca/P ratio, adding other components to dope the final hydroxyapatite if wanted.

One critical aspect during the sol-gel process is, during the formation of the sol, to prevent particles from agglomerate or sediment. Several techniques can be used to achieve this result: electrostatic repulsion and steric hindrance are the main used.

Electrostatic repulsion consists on the adsorption of charged species on the surfaces of particles, this ending into the generation of repulsive forces that keep the particles away from each other.

Steric hindrance consists in adsorbing a deep layer of polymeric chains on the surfaces of colloidal element, which makes very difficult for the particles to get closer enough to develop attractive forces [25].

Polymers such as PEG can serve as stabilizers for metal colloids: they are able to form complexes with metal cations due to ether groups displayed on PEG chain, resulting in a more homogeneous mix [18].

In fig. 1.8 can be seen some processing option for sol-gel process.

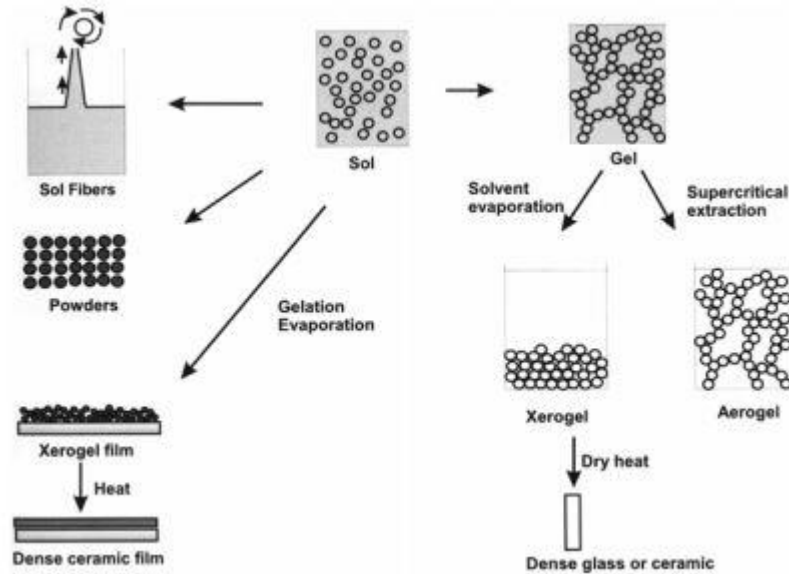


Fig. 1.8 Sol-gel processing options [25].

For what concerns hydroxyapatite application for sol-gel synthesis, 2 powders used are always precursors of  $\text{Ca}^{2+}$  and  $\text{PO}_4^{3-}$ , such as  $\text{Ca}(\text{NO}_3)_2 \cdot 4\text{H}_2\text{O}$  and  $(\text{NH}_4)_2\text{HPO}_4$ , same precursors that can be used also for precipitation method [21].

In fig. 1.9 is displayed a flow-chart for an example of possible sol-gel process aiming at synthesizing HAp.

The process can be carried out in control of pH (as usually happens when solution are prepared in distilled water), but in the same time can be in temperature control [26].

Another advantage of using the sol-gel method is that usually, the resulting powder can be easily sintered at a lower temperature compared to the typical temperature of  $1000^\circ\text{C}$  for sintering after a wet chemical precipitation technique, together with a reduced degradation of material [16].

On addition to that, sol-gel products are characterised by nano-size dimensions of the primary particle, that is a very important aspect that can improve the contact reaction and the stability at the interface bone/artificial HAp [16].

Usually typical drawbacks of sol-gel method can be found in the high cost of raw materials and to the strict control of pH that has to be performed to enhance the process.

For being a versatile, easy technique, with parameters that can be simply controlled without the need of complicate and expensive equipment, together with affordable raw materials, this method has been chosen for the HAp synthesis in the project of this thesis.

Later in the section '2. Materials and methods' will be presented the parameters of the specific sol-gel technique used.

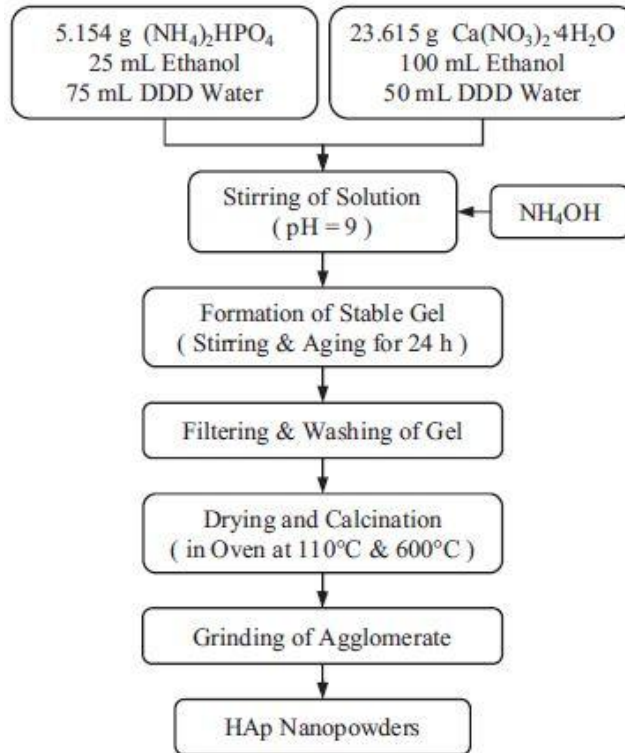


Fig. 1.9 Flow chart of sol-gel process [21].

Particle size of the sintered HAp is crucially important to achieve the best result possible. So this topic will be handles in next section.

### 1.5 Nanometer size

Nowadays, as it is proved the improvement of performance in many fields when using nanotechnology, several branches spread out. For this reasons, materials have been developed in several shapes according to the application needed: nanowires, nanorods, nanospheres, nanotubes, nanoparticles, quantum dots and hollow spheres are just some of many.

In medicine several unsolved problems of the past now have a solution thanks to the development in nanoscience. Application in medicine is so important, that a branch related to it was born: nanomedicine.

In this regard, nanotechnology is used in medicine for diagnosis and therapies, as well as in regenerative medicine and tissue engineering [27].

Another branch largely affected is analytical chemistry due to the providing of new detector based on nanotools that allows to be more accurate in analysis, this leading to an expansion of the possibility of investigation [29].

Nanoscience is a very multidisciplinary topic by now, collecting people with any kind of different preparation: engineering, medicine, chemistry, physic, biology. This also because the information that can be collected using nanotools are of different types: chemical (e.g., chemical composition, chirality, reactivity, bonds, etc); physical (e.g., dimensions, physical properties, surface topography, etc.); biological features mainly based on chemical reactivity (e.g., toxicity, membrane diffusion, bio-transformations, interaction with cells and microorganisms, etc.); and the final physic-chemical structure[29].

Quantitatively talking, it is considered nanoscale everything with a dimension in the range of 1-100 nm. At this scale characteristic of materials are different from those of individual atoms, molecules

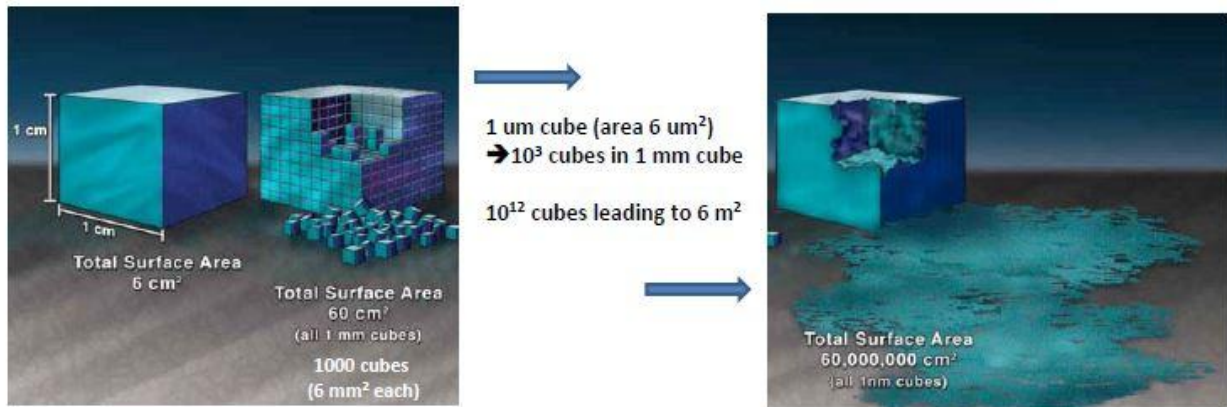


Fig. 1.10 Increase of surface area at the nanoscale [28].

and bulk atoms. On addition to that, the higher surface area implies higher surface activity by which catalysis and chemical reaction are faster [27].

In fig.1.10 it is displayed how passing to nanoscale can substantially increase the surface area.

There are some materials that when passing from the micro to nano scale they just exhibit a different behaviour because of the reduction of dimension and some other also exhibit changes in properties.

These two types of materials are fundamental, because the design can be based in the benefits coming from nanosize, from the change in properties of both [29].

In this work, hydroxyapatite nanoparticles were produced following a sol-gel process. The choice of nanometer size has the goal of changing the magnetic properties, reducing the amount of domains and possibly achieving a super-paramagnetic behaviour. On addition to that scaling to this dimension, bioactivity and reactivity of the surface increase.

The next paragraph deals with magnetism, it is considered interesting to pass through the general topic of magnetism and magnetic properties of materials for a better understanding of the main purpose of this project.

### 1.6 Magnetism, general introduction

Being an electron a moving charge in its revolution around the nucleus, it generates a magnetic moment along the axis of rotation. Furthermore, due to the spin of the electron, another magnetic moment is generated along the spin axis. The concurrence of these two moments determine a different magnetic behaviour according to the type of material considered [31].

Before dealing with the magnetic behaviour, it is important to present a focus on magnetic moment and dipoles.

A magnetic dipole, analogously with the electric one, can be described as 2 monopoles of opposite strength separated by a certain distance. However, a magnetic monopole doesn't exist in nature. If there are  $N$  monopoles all located at a point given by the vector  $\vec{a}$ , then the magnetic dipoles is a vector  $\vec{u}$  given by the equation 1.1

$$\vec{u} = \sum_{i=1}^N \vec{m}_i \vec{a}_i \quad \text{Equation 1.1}$$

A bar magnet can be considered as two opposite equal poles at its ends [32]. ‘ $\bar{m}$ ’ indicates the elementary magnetic quantity. In particular in equation 1.1 it is taken every  $\bar{m}$  corresponding to a different magnetic moment inside the material to calculate the dipole moment of the entire material.

An external magnetic field applied on a material interacts with dipole moments and tends to align them, increasing the magnitude of the field strength. This increase can be described by the equation 1.2:

$$\mathbf{B} = \mu_0 \mathbf{H} + \mu_0 \mathbf{M} \quad \text{Equation 1.2}$$

Where M is the magnetization and can be described as the density of magnetic dipoles for unit volume, as can be seen in the equation 1.3.

$$\mathbf{M} = \frac{d\mathbf{m}}{dV} \quad \text{Equation 1.3}$$

The magnetic response of the material depends on atomic structure and temperature and this is quantified by the equation 1.4.

$$\mathbf{B} = \chi_0 \mathbf{H} \quad \text{Equation 1.4}$$

Depending to the alignment and disposition of dipole moments in presence or not of an external field, materials can be classified in 3 main groups: diamagnetic, paramagnetic and ferromagnetic.

Diamagnetism is a weak form of magnetism which arises just when an external field is applied. There are no magnetic dipoles when no field is applied but dipoles are activated when a field is applied, orienting opposite to the applied field H. It is possible to see this behaviour in fig. 1.11 [31].

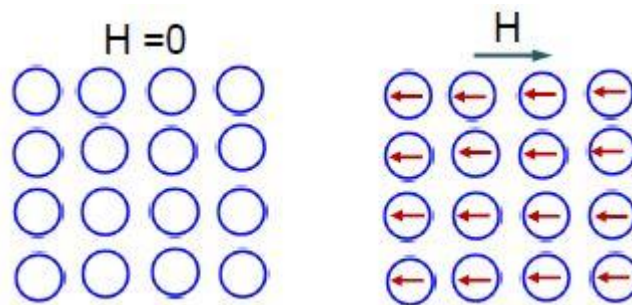


**Fig. 1.11** Diamagnetic behaviour [31].

In a diamagnetic material magnetic susceptibility is negative and smaller in module than that of vacuum. For this reason, they are repulsed by a magnetic field.

A paramagnetic material shows the presence of magnetic moments due to the presence of incomplete cancellation of magnetic moments between electron pairs. However, remaining moments are randomly aligned, this resulting in no magnetic behaviour without an external field applied.

Moreover, when a field is applied, unpaired couple of electrons they orientate in the direction of the applied field, causing all the dipole moments to be aligned in the same direction. In this case, magnetic susceptibility is positive and greater in module than that of vacuum[31], being this way attracted by a magnetic field [32]. In figure 1.12 is shown paramagnetic behaviour.

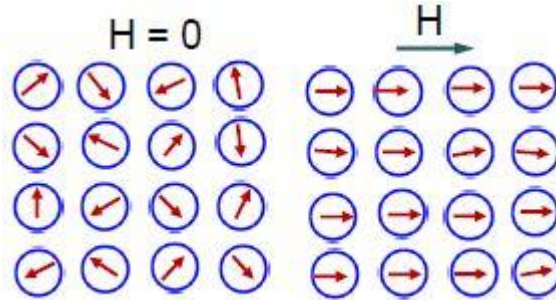


Fig. 1.12 Paramagnetic behaviour [31].

Magnetic moments can arise if there are phenomena of un-cancelled electron spin, due to the particular electron structure. In these cases, the material considered is ferromagnetic and shows the presence of permanent magnetic moments in the absence of external magnetic field applied. The interactions of adjacent coupling electrons cause the alignment of the moments. The presence of unpaired couple of electrons derives from the electronic structure. Ferromagnetic materials such as Fe have incompletely filled d electronic orbits and hence unpaired electronic pairs [31].

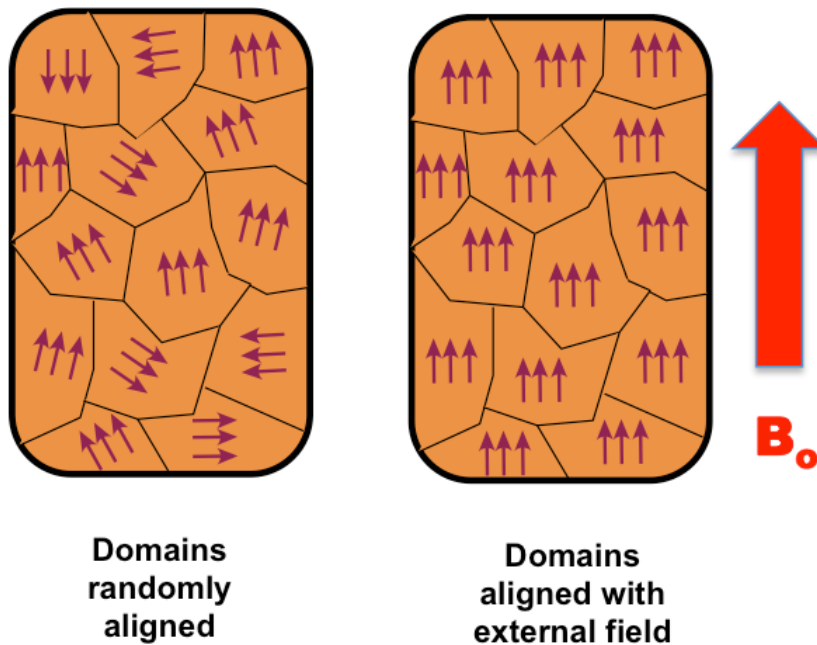


Fig. 1.13 Ferromagnetic behaviour in presence of external field [33].

As can be seen in fig. 1.13, in ferromagnetic materials are characterised by the presence of magnetic domains. They are small areas of material in which magnetic moments are aligned in the same direction. Within the same domain, magnetic moments are aligned in the same direction, that can be different from the alignment in other domains, unless an external field is applied. In this case, in a

ferromagnetic material all the domains show the same orientation for their magnetic moment. Only materials showing natural alignment of dipoles due to interaction between electron pairs show the presence of domains. Besides of ferromagnetic, also antiferromagnetic and ferrimagnetic materials have domains.

Diamagnetic and paramagnetic materials don't have domains, because they don't show magnetic moments without an applied external field.

In antiferromagnetic materials coupling of electrons pairs are aligned in antiparallel way, resulting to cancellation of spin. In this case, no magnetic moment arises.

An example of this behaviour is MnO, in which  $O^{2-}$  doesn't show a magnetic moment and in  $Mn^{2+}$  spins are antiparallel, leading to a magnetic moment equals to zero (fig. 1.14) [31].

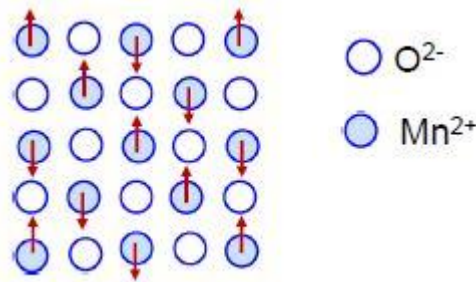


Fig. 1.14 Antiferromagnetic behaviour [31].

Ferrimagnetism is quite similar to ferromagnetism: in both case the final result is an oriented magnetic moment, but it is formed in 2 different ways. In ferromagnetic materials derives from the orientation of all the magnetic dipole in the same direction. On the contrary in ferrimagnetic, some of the dipole are oriented in opposite way, but the cancellation of opposite dipoles leads to a remaining net magnetic moment [31]. This is better understandable looking at fig. 1.15.

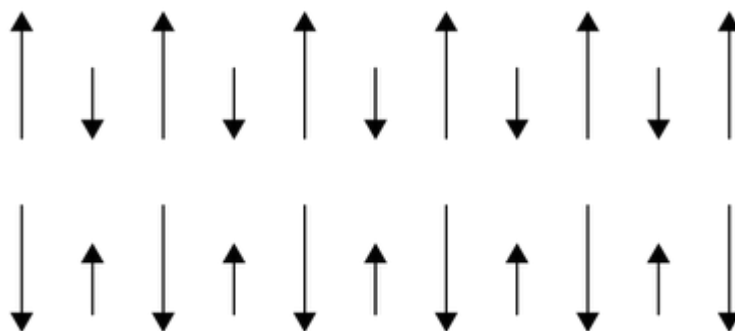


Fig. 1.15 Ferrimagnetic behaviour [34].

Ferromagnetic, ferrimagnetic and antiferromagnetic behaviour depends on temperature. In fact, above a certain temperature that is typical of each material, they also turn into paramagnetic materials.

This temperature is the Curie temperature  $T_C$  for ferromagnetic and ferrimagnetic and the Neel Temperature for antiferromagnetic.

All of the above is resumed into fig 1.16.

<b>Ferromagnetic</b> 	Below $T_C$ , spins are aligned parallel in magnetic domains
<b>Antiferromagnetic</b> 	Below $T_N$ , spins are aligned antiparallel in magnetic domains
<b>Ferrimagnetic</b> 	Below $T_C$ , spins are aligned antiparallel but do not cancel
<b>Paramagnetic</b> 	Spins are randomly oriented (any of the others above $T_C$ or $T_N$ )

Fig. 1.16 Resume of magnetic behaviours [35].

The main interest of this work is that doped hydroxyapatite with suitable ions is able to show super-paramagnetic behaviour, which is essential for hyperthermia. For this reason, now super-paramagnetism is treated more deeply.

### 1.7 Super-paramagnetism

Considered a ferromagnetic material, dimension can highly influence the division in different domains of the particle.

Considering a spherical particle, scaling the dimension the number of domains reduce until all the domain wall are removed. At this point, by reducing more the dimension it is possible to arrive to a single domain case, in which the entire particle is made up of just one domain.

It is in this state that the particle is able to show super-paramagnetic behaviour.

In fig.1.17 can be seen how is the domain division at different dimensions[37].

This happens because below a certain radius it is more favourable from an energetic point of view to have a monodomain state.

Moreover, the gain in energy of the division into domains is less than that derived from the formation of domain walls [38].

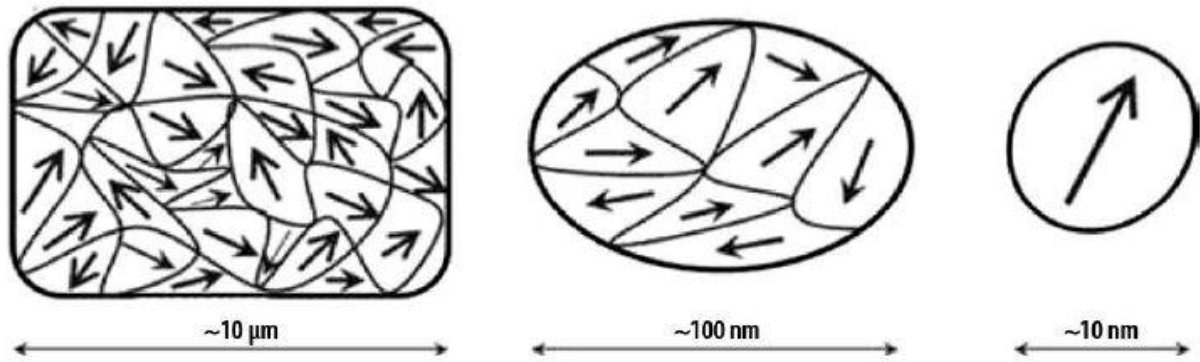


Fig. 1.17 Domain distribution at different particle dimension [37].

According to literature, it is possible to build the equation 1.5 related to magnetic domains.

$$\mu_0 \frac{\pi}{4} r^2 M_S^2 = \gamma 2r + \mu_0 \frac{1}{\pi} r^2 M_S^2 \quad \text{Equation 1.5}$$

Elaborating equation 1.5 it is possible to obtain equation 1.6 to calculate critical radius.

$$r_C \approx 35 \frac{\sqrt{AK}}{\mu_0 M_S^2} \quad \text{Equation 1.6}$$

where:

- A is called exchange stiffness and is a measure for the critical temperature for magnetic ordering of this specific material;
- K is the magnetic anisotropy of the particle;
- $M_S$  is the saturation magnetization. This quantity is relevant since in a single domain particle magnetization is always saturated, with or without the application of an external field.

Using this equation is possible to approximately calculate the critical radius for some typical super paramagnetic materials. Results are shown in fig. 1.18 [38][36].

	$r_c$ [nm]	$\gamma$ [ $10^{-3} \text{ Jm}^{-2}$ ]
$\alpha$ -Fe	5.8	2.1
Co	27.8	7.84
Ni	11.3	0.39
$\text{Fe}_3\text{O}_4$	6.2	2.0
$\text{CrO}_2$	90	2.0
$\text{SmCo}_5$	585	57

Fig. 1.18 Critical radius for some super-paramagnetic materials [38].

Nanoparticles with uniaxial anisotropy randomly flip the direction of their magnetization and this process is thermally activated. It is possible to define the relaxation time as the average time necessary to perform this flip. The equation 1.7 described the relaxation time.

$$\tau = \tau_0 \exp\left(\frac{\Delta E}{k_b T}\right) \quad \text{Equation 1.7}$$

Where:

- $\tau_0$  is the typical relaxing time of the considered material, usually it is a value between  $10^{-9}$  and  $10^{-12}$ s;
- $\Delta E$  is the required energy for the flip;
- $k_b$  is the Boltzmann constant;
- $T$  is the considered temperature.

Usually experimental measures indicate also the typical time of measurement  $\tau_m$  that is essential for the interpretation of the nanoparticles system behaviour.

If  $\tau_m$  is smaller than  $\tau$ , the time of the measure is smaller than the average time necessary for one flip. This means that the particle is in a well-defined state: the blocked state.

If on the contrary  $\tau_m$  is higher than  $\tau$  time of the measure is enough to allow magnetization flip. If there is no external field applied the average value of magnetic moment is zero. This is the super-paramagnetic state [36].

Through equation 1.7 it is possible to obtain equation 1.8 through which can be calculated the blocking temperature, that is the between the blocked state and the super-paramagnetic state.

$$T_B = \frac{\Delta E}{k_B \ln\left(\frac{\tau_m}{\tau}\right)} \quad \text{Equation 1.8}$$

When  $T < T_B$  blocked state is activated.

On the contrary when  $T > T_B$  particles are in super – paramagnetic state [36].

In fig. 1.19 the difference between the 2 states is shown.

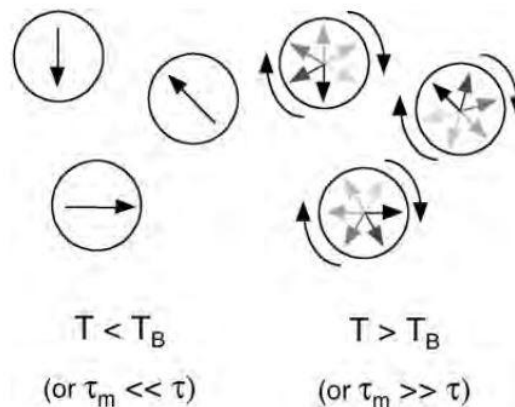


**Fig. 1.19** Blocked state (on the left) vs super – paramagnetic state (on the right)

Different types of magnetism are characterized, as seen before, by different values of magnetic susceptibility, below it is shown a resume of it.

Ferromagnetic, ferrimagnetic and antiferromagnetic materials present strong order with respect to the alignment of magnetic moments. They present a large value of  $\chi$ .

On the contrary in diamagnetic and paramagnetic materials magnetic moments are aligned just in presence of an external field. Diamagnetic on the opposite direction of the applied field ( $\chi < 0$ ) and paramagnetic on the same direction ( $\chi > 0$ ).

According to these different types of magnetism, they show a different behaviour in  $\vec{M}$  varying the external field  $\vec{H}$  [36].

When an external field is applied to a super – paramagnetic particle, as with paramagnetic particle magnetic moments start to align with the applied field, faster than what happened with paramagnetic materials due to the higher value of  $\chi$ .

In particular, two cases can be studied according to the situation and depending on the temperature.

- In case  $T_B < T < KV / 10k_B T$ , all easy axes orientate in direction of the field and magnetization is described through the equation 1.9

$$M(H) = n m \tanh\left(\frac{\mu_0 H m}{k_B T}\right) \quad \text{Equation 1.9}$$

- In case  $KV/k_B T < T$ , all axes are now oriented and magnetization is described with equation 1.10.

$$M(H) = n m L\left(\frac{\mu_0 H m}{k_B T}\right) \quad \text{Equation 1.10}$$

Where:

- $\Delta E = KV$  with K constant of anisotropy and V as the volume of the particle;
- n : density of nanoparticles in the sample;
- m : magnetic moment of the nanoparticle;
- L(x) : Langevin function depending on x [39].

The difference of the function is shown in figure 1.20 [36].

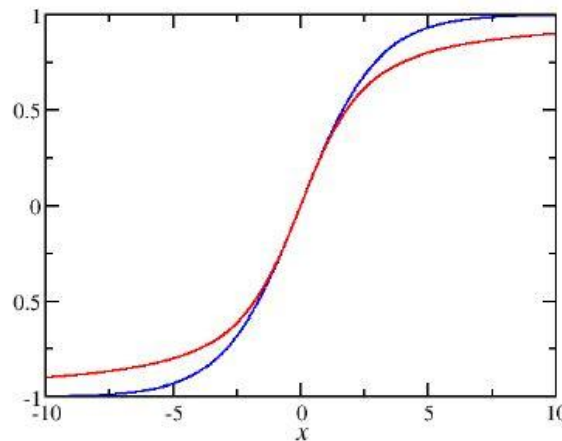


**Fig. 1.20** Comparison between  $\tanh(x)$  (blue line) and  $L(x)$  (red line).

Magnetic susceptibility of super – paramagnetism in the 2 cases above is described as follows [36].

- For  $T_B < T < KV / 10k_B T$  it is as stated in equation 1.11.

$$\chi = \frac{n\mu_0 M^2}{k_B T} \quad \text{Equation 1.11}$$

- For  $KV/k_B T < T$ , it is as described in equation 1.12.

$$\chi = \frac{n\mu_0 M^2}{3k_B T} \quad \text{Equation 1.12}$$

In figure 1.21 all the typical M-H curves for the different kind of magnetism treated before are presented.

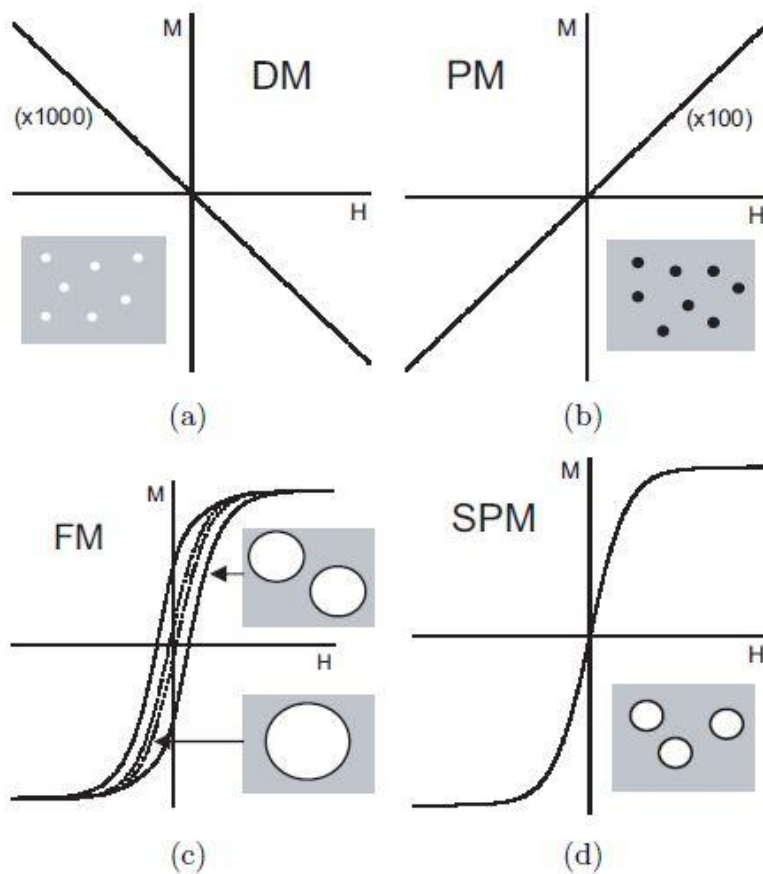


**Fig. 1.21** Magnetization curve for different type of materials in external field: (a) is diamagnetic material; (b) is paramagnetic material; (c) is ferromagnetic material; (d) is super-paramagnetic material. Interesting to underline that ferromagnetic material and superparamagnetic material show both the same sigmoidal shape, but in the ferromagnetic there is the loop typical of the hysteresis, while in superparamagnetic there is just one line [36].

As can be seen in figure 20(d), the curve doesn't show hysteresis, this implies that when external field is removed, magnetization drops to zero. On the contrary, ferromagnetic materials still show remaining magnetization when the external field is removing.

Curie temperature exists also for super-paramagnetic materials, this meaning that above a certain temperature a paramagnetic behaviour is displayed.

There are 2 critical temperatures for a super-paramagnetic behaviour: blocking temperature and Curie temperature.

In fig. 1.22 different magnetization curve in different states according to the temperature considered, are represented[38].

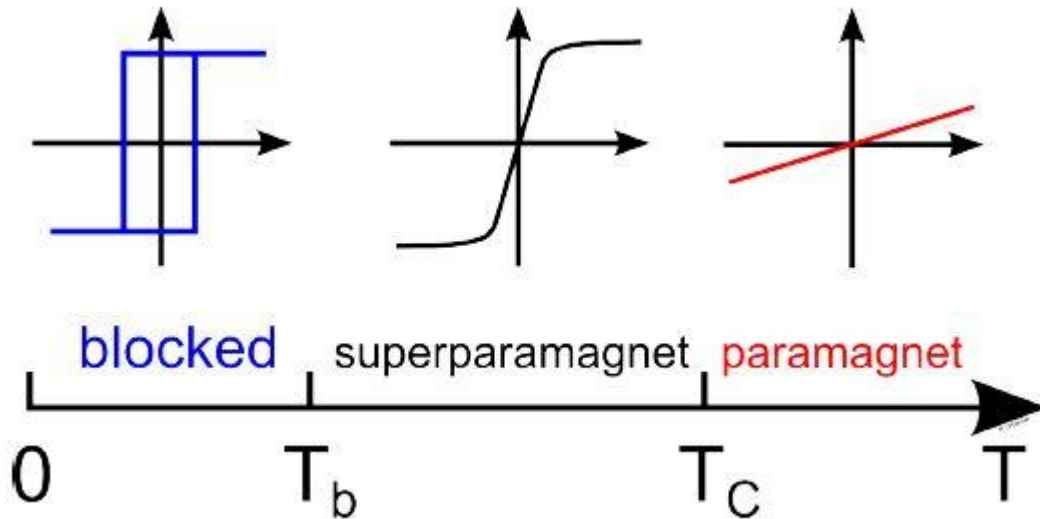


Fig. 1.22 Different M-H curves and different behaviour of the super-paramagnetic material according to the temperature[38].

As said before, the goal of this work was to produce super-paramagnetic hydroxyapatite nanoparticles, by doping normal hydroxyapatite with iron. One possible application, magnetic hyperthermia, will be treated in next paragraph.

### 1.8 Magnetic hyperthermia

Potential of hyperthermia in cancer cell treatment derived from the observation that several tumoral cells are more sensitive to temperature increase above 42°C than their normal cells counterparts. The most important aspect in magnetic hyperthermia is to control the heat variation and intracorporeal temperature increase in order to avoid overheating phenomena that could damage health cells.

Magnetic fluid are suspensions of monodomain magnetic nanoparticles (between 1-100 nm size). A stabilizing agent provides particles from aggregation. These particles are able to produce around 1000 more heat per unit mass if compared to multidomains materials, when exposed to alternating magnetic field. The mechanism of heat is based on the Brown effect and Néel effect, that will be explained later [40].

According to the dimension of the magnetic material involved, there could be different heating mechanisms. These mechanisms are eddy currents (Foucault currents), hysteresis loss and Brown and Néel effects.

Relating to material's dimensions, some of them are negligible.

Eddy currents induction takes place whenever a conductor is exposed to an altering magnetic field generating resistive heating. For magnetic materials, relevant eddy currents are detected just for

bulk material with a dimension bigger than 1 mm. For this reason, they are negligible in nanoparticles [43].

In case of multidomain materials, when applied an external magnetic field, all domains try to align in the direction of the field. Increasing the field imposed, more and more domains align, till the evolution to the magnetization saturation. At this value of field, all domains are aligned.

In fig. 1.23 a hysteresis curve is presented, along with response to an external field of other kind of magnetism.

When from the position of magnetization saturation field is gradually reduced, when it drops to zero a certain magnetization remains. Indeed, it is necessary to apply an opposite field to make the magnetization evolving to zero again [43].

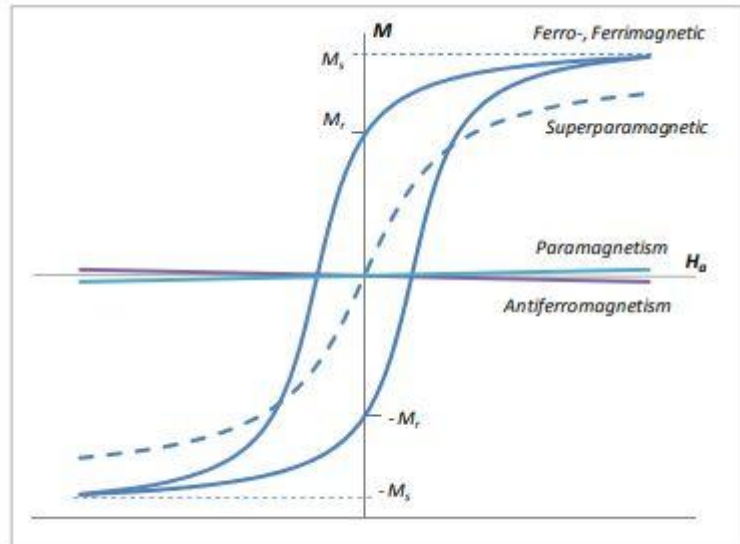


Fig. 1.23 Magnetization curve related to different kind of magnetism [43].

This kind of loss just interests multidomain materials.

For what concerns super-paramagnetic nanoparticles the most important effects for heating are Brown and Néel effects.

Brownian relaxation relates to the friction that liquid opposes when particles rotate due to the external field. As the whole particle oscillates towards the field, the liquid medium opposes this rotational movement resulting in heat generation [43].

The Néel mode represents the rotation of the individual magnetic moments towards the alternating field. Upon application of an external field, magnetic moment rotates away from the crystal axis, aligning to the field direction, minimizing potential energy. The remaining energy is released in form of heat [43].

In fig. 1.24 is displayed a summary of all the mechanisms presented above.

The best performance was found until now in nanocrystal magnetite, this being also the most investigated material for this application [44].

For what concerns the amount of material needed, it may vary according to the specific application and the way particles are dispensed in the intervention area. By direct injection is possible to accumulate larger quantities (always avoiding aggregation between particles) directly on the spot. On the contrary with intravascular and antibody targeting needs larger overall quantities, because the distribution is less efficient [36].

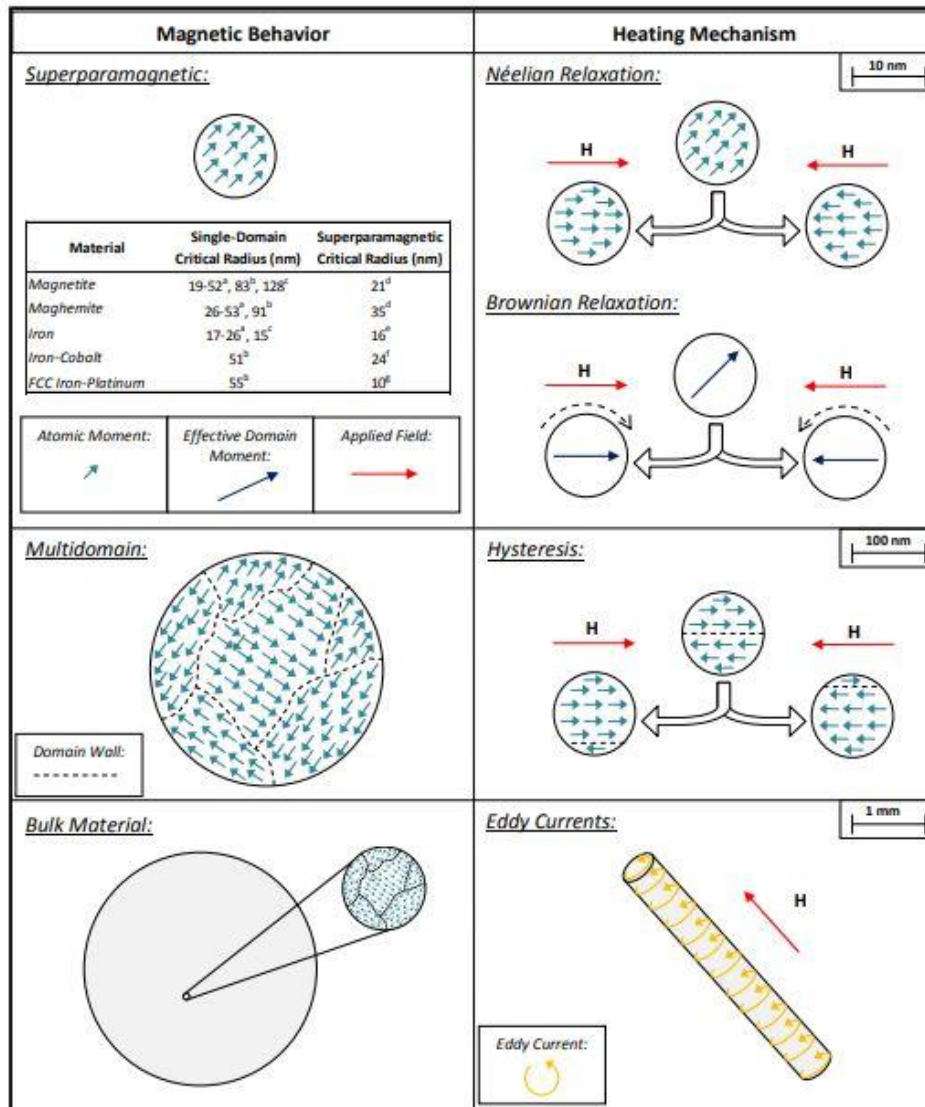


Fig. 1.24 Summary of heating mechanism [43].

In general, magnetite particles of diameter of around 10 nm or less are considered to be small enough. According to the structure (multidomain or monodomain) a different heating system will take place, describe with a different equation.

Two heating mechanisms are explained below.

Heating mechanism for ferromagnetic particles is principally caused by hysteresis loss. It can be described through the equation 1.13.

$$P_{FM} = \mu_0 f \oint H dM \quad \text{Equation 1.13}$$

With:

- f is the frequency of the magnetic field;
- the integral loop is over the hysteresis loop.

In the case of super-paramagnetic particles, the equation describing the power loss (generated heat) is displayed in equation 1.14.

$$P_{SPM} = \mu_0 \pi f \chi'' H^2 \quad \text{Equation 1.14}$$

Where  $\chi''$  derived from the decomposition of the magnetic susceptibility in the two component on-phase  $\chi'$  and out of phase  $\chi''$ .

Heat absorption from the tissue is usually given in term of W/g. Quantitatively talking, heating mechanism with ferromagnetic particle usually can generate around 75 W/g while super-paramagnetic particles can generate till around 200 W/g [36].

In literature several successful attempt of producing and using hydroxyapatite nanoparticles with super-paramagnetic behaviour can also be found, after iron doping. More specifically, hydroxyapatite shows a better bioactivity and less blood toxicity when compared to magnetite.

The next paragraph deals with the state of art of iron doping technique for hydroxyapatite.

### 1. 9 Iron doped Hydroxyapatite: state of art

As already stated, the main goal of this project is to develop iron-doped hydroxyapatite nanoparticles using sol-gel method. In literature several attempts to synthesize hydroxyapatite using different methods can be found.

*Panseri et al* [45] investigated the possible positive influence of iron doped hydroxyapatite in the growth of osteoblast-cells. Hydroxyapatite was synthesized through neutralization in different concentration of Fe ions. Final results show not only a comparable osteoblast viability and morphology, but increased in cell proliferation when compared to a commercial HAp, even with the highest dose used.

Furthermore, exposing the Fe-HAp to a magnetic field during the experiment improves results obtained.

*Hou et al.* [46] tried to treat cancer cells on a mouse using iron-doped hydroxyapatite synthesized by co-precipitation technique. After 15 days of hyperthermia treatment the concentration of cancer cells was heavily reduced, showing how encouraging are these kind of nanoparticles for this application.

Fe ions can be with two different oxidation states:  $Fe^{2+}$  and  $Fe^{3+}$ . In the literature researches using each of them singularly or together can be found. Apparently in some of them, the simultaneous addition of both Fe ions together during hydroxyapatite nucleation minimize the formation of iron oxide as a secondary phase, still showing super-paramagnetic behaviour [47].

Crystal growth in iron-doped hydroxyapatite can be influenced by the application of an external field.

Oriented dendritic growth of brushite crystals was confirmed in the work of *Baskar et al.* [48]. Furthermore, presence of  $HPO_4^{2-}$  has been found in crystals grown without application of magnetic field. The disappearance of  $HPO_4^-$  occurs in the presence of a magnetic field, which also promotes a reduction of incorporated iron, leading to a different crystal morphology. Finally, nanoroughness of the crystal was also seen to increase on applying a magnetic field of the order of 0,1 T [48]. In fig. 1.25 the difference in crystal growth with field applied or not can be seen.

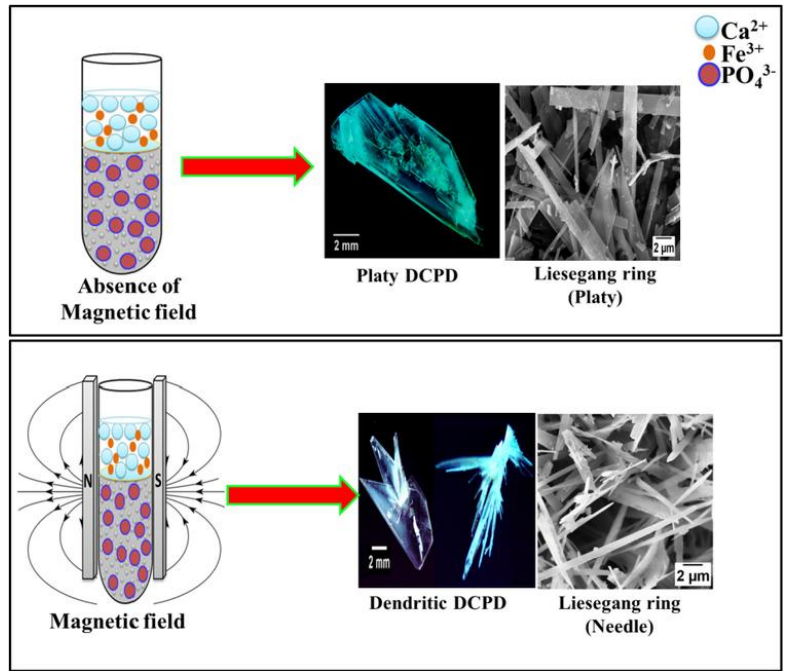


Fig. 1.25 Influence of magnetic field on crystal growth [48].

Iron ions substitution takes place in preferential sites. This has been investigated in several studies, this being prerequisite for a correct synthesis of the desired bioceramic with the proper Ca/P ratio. In this way it is also possible to predict its iron release and magnetic properties[49].

Calcium can be in two different positions in the hydroxyapatite lattice, coordinated in a different way. In fig. 1.26 these 2 calcium positions are shown.

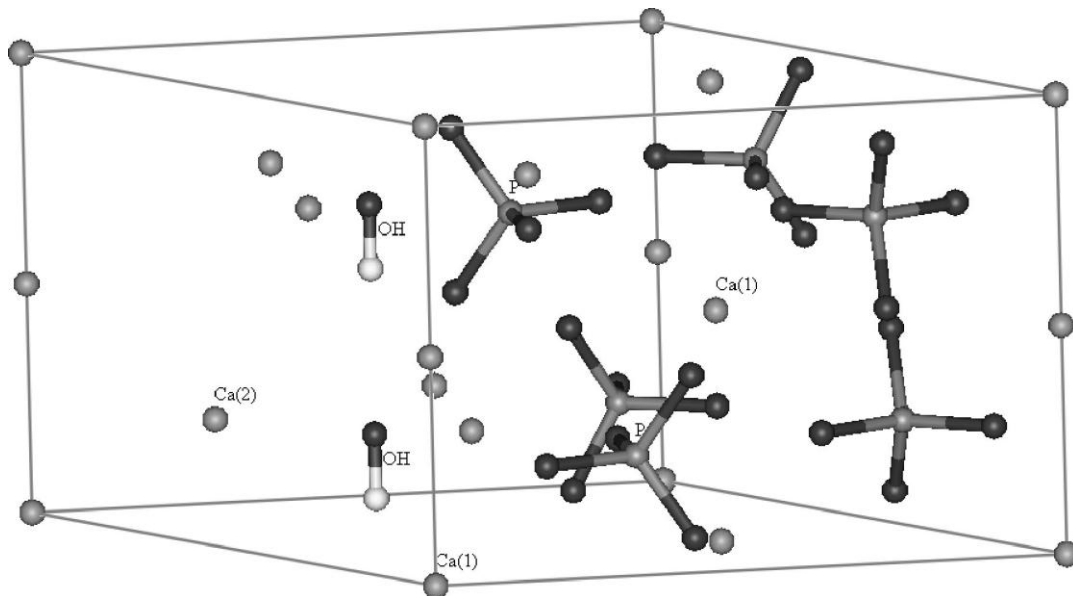


Fig. 1.26 Hydroxyapatite lattice. Ca(1) and Ca(2) positions are labelled [48].

Jiang *et al.* [48] investigated through atomic simulation possible positions of Fe ions substitutions into the lattice.

Moreover calcium can be in two different coordination states.

$\text{Ca}^{2+}$ , in the site Ca(1), is sixfold coordinated to 3O(1) and 3O(2). In fig 1.27 these two sites are displayed [48].

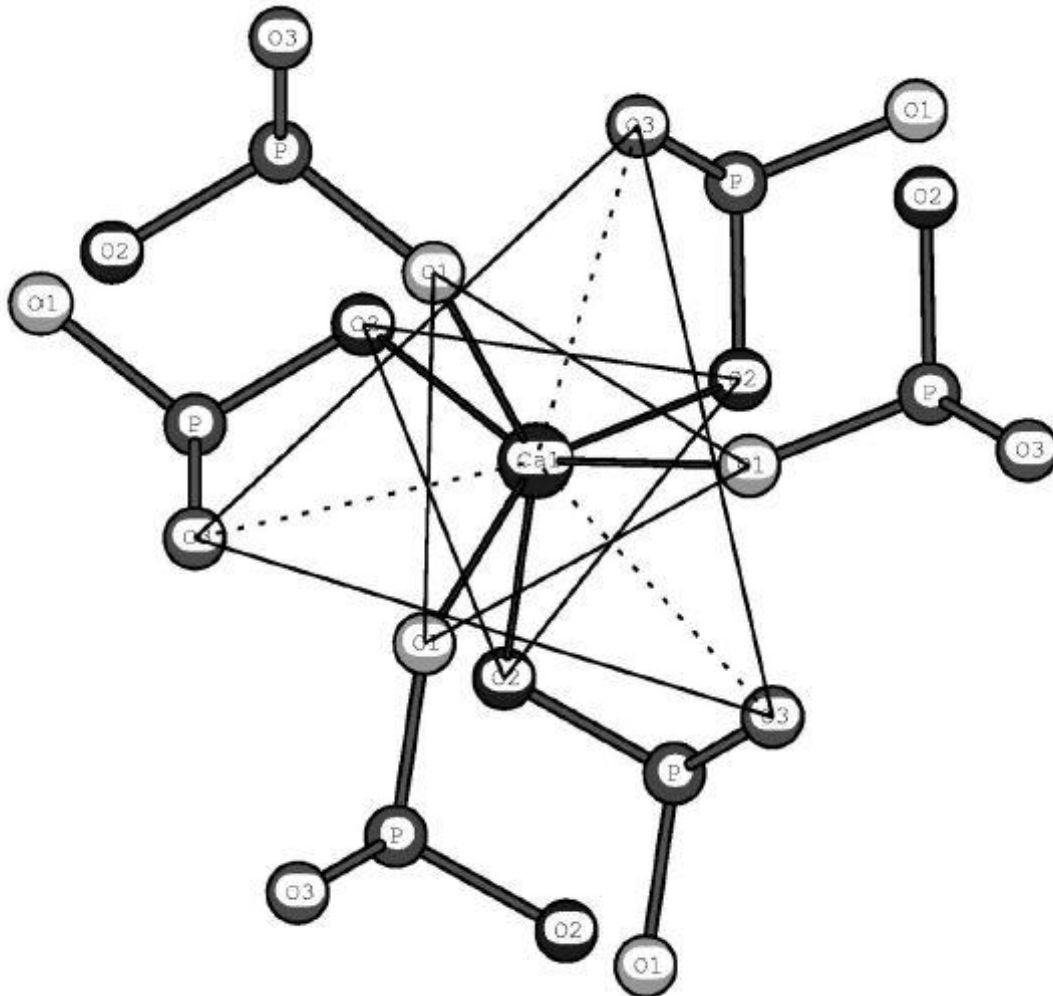


Fig. 1.27 Sixfold coordinated site called Ca(1) [48].

The other site Ca(2) is sixfold coordinated with 4O(3), O(2) and  $\text{O}_\text{H}$ . In fig 1.28 is showed how this site looks like in the lattice [48].

Studying the possible potential energies in each site for  $\text{Fe}^{2+}$  and  $\text{Fe}^{3+}$  a list of more favourable site and coordination for each ion can be done.

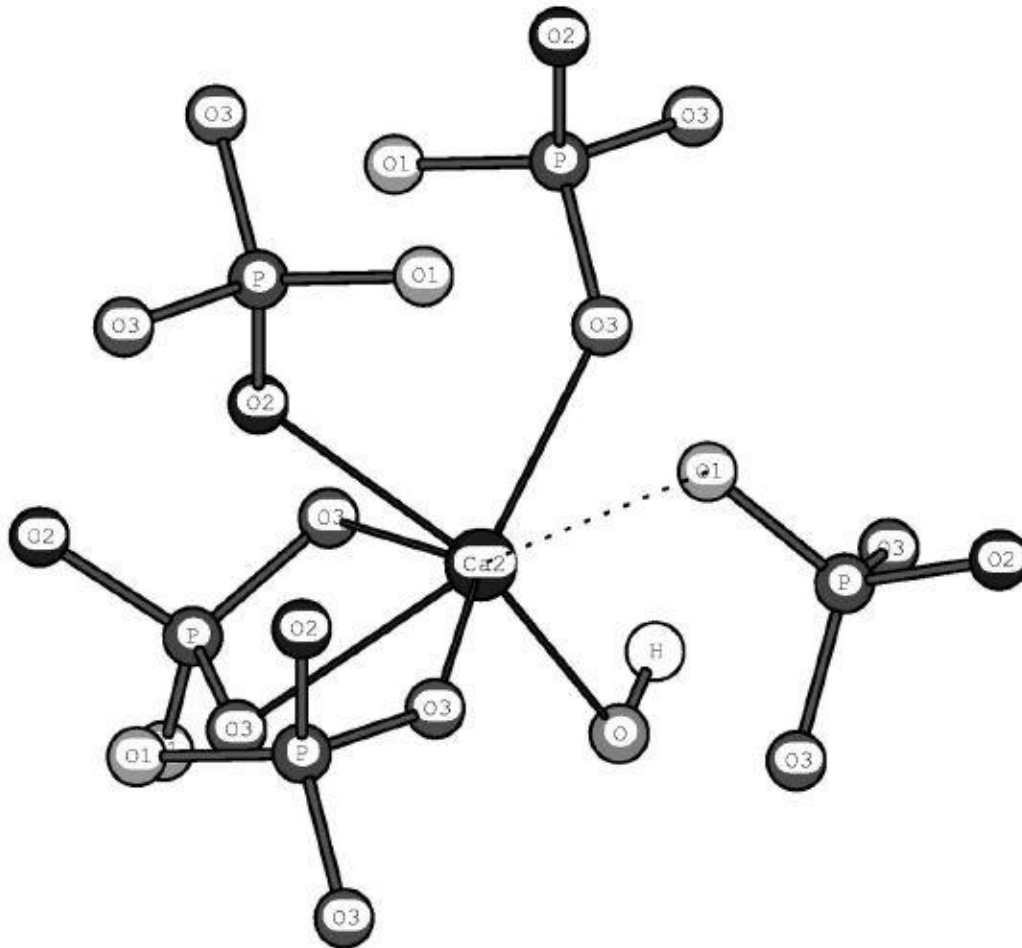


Fig. 1.28 sixfold coordinated site Ca(2) [48].

Being  $\text{Fe}^{2+}$  and  $\text{Fe}^{3+}$  characterised by a 3d electron configuration, they have flexible coordinations fourfold, fivefold and sixfold in their compounds.

Between the possible combinations, it has been discovered that in case of  $\text{Fe}^{2+}$  the most stable position is the sixfold coordinated centered in Ca(2), as it is shown in fig. 1.29.

On the other hand, considering  $\text{Fe}^{3+}$ , the most stable position is the fourfold coordinated in Ca(1) position, as it is displayed in fig. 1.30 [48].

These results have been reached considering Lennard-Jones potential parameters, comparing between each other their value, in order to create a hierarchy going from the lower to higher.

As potential is increasing, less stable is the configuration.

After that, results were confirmed Mossbauer and EPR spectra of the iron doped hydroxyapatite.

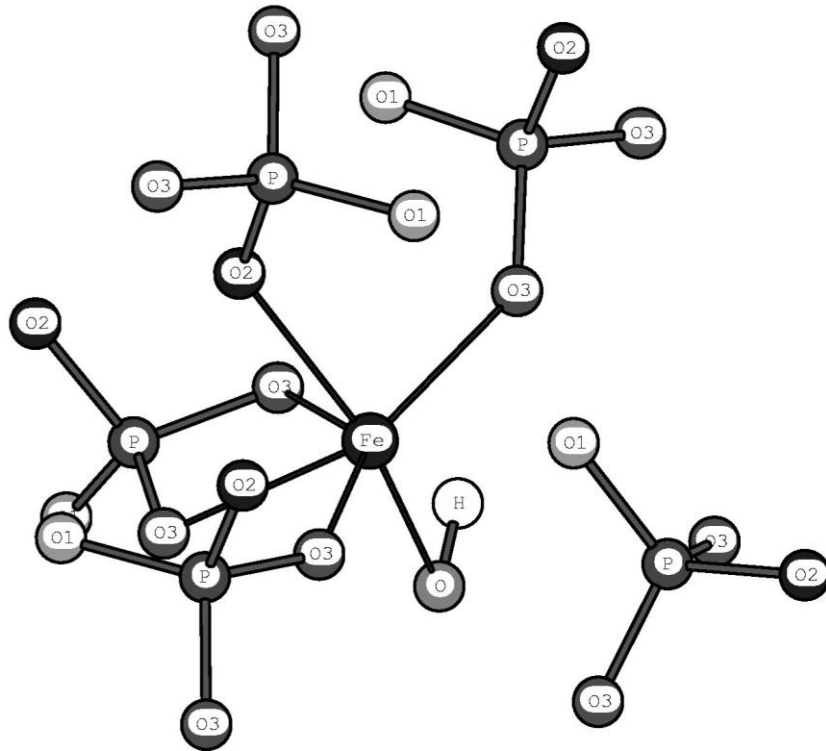


**Fig. 1.29** Sixfold coordinated site Ca(1) occupied by Fe<sup>2+</sup> ion [48].

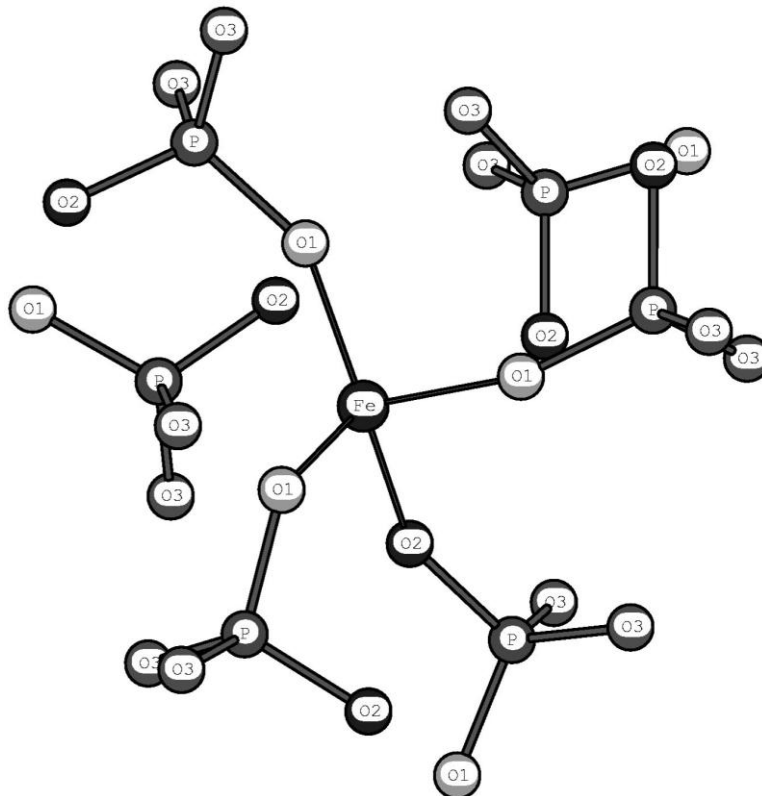


**Fig. 1.30** Fourfold coordinated site Ca(1) occupied by Fe<sup>3+</sup> ion [48].

After this theoretical background, next section deals with the experimental procedure performed.

*Gomes et al.* [49] objected what already stated, showing in their studies that Fe ions may also stay in other site inside hydroxyapatite. According to this theory,  $\text{Fe}^{3+}$  insert in hydroxyapatite lattice in different position according to temperature. In particular it stays in the interstitial 2b Wyckoff site up to  $1000^\circ\text{C}$  and shift from the (0,0,0) position to a (0.12,0,0) new position in the range of temperature  $1000\text{-}1100^\circ\text{C}$ .

In fig. 1.31 the two possible lattice organization with  $\text{Fe}^{3+}$  ions inside can be seen[49].

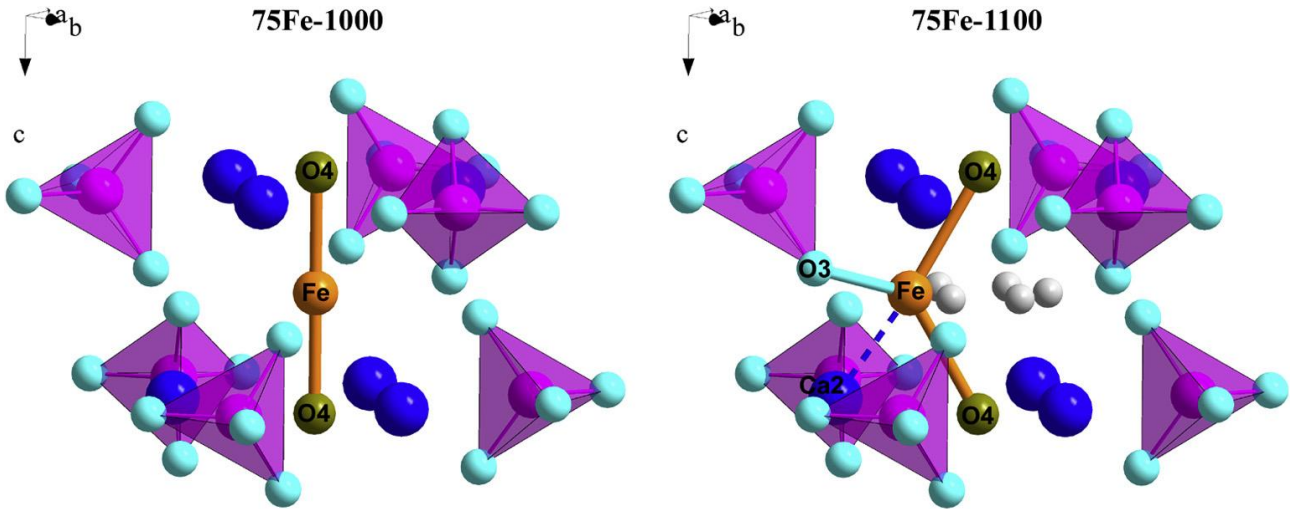


**Fig. 1.31** Structural details on the hexagonal channel passing from the  $1000^\circ\text{C}$  twofold configuration (left) to the  $1100^\circ\text{C}$  threefold configuration (right). Tetrahedra represent phosphate ions, large blue spheres represent calcium cations, green spheres represent hydroxyl sites from HAp structure and orange spheres represent iron cations. Small grey spheres (on the right) represent all the six equivalent points (0.12,0,0) positions all around the (0,0,0) position. Dotted line shows the shortest distance connecting  $\text{Fe}^{3+}$  and  $\text{Ca}^{2+}$ , according to crystallographic description [49].



## 2 Materials and methods

### 2.1 Fe – doped hydroxyapatite synthesis

Iron doped hydroxyapatite synthesis is performed following a standard procedure of the sol-gel method, with some variants to adapt it to the iron doping process. It is doped in two compositions with different quantities of Iron. An example of the standard sol-gel method taken as a reference is displayed in fig. 2.1.

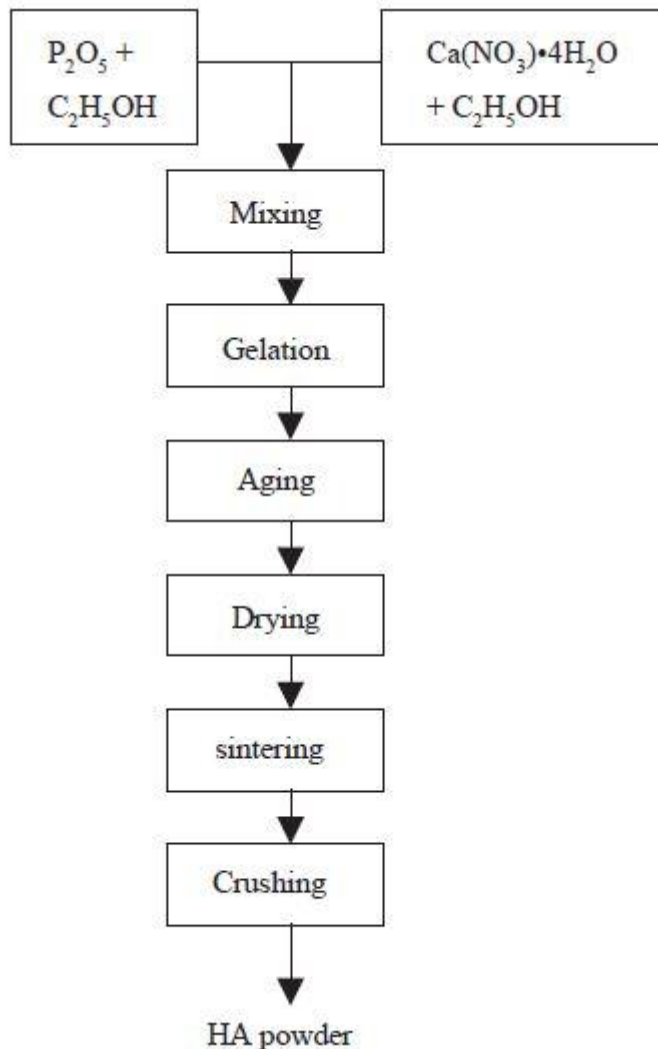


Fig. 2.1 sol-gel method for HAp synthesis. [51].

#### 2.1.1 Synthesis precursors

Precursors are supposed to provide all the chemical group needed to synthesize the final product. In this project Calcium nitrate tetrahydrate ( $\text{Ca}(\text{NO}_3)_2 \cdot 4\text{H}_2\text{O}$ , *Panreac*), Phosphorus pentoxide ( $\text{P}_2\text{O}_5$ , *Sigma – Aldrich*) that are the same precursors used for the normal hydroxyapatite have been chosen. To this, iron (II) Chloride tetrahydrate ( $\text{FeCl}_2 \cdot 4\text{H}_2\text{O}$ , *Sigma-Aldrich*) and iron(III) chloride exahydrate ( $\text{FeCl}_3 \cdot 6\text{H}_2\text{O}$ , *Sigma-Aldrich*) have been added as precursors of  $\text{Fe}^{2+}$  and  $\text{Fe}^{3+}$  ions.

### 2.1.2 Experimental procedure

Two different compositions are prepared following two different criteria. In this way two different iron doped hydroxyapatite in term of composition were synthesized. For both compositions some initial conditions have been chosen in order to estimate precursors quantities to use in the sol-gel technique. These initial conditions are resumed in table 2.1.

**Table 2.1** Molar ratio initial conditions.

	Sample 1	Sample 2
Ca/P	1,5	1,5
Fe <sup>3+</sup> /Fe <sup>2+</sup>	2	2
(Fe <sup>3+</sup> +Fe <sup>2+</sup> )/P	free	0,175
(Fe <sup>3+</sup> +Fe <sup>2+</sup> )/Ca	0,2	free

As can be seen from the table 2.1, there is always one ratio that is free. This is due to the fact that the 4 ratios considered are not linearly independent.

The amount of ethanol and the technique used are the same for both, just with different precursors quantities to fulfil the desired ratio.

The ratio between Ca/P is maintained in both composition at around 1.5, this being the critical ratio for solubility.

It is possible to calculate the two “free” quantities reported in table 2.1.

This resulting in (Fe<sup>3+</sup>+Fe<sup>2+</sup>)/P equals to 0,3. Moreover, the average ratio between the positive cations and P (Ca<sup>2+</sup>+Fe<sup>3+</sup>+Fe<sup>2+</sup>)/P in hydroxyapatite is 1,80, more than the usual 1,67 of normal hydroxyapatite.

For sample 2, it results Fe<sup>3+</sup>+Fe<sup>2+</sup>/Ca = 0,12 and (Ca<sup>2+</sup>+Fe<sup>3+</sup>+Fe<sup>2+</sup>)/P = 1,67.

Considering the same amount of calcium in both samples, it means sample 1 is characterised by a higher amount of iron ions, when compared to sample 2.

Final volume of ethanol is 20 ml for both samples. Quantities of precursors are then calculated and results are resumed in table 2.2.

**Table 2.2** Precursors quantities used for the synthesis.

	Sample 1 (g)	Sample 2 (g)
Ca(NO <sub>3</sub> ) <sub>2</sub> ·4H <sub>2</sub> O	7,08	7,08
P <sub>2</sub> O <sub>5</sub>	1,42	1,42
FeCl <sub>2</sub> ·4H <sub>2</sub> O	0,40	0,23
FeCl <sub>3</sub> ·6H <sub>2</sub> O	1,08	0,63

First step is to prepare one solution of Calcium nitrate tetrahydrate in 10 ml of absolute ethanol and another one of phosphorus pentoxide in 10 ml of absolute ethanol as well. These two solutions are then sealed and put 10 mins in magnetic agitation, in order to solubilise both compounds inside the ethanol.

Next passage is to add iron(III) chloride hexahydrate in the solution with calcium and iron(II) chloride tetrahydrate in the solution with phosphorus.

It was preferred to put bivalent iron in the solution containing phosphate, to reduce the risk of precipitation of salt, which could be more favourable in presence of trivalent iron.

After that two solutions are put again under magnetic agitation for 10 minutes.

When complete dissolution of powders is reached, both solutions are put in oil bath at 90°C until the formation of a gel, which takes approximately 1 hour.

Two solutions are then put in oven to dry at 80°C for 24 hours.

Finally, thermal treatment into the oven is performed at 3 different temperatures 600 °C, 700°C and 800°C, this resulting in a total of 6 different samples at the end of processes to be analysed.

Oven setting includes a first heating phase from room temperature to sintering temperature with a permanence of 1 hour at this temperature. Finally, samples are cooled to room temperature.

This specific treatment leads to a partial sintering of the powders and, in order to simplify, in the rest of the project it will be referred as “Sintering treatment”.

Finally using a mortar and a pestle, powders are homogenised and reduced in size.

## 2.2 Characterization technique

Characterization of properties is very important to understand possible use and potentialities of the material and its possible future developments.

On all the 6 samples are performed these analyses: X-Rays diffraction (XRD), Fourier transformed infrared spectroscopy (FTIR), Vibrating Sample Magnetometer (VSM) and hyperthermia analysis.

Beside these, cytotoxicity and bioactivity analysis were performed to estimate samples biocompatibility as well.

Finally, morphological and compositional analysis were performed with scanning electron microscope (SEM).

### 2.2.1 X-Ray diffraction

X-ray diffraction is a phenomenon of interaction between an incident electromagnetic wave and the material. To have diffraction of the wave in meeting atomic plane of the material it is necessary that the wavelength has the same dimension of the distance between adjacent planes that in this case is in Angstrom (Å).

To perform this analysis a diffractometer *X'Pert PRO PANalytical* is used. Spacing between two consequent measures of  $2\theta$  is 0,033 degrees ( $\theta$  is the diffractive angle). Scan is performed in the range of 10° - 90°.

Electromagnetic radiation is a Cu-K $\alpha$  type ( $\lambda=1,54060$  Å).

XRD technique allows to evaluate crystal structure as well as getting information about the possible phases present in the powders. Using this technique is also possible to gather information about crystallinity and cell parameters of the lattice cell. In order to do this it is necessary to know symmetry of the structure and atomic disposition thus its crystalline structure. Hydroxyapatite is a hexagonal symmetry crystalline structure.

It is also possible to evaluate crystallite diameter using Scherrer equation that is named here as Equation 2.1.

$$D = \frac{k\lambda}{\beta \cos\theta}$$

Equation 2.1

Where:

- D is crystallite diameter;
- k is a constant that in the case of hydroxyapatite is  $k = 0,9$ ;
- $\beta$  is the width at half height of the highest peak in the spectrum;
- $\theta$  is the angle related to the highest peak.

Furthermore, from x-ray diffractogram is possible to obtain cell parameters of the crystalline structure.

The equation needed is different, according to the crystalline structure of the considered material. In case of hydroxyapatite equation 2.2 is what must be used.

$$\frac{1}{d^2} = \frac{4}{3} \left( \frac{h^2 + hk + k^2}{a^2} \right) + \frac{l^2}{c^2} \quad \text{Equation 2.2}$$

Where:

- d is the distance between two consequent atomic plane and can be calculated through Bragg law (Equation 2.3);
- h,k,l are Miller indexes related to the unitary crystal cell and they can be obtained studying peaks of the diffractogram.
- a and c are the two desired cell parameters.

$$d = \lambda \cos \theta \quad \text{Equation 2.3}$$

Two peaks (002) and (300) are considered to calculate respectively c and a.

### 2.2.2 Fourier transformed infrared spectroscopy (FTIR)

It is a technique for recording absorption or emission spectrum of a solid, liquid or gas. It is used to collect information about chemical groups present in the compound considered.

The process consists of collecting an interferogram and its subsequent conversion to frequency data by inverse Fourier transform. The first spectrum collected is the background spectrum, because inside the solvent where the sample is placed there are traces of dissolved gases and solvent molecules. This background spectrum is useful, because it is then subtracted to the sample spectrum to obtain just the contribution of the sample.

In fig. 2.2 there is an example of a background spectrum.

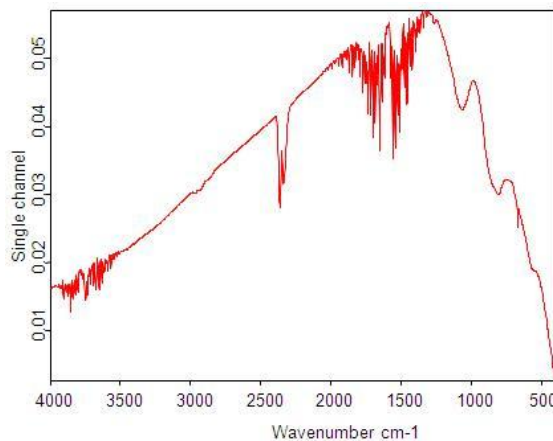


Fig. 2.2 example of a FTIR background spectrum [52].

After that the background spectrum is subtracted to the other one taken with sample and solvent. This way it is possible to obtain just the sample answer to infrared, similar to what can be seen in fig. 2.3 [52].

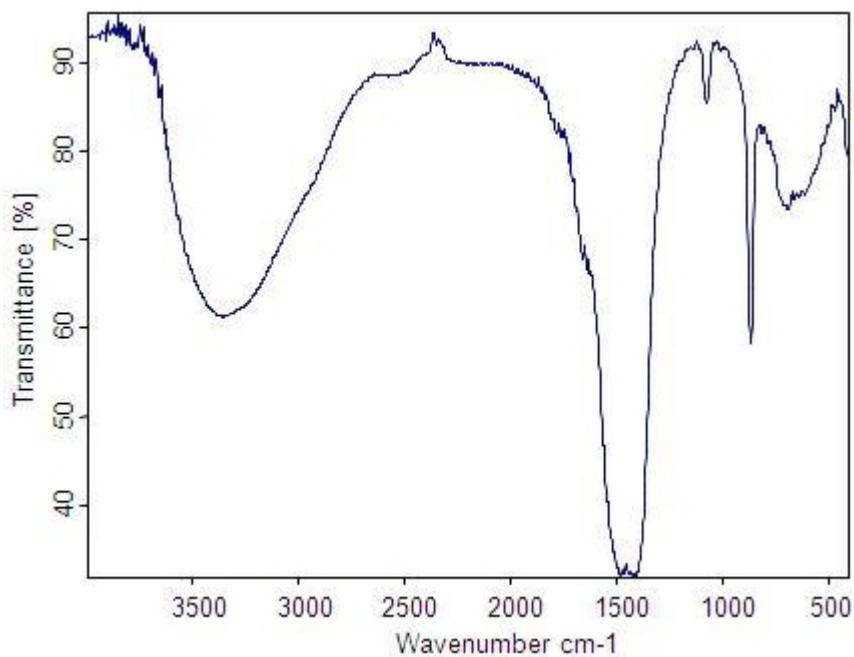
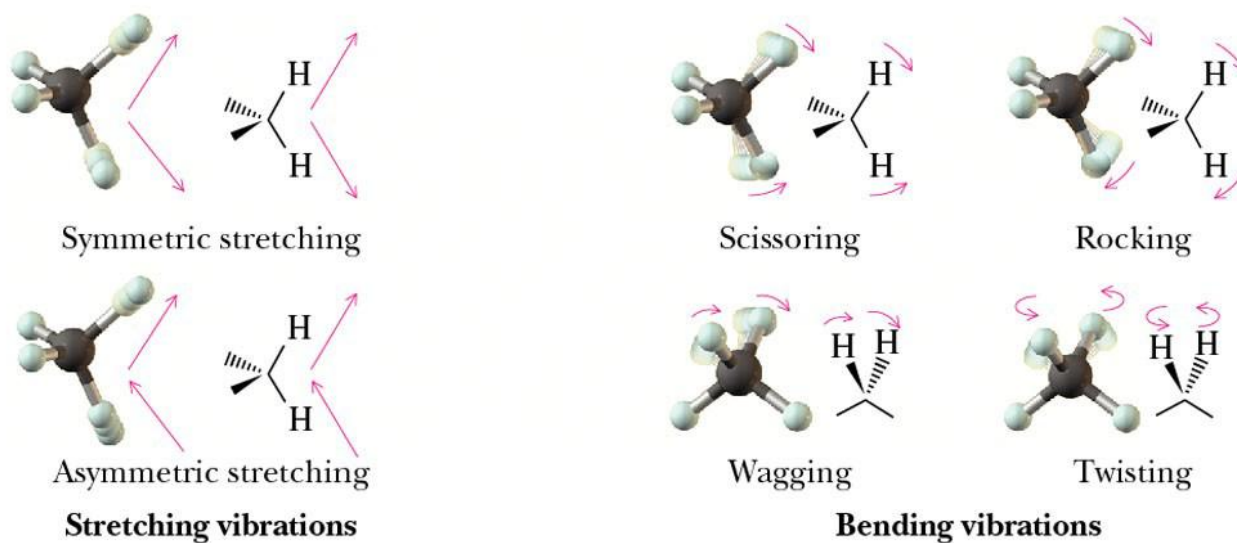


Fig. 2.3 example of a sample FTIR spectrum [52].

After the spectrum is available it is time to label various peaks according to which kind of molecular vibration they are related. Every peaks correspond to a molecular type of vibration related to one specific chemical group of the compound. There could be several types of vibration as resumed in fig. 2.4.

Infrared spectrum is formed in bands, showing the transition between different rotational levels, due to the radiation.



© 2006 Brooks/Cole - Thomson

Fig. 2.4 Resume of possible vibrational modes in molecules [53].

Movements IR activated are stretching, which consists in a variation of the bond length, and bending consisting in the variation in bond angle.

Labelling FTIR spectrum according to the energy related to each movement for the chemical groups of the compound considered is possible to have information about chemical composition of the material and its molecular arrangement.

The analysis was performed using the spectrophotometer *ATR-FTIR Nicolet 6700 – Thermo Electron Corporation Attenuated Total Reflec-tance-Fourier Transform Infrared Spectrometer*, in the range of 500-5000  $\text{cm}^{-1}$ . An incidence angle of  $45^\circ$  was used.

### 2.2.5 Vibrating sample magnetometer (VSM)

The sample is introduced inside where an applied external magnetic field which induces a magnetization in the sample. At this point the magnetized sample is vibrated, perturbing the external field of the instrument.

A set of coils can be arranged around the sample to measure this perturbation that determine a change in the magnetic flux piercing the coils, this leading to the formation of an emf (electro motive force).

For a particular coil geometry, emf depends on amplitude and frequency of vibration, external magnetic field and magnetization of the sample. Finally, it is possible to calculate the magnetization of the sample [54].

This analysis was performed in Aveiro University using magnetometer VSM-10 T(*Cryogenic-Cryofree*). Hysteresis curves are done at 7 K and 300 K with an applied field of  $\pm 2$  T.

### 2.2.6 Magnetic hyperthermia analysis

This test is performed to evaluate the actual capacity of the synthesized material to heat in presence of an external magnetic field. The objective is to produce materials with the property to warm up at least at  $43^\circ\text{C}$ , this being the temperature needed to kill cancer cells preserving the healthy ones.

For the purpose it is used the instrument *Nb Nanoscale biomagnetics*, with a fixed frequency of 418,5 kHz.

First step of the procedure is to dissolve powder of every sample in absolute ethanol with the ratio of 5% m/V. For this procedure is used 1 ml of ethanol and in table 2.3 is listed the amount of powder for each material.

**Table 2.3** quantity of powder used for the hyperthermia analysis.

Samples	Quantity of powder (g)
Sample 1 – $600^\circ\text{C}$	0,047 g
Sample 2 – $600^\circ\text{C}$	0,045 g
Sample 1 – $700^\circ\text{C}$	0,049 g
Sample 2 – $700^\circ\text{C}$	0,047 g
Sample 1 – $800^\circ\text{C}$	0,046 g
Sample 2 – $800^\circ\text{C}$	0,045 g

3 suspensions are prepared for each sample. They are then inserted into the machine able to record the difference in temperature within applying an alternate magnetic field with an intensity of 24 kA/m and frequency of 418,5 kHz. The test lasts 10 minutes.

### 2.2.7 Bioactivity test

It is necessary to evaluate the way samples interact with the organism. In order to do this, bioactivity test is performed putting all the sample in contact with a fluid able to simulate plasma present in the body. In fact, SBF (simulated body fluid) is prepared and samples are collocated into it for 3 different times: 24 hours, 3 days and 7 days.

Finally, SEM analysis is performed to visually check interaction between samples and SBF. This is useful to evaluate the material's bioactivity and therefore its effectiveness for use in bone tissue regeneration.

The change in surface morphology of the sample due to the formation of crystalline hydroxyapatite is a sign of the occurred interaction. In fact, it shows the ability of creating a bond with bones.

First step is to prepare the SBF which is prepared following a protocol that can be easily found in literature [70].

The first requirement is to have in the SBF the same ionic concentrations of plasma species. In order to achieve this, several precursors are mixed together following a rigid order. So it is needed : sodium chloride (NaCl 99,5%, *Sigma*), sodium bicarbonate (NaHCO<sub>3</sub>, *Merck*), potassium chloride (KCl, *Panreac*), sodium hydrogen dyphosphate (Na<sub>2</sub>HPO<sub>4</sub>, *Panreac*), cloreto de magnesium chloride exahydrate (MgCl<sub>2</sub>·6H<sub>2</sub>O, *ROTH*), hydrochloric acid 37% (V/V) (HCl, *Carlo Erba*), calcium chloride dihydrate (CaCl<sub>2</sub>·2H<sub>2</sub>O, *Honeywell | Fluka*), sodium sulfate (Na<sub>2</sub>SO<sub>4</sub>, *Fluka*), tris(hydroxymetil)aminomethane (C<sub>4</sub>H<sub>11</sub>NO<sub>3</sub>, *Alpha Aesar*).

All the precursors were added to ultrapure water.

For this purpose, first step is to prepare 700 ml of ultrapure water and putting it on magnetic agitation, connected to pH and temperature meters.

Meters must be connected and on service during the all process, being these two parameters essential for the success of the preparation.

Magnetic stirrer should be placed to a speed of 100-300 rpm, taking care of varying it according to how dense is the solution.

Precursors are listed in table 2.4 in the order that must be followed to add them to the solution.

**Table 2.4** Ingredients listed in the order to follow to add them.

	List of ingredients	Quantity
1	NaCl	9,8184 g
2	NaHCO <sub>3</sub>	3,4023 g
3	KCl	0,1118 g
4	Na <sub>2</sub> HPO <sub>4</sub>	0,2129 g
5	MgCl <sub>2</sub> ·6H <sub>2</sub> O	0,4574 g
6	HCl	3 ml
7	CaCl <sub>2</sub> ·2H <sub>2</sub> O	0,5822 g
8	Na <sub>2</sub> SO <sub>4</sub>	0,1080 g
9	C <sub>4</sub> H <sub>11</sub> NO <sub>3</sub>	1,8189 g

After that all the ingredients are added following the list and leaving more about 5 minutes between each other, to let the solution to stabilise.

One critical step is the addition of 1M hydrochloric acid. It should be added dropwise, lowering the pH solution until a value of 7.4. Then, pH should be controlled and held at this level from this step on the process. If it is higher, it is just necessary to add more HCl. If it is lower, a solution of ammonia should be created.

When all the ingredients have been added, it is necessary to wait a couple of hours for the solution to be stable and transparent. Finally, Millipore water must be added until reaching the total volume of 1 L of solution.

It is necessary to store it in the fridge to conserve it.

Samples for bioactivity tests must be prepared in the specific shape of a disc to have a wide surface area and consequently increasing chemical susceptibility.

To pursue the preparation process, it is necessary to measure the quantity of 300 mg of powder for each sample. After that, each sample singularly is mixed with PVA added as a binder. It is then put into the press (*Specac* ©), set with the weight of 5 tons, which is maintained on the sample for 5 minutes to consolidate into the shape of the disk.

In this way, samples are formed with diameter of 13 mm and 2.5 mm thickness.

They are then sintering at the temperature of 800°C for 1 hour, heating up from room temperature and persisting at the sintering temperature for 1 hour.

Samples are then immersed in SBF for 24 hours, 3 days and 7 days.

When removed from SBF, samples are washed with Millipore water and dried at room temperature.

Finally, surface morphology is analysed with SEM, looking for any evidence of bioactivity, at the listed above time.

### 2.2.8 *Citotoxicity test*

Another fundamental during development of a biomaterial is a citotoxicity test.

Cell death can derive from different episodes. It can be due to necrosis, in which they lose cellular membrane and die rapidly due to cell lysis. Other ways are if cells lose integrity and stop growing and dividing or if cells activate genetic program of controlled death (apoptosis).

In order to understand cell viability of samples the test is perform checking their toxicity when in contact with Vero cells. They are a lineage of cells used in cell cultures. It was first isolated from kidney epithelial cells from an African green macaque.

Cells lineage are prepared in vitro and they last until they grow enough to totally cover the space in which they are or until they finish nourishment [55]. Cells viability is evaluate using resazurin, which is a blue not fluorescent dye that can be used also as a pH indicator. Resazurin has the advantage of being almost not citotoxic.

Resazurin is turned into a pink fluorescent compound called resorufin by viable cells, as showed in fig. 2.5.

Thanks to this chemical reaction is possible to understand how many viable cells remain in the medium. This is possible checking the absorbance at 2 different wavelengths related to resazurin and resofurin.

In fig 2.6 is possible to see the absorbance spectrum and to compare the intensity of the two peaks in order to evaluate cells viability.

Before proceeding with the test, it is recommendable to perform a pH test to powders. In fact, if the detected pH is too basic or too acid, cells will die for this reason and not for materials being toxic by itself. If pH detected is higher than 7.5-8 dialysis is performed to reduce it to a normal level.

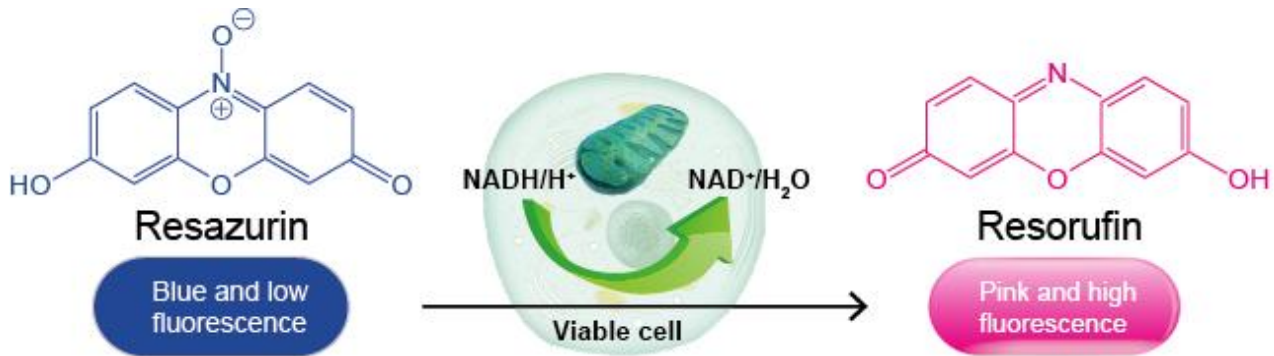


Fig. 2.5 Transformation of Resazurin into Resorufin due to interaction with viable cells [57].

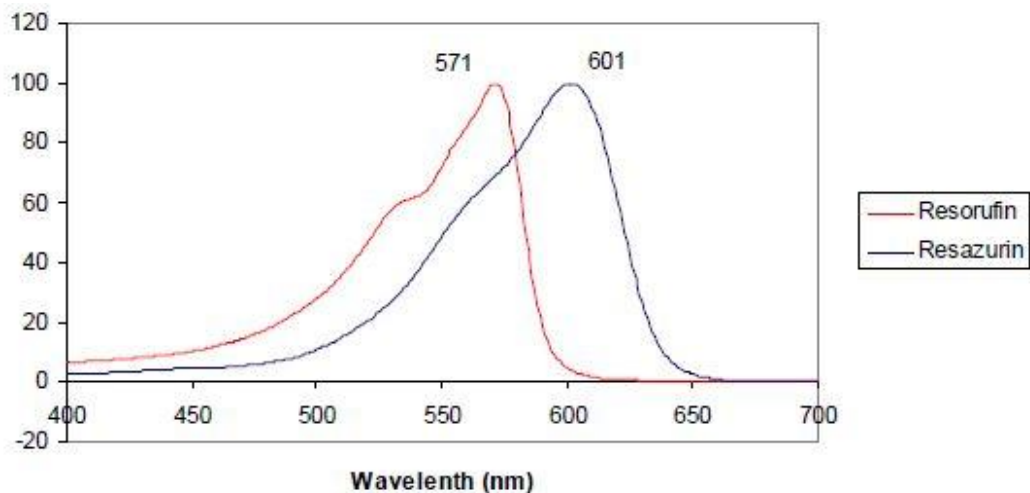


Fig. 2.6 Resazurin and resorufin absorbance curves. Their respective peaks is at different wavelength [57].

After this is done, it is now possible to proceed with the cytotoxicity evaluation itself.

First step is to prepare 200 mg of each sample and to put them in separate flasks. After that it is essential to put all of them in the oven at  $120^{\circ}\text{C}$  for 4 hours, in order to kill all bacteria and fungi, sterilizing the powders and eliminating any kind of contamination.

Contamination must be absolutely avoid all along the entire test. For this reason, all the processes are performed into a cell culture hood. On addition to that, alcohol 70% is sprayed several times, before, during and after every passages developed inside the hood.

Indeed eventual contamination can completely falsify results.

All the processes must be performed wearing gloves, hair-net and lab coat.

Culture medium should then be placed inside the hood for 2 hours before being used for the tests.

Culture medium in this case is DMEM which is a modified version of MEM. MEM is the primary culture, while DMEM is obtained modifying MEM increasing level of amino acids and vitamins [55].

It is now possible to add  $1800\ \mu\text{l}$  DMEM (without serum, that will be add later) to each flask and then put them in the oven for 2 days at  $37^{\circ}\text{C}$ .

After that it is possible to start preparing cell culture. Cells are then moved inside the 96 small wells in which cytotoxicity of materials will be evaluate. Culture medium is removed and the cell layers

remaining is then wash with PBS (phosphate buffer solution) without calcium and magnesium, with a volume of liquid equal to one of cultural medium.

To move cells from the culture plate to the 96 wells is necessary to unstick cells from the bottom of the plate. This is pursued using 0,5 ml of trypsin, which destroy bonds between cells and substrate, every 25 cm<sup>2</sup>. Using a microscope the plate should be analysed to make sure all the cells are detached and floating. After re-suspension is done by using a fresh medium with serum to inactivate the trypsin.

Next step is to count the number of cells , to be able to determine viable cell concentration. For this purpose 100-200 µl of cell suspension is removed adding also trypan blue in the same quantity (dilution factor = 2). Heamocytometer is then prepared by moisturing the coverslip and then placing it over the chamber using slight pressure. When Newton's refraction rings (they are rainbow – like rings under the coverslip) start appearing.

Moreover 5 – 10 µl are used to fill both sides of the chamber which is then viewed under an inverted microscope using 20x magnificent.

In order to calculate cellular concentration number of viable cells inside squares of a set dimension. It usually good to count at least 100 cells. Trypan blue makes viable cells appeared bright while dead cells are stained blue.

Cell concentration can be calculated using the equation 2.4 below.

$$\text{Viable cells (live cells per millimeter)} = \frac{\text{Number live cells counted}}{\text{number of large squares counted}} \times (\text{dilution factor}) \times 10000 \quad \text{Equation 2.4}$$

With equation 2.4 a cell concentration in the suspension of 1265 kcells/ml. It is then diluted 892 µl of suspension into DMEM in order to reach the final volume of 18800µl, in order to prepare the solution to be placed inside the 96 wells. In order to obtain a cocentration of 20 kcells/cm<sup>2</sup>, it is placed 100 µl in each well, characterised by the surface area of 0,3 cm<sup>2</sup>.

Sewed wells prepared are then placed in the oven at the temperature of 37°C in control of CO<sub>2</sub> and humidity.

In fig. 2.7 a picture of a well with the cell suspension is displayed.

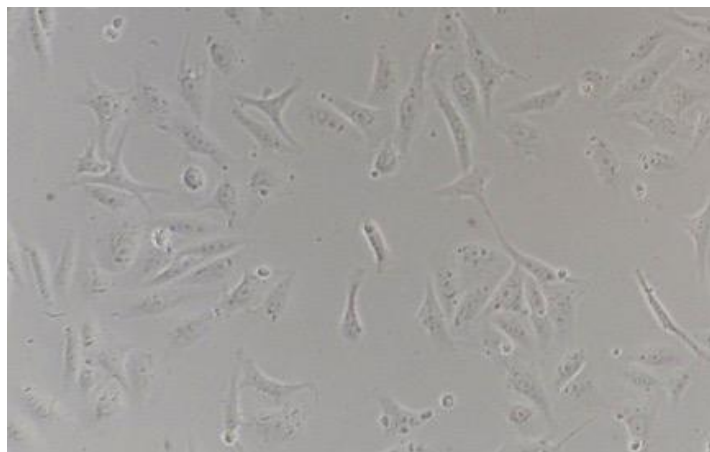


Fig. 2.7 Well with the cells suspension.

Next step is to take out from the fridge samples prepared and extract 900 µl of suspension from every flask. To this quantity is then added 100 µl of FBS (foetal bovin serum), which is a complex mix of albumins, growth factors and growth inhibitors.

The suspension prepared this way is referred as the suspension C0 and 100 µl of it are put in each of the five well with cells sewed the day before. The remaining 500 µl are then diluted with 500 µl of

DMEM, resulting in the suspension C0/2, in which powder concentration is half the C0. 100µl are then put in other 5 wells with cells inside.

Finally, the remaining 500 µl is diluted again with µl of 500 DMEM, creating C0/4, whose concentration is one quarter of the first C0. 100 µl are then placed in other 5 wells with cells.

This procedure is repeated for each of the six prepared samples.

As can be easily understood, passing C0 to C0/4 the amount of materials gradually reduces, determining a less aggressive solution. Increasing concentration may determine increasing toxicity.

After that a solution of resazurin 0,04 mg/ml in PBS<sup>+</sup> (this PBS contains calcium and magnesium as well) to measure cell viability with resazurin technique explained before. A second solution is prepared in the proportion of 50% of the solution first one and 50% of DMEM. Medium is then removed from every wells and substitute by 100 µl of the new solution. Cells are then incubated for 3 hours at 37°C in controlled atmosphere of CO<sub>2</sub> and humidity.

6 wells are prepared to be control of medium, positive control and negative control and they are maintained in the same conditions of other wells throughout the process but without the addition of iron-doped hydroxyapatite powders.

In fig. 2.7 the aspect of the 96 wells before putting them into the machine to measure absorbance is showed.

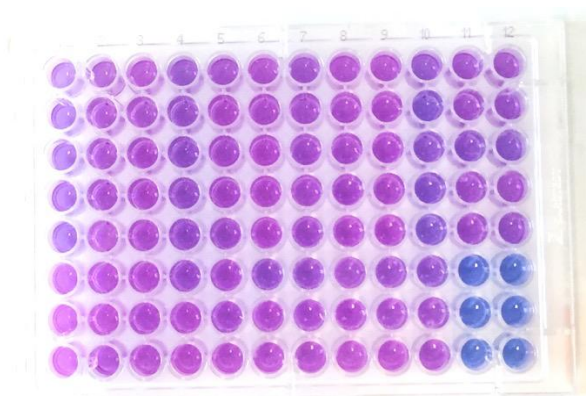


Fig. 2.7 Aspect of the 96 wells with cells before measuring absorbance.

The plate is then put inside the machine and absorbance is measured at 571 and 601 nm, corresponding to the two peaks of resazurin and resorufin, to be able to determine powders viability.

In fig. 2.8 are shown details of some wells identified by a letter and a number, where the letter is the line and the number the column, imagining the 96 wells-complex as organised in a grid.

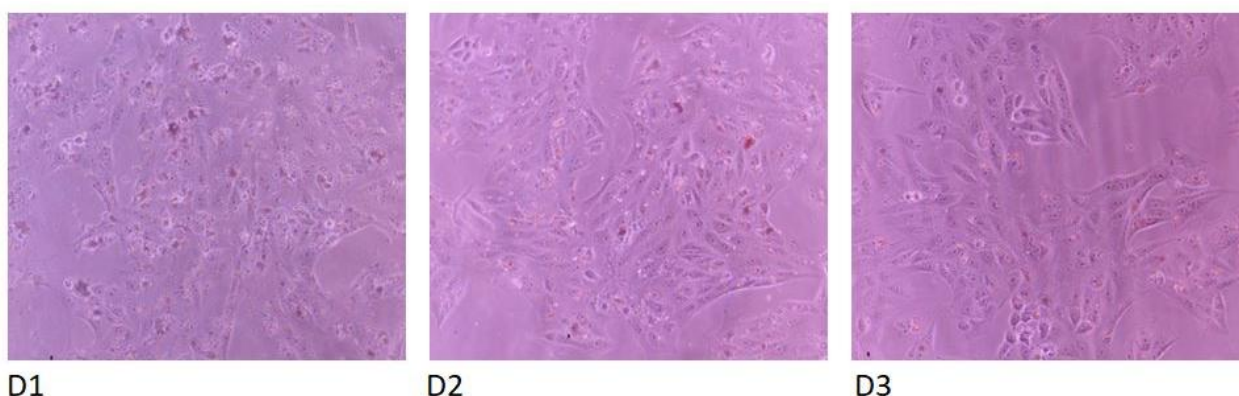


Fig. 2.8 Details of three wells with resazurin solution.



### 3. Results and discussion

In this chapter, all the results related to each analysis will be deeply discussed.

First of all, a visual characterisation can be done just looking at the aspect of powders produced, at different temperature and with different chemical composition.

#### 3.1 Visual characterisation

First check that can be performed on a new synthesized material is visual check. One can make a hint of the composition of the powders just by looking at their colour. This because some oxides and compounds have an identifying colour, such as iron oxide powder that is usually red. In fig. 3.1 obtained powders are presented.

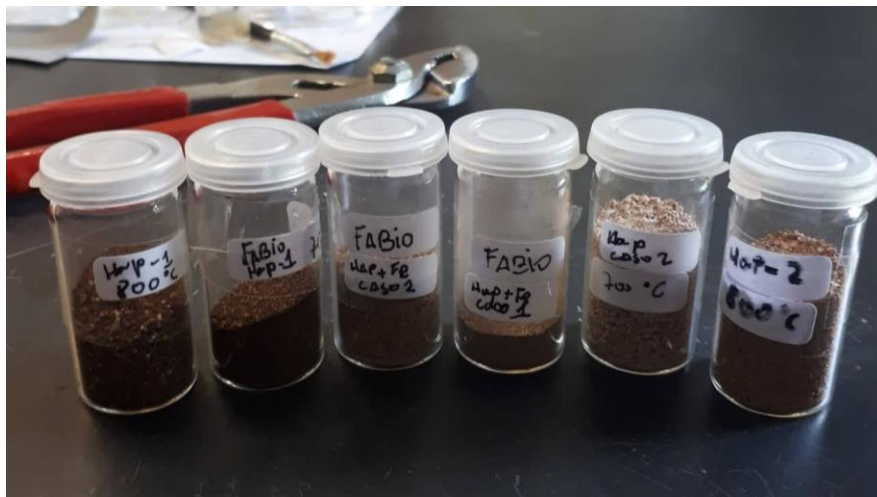


**Fig. 3.1** All six synthesized powders (“HAp + Fe caso 1” and “HAp + Fe caso 2” are respectively sample 1 – 600°C and sample 2 – 600°C).

By increasing the sinthering temperature, considering the same composition, powders get a colour more and more approximated to dark red, suggesting the possibility that increasing temperature iron oxide more easily segregates.

No clear differences can be recognised between two different compositions when comparing two samples synthesized at same temperature.

#### 3.2 X-Ray analysis (XRD)

The diffractogram of a crystal is very useful not only to intimately identify it but also to clarify some aspects about its structure.

In this way, several level of study can be performed using a diffractogram.

Firstly sample 1 synthesized at 600 °C is compared to a regular diffractogram of a common hydroxyapatite.

Fig. 3.2 shows XRD spectrum of sample 1 – 600 °C displaying all peaks related to hydroxyapatite with the respective crystallographic plane direction.

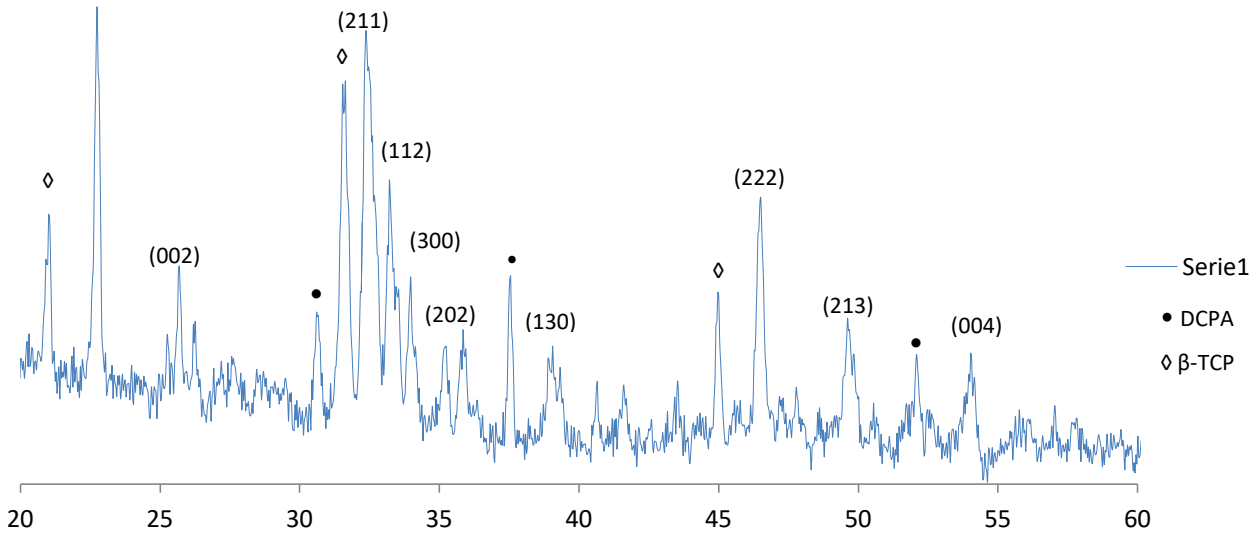


Fig. 3.2 Diffractogram of sample 1 – 600°C.

Diffractogram is quite different if compared to the usual not doped hydroxyapatite taken in the literature (fig 3.3) with a Ca/P ratio of 1,67. This is probably due to the different ratio between positive ions and negative ions in this hydroxyapatite. In fact, in the case of sample 1 ( $\text{Ca}^{2+} + \text{Fe}^{2+} + \text{Fe}^{3+}$ )/P is around 1,80, resulting in the presence of other compounds in hydroxyapatite. Comparing to similar experience found in literature, in which the ratio is around 1,80, formation of secondary calcium phosphate is evidenced [76]. As represented in fig. 3.2 peaks of anhydrous calcium phosphate (DCPA) and  $\beta$ -tricalcium phosphate ( $\beta$ -TCP) can be found, showing the presence of this compound in the material.

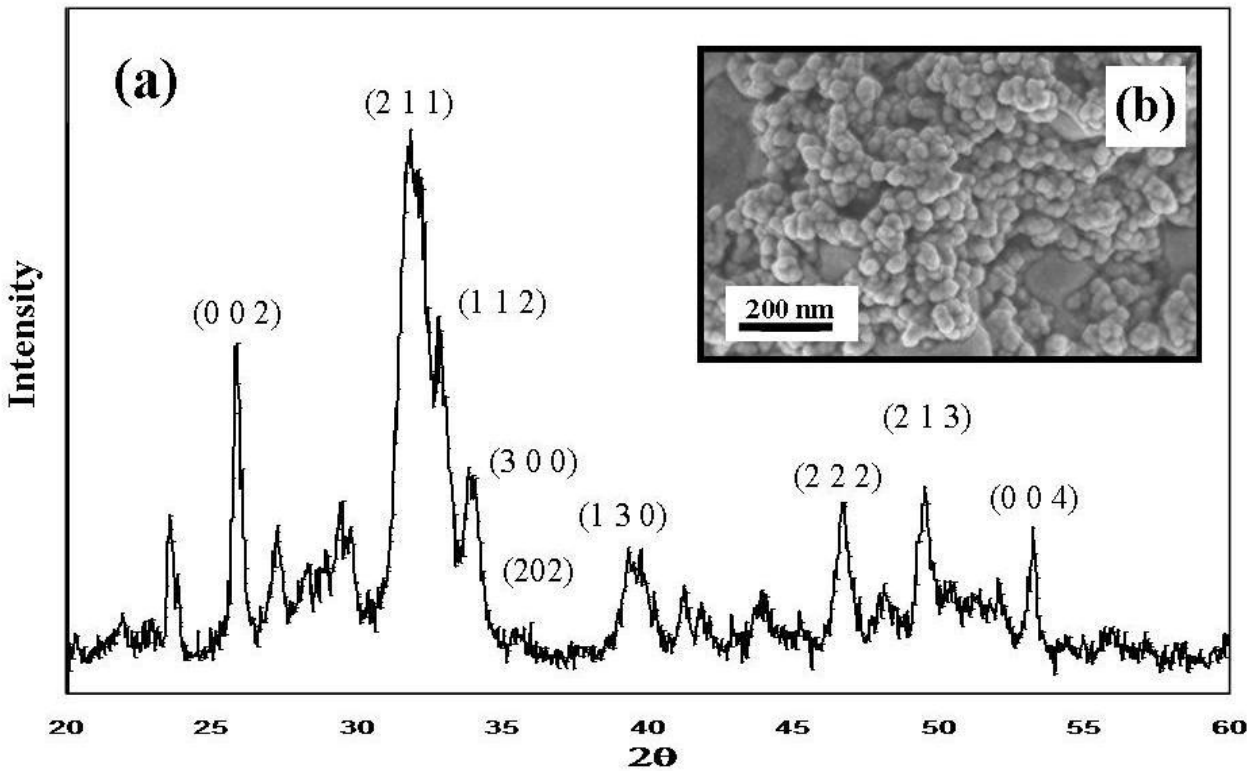


Fig. 3.3 Un-doped hydroxyapatite nanoparticles diffractogram, used for comparison [58].

Furthermore, the high intensity peak at around  $22^\circ$  can be related to hydroxyapatite or to  $\beta$ -tricalcium phosphate[60]. The intensity higher than usual can be due to the fact of the presence of both compounds.

Peaks ascribed to  $\beta$ -TCP are identified with the symbol “ $\diamond$ ” in fig. 3.2.  $\beta$ -TCP usually derives from the thermal decomposition of hydroxyapatite or from a Ca/P ratio above 1,67 as can be seen in similar situations found in literature[60]. Probably in this case, presence of  $\beta$ -TCP depends on both reasons.

In fact, the presence of other compounds can be supposed as well, like compounds containing chlorine, calcium carbonate or calcium hydroxide. Even though there are no clear evidences for them from the XRD, FTIR could probably be useful to detect them, by looking for peaks whom intensity depends on the presence of these compounds.

Considering sample 2 –  $600^\circ\text{C}$  it is easy to recognize a common diffractogram of hydroxyapatite, with a normal ratio of 1,67. In fact, as can be seen in fig. 3.4 all hydroxyapatite peaks can be identified, showing that doping with this quantity of iron doesn't seem to affect the crystalline structure, at least when sintered at this temperature.

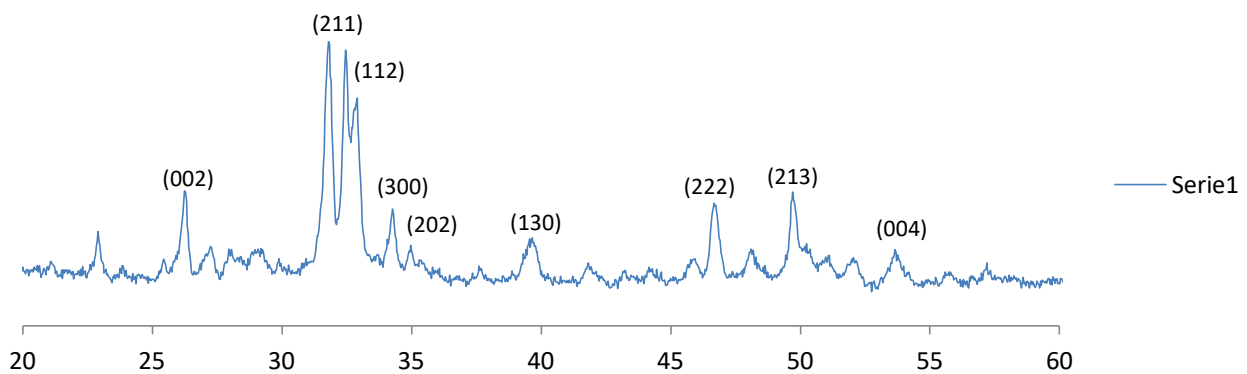


Fig. 3.4 Sample 2 –  $600^\circ\text{C}$  iron doped hydroxyapatite diffractogram.

As a comparison between the two diffractograms related to sample 1 and sample 2 both sintered at  $600^\circ\text{C}$ , different in structure can be ascribed to difference in the content of iron doping and in the different ratio  $(\text{Ca}^{2+} + \text{Fe}^{2+} + \text{Fe}^{3+})/\text{P}$ .

It can be supposed that increasing the content of iron could lead to a higher formation of secondary phase such as  $\beta$ -TCP, other phosphate and calcium oxide.

More information will be deductible after having calculated crystallite diameters, percentage of crystallinity and cell lattice parameters.

It is interesting to compare between each other diffractograms related to the same composition for hydroxyapatite just sintered at difference temperature, to understand if the temperature can have an influence in the final structure formed. In fig. 3.5 all the sample with composition 1 are displayed.

As can be seen there aren't big differences between the 3 diffractograms: same peaks in the same position, just the intensity of some of them is different. Specifically, the peak at  $22^\circ$  is higher in sample 1 –  $600^\circ\text{C}$ .

The peak at  $37^\circ$  deserves a special mention. In fact, it is just displayed in the sample prepared at  $600^\circ\text{C}$  and disappeared in all the other. *Ramesh et al.* [59] associates this peak to the presence of CaO inside the powders.

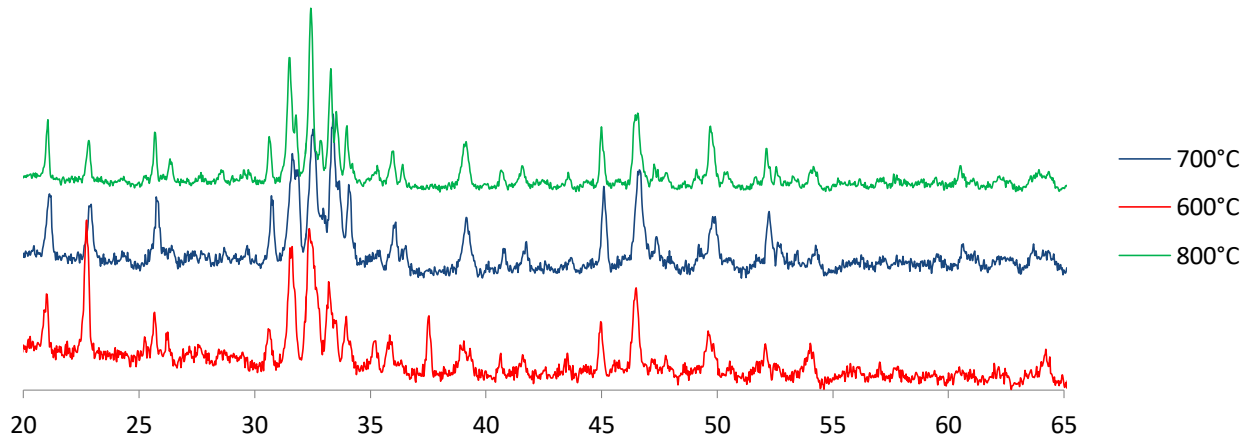


Fig. 3.5 Diffractogram of 3 samples with composition 1, sintered at different temperatures.

Same comparison can be performed when considering sample 2 and the 3 different sintering temperature. The result is displayed in fig. 3.6.

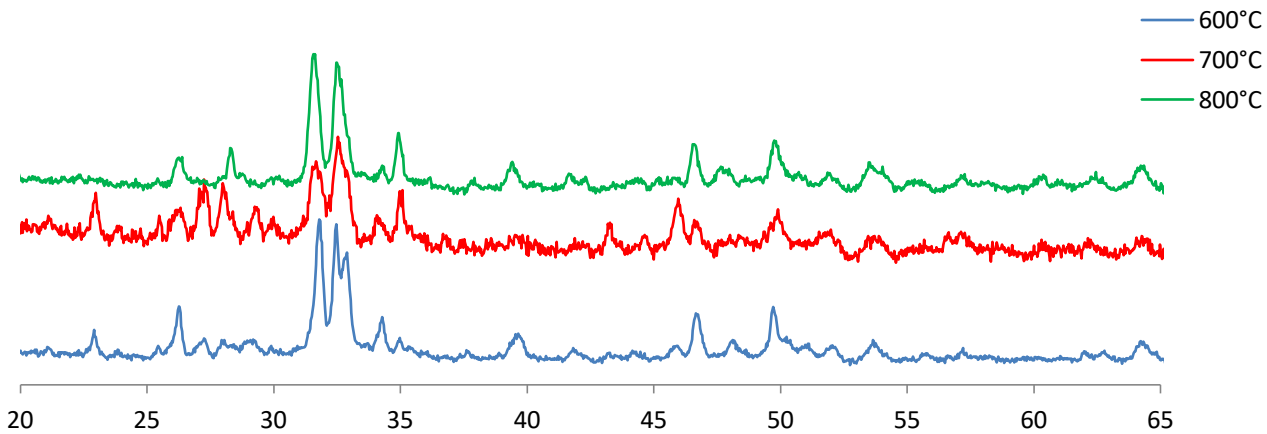


Fig. 3.6 Diffractogram of 3 samples with composition 2, sintered at different temperatures.

Two main differences can be detected between the sample at 600°C and both the other in increasing the temperature, the peak corresponding to the crystallographic plane (202) gets bigger and bigger, which means that in changing temperature this plane grows more. In the same time, a new peak starts appearing at the degree of 28,5°. According to literature, it can be the sign of the presence of hematite inside the powders, this being a typical hematite resonance peak. This would also explain the change in colour of the powder, which gets more red when sintered at higher temperature.

Sample 2 – 700°C deserves a deeper focus. In fact, it presents in the range 25°-30° several peaks which are not detected in the other samples. *Lee et al.* [60] identify these peaks as being typical of  $\beta$ -TCP, which means that supposedly sample 2-700°C synthesis condition lead to the formation of tricalcium phosphate and/or other phosphate rather than hydroxyapatite. This might explain differences that can be seen between its spectrum and the other 2.

Performing the sintering process in nitrogen atmosphere can be a good solution in order to avoid the formation of hematite, which reduces the amount of iron that could substitute  $\text{Ca}^{2+}$  in hydroxyapatite structure.

From the diffractograms it is possible to extrapolate also information about crystallinity, crystallite diameter and cell parameter of the analysed powders.

Now each of this characteristic related to all the 6 samples will be discussed.

### 3.2.1 Crystallinity

Crystallinity can be calculated using equation 3.1 displayed below.

$$X_c = 1 - \frac{V_{112/300}}{I_{300}} \quad \text{Equation 3.1}$$

Where  $I_{300}$  is the intensity of the diffraction peak (300) and  $V_{112/300}$  is the valley between the peak (112) and (300) of HAp.

Results are collected in table 3.1.

**Table 3.1** Crystallinity of all the 6 samples.

Sintering temperature	600°C	700°C	800°C
$X_c$ (Sample 1)	38,8%	36,9%	47,9%
$X_c$ (Sample 2)	38,6%	21,5%	14,9%

For what concerns sample 2, when the sintering temperature increases, crystallinity is getting smaller and smaller, this due to the probable formation of other compounds as it has been showed before when analysing the XRD spectrum.

This being in contrast with what *Fathi et al.* [62] found out in their analysis, where percentage of cristallinity increased while increasing sintering temperature. However, *Fathi et al.* [62] considered un-doped hydroxyapatite. It means that possibly the addition of iron could influence cristallinity, reducing it when increasing the sintering temperature.

While this being true for sample 2 as can be seen for fig. 3.7, it is not the same for sample 1. In fact, in this case crystallinity displays an oscillating behaviour with the increase of temperature. This might derive from the formation of more  $\beta$ -TCP and the improvement in crystalline organisation due to more energy deriving from thermal treatment.

Finally, no general trend can be observed.

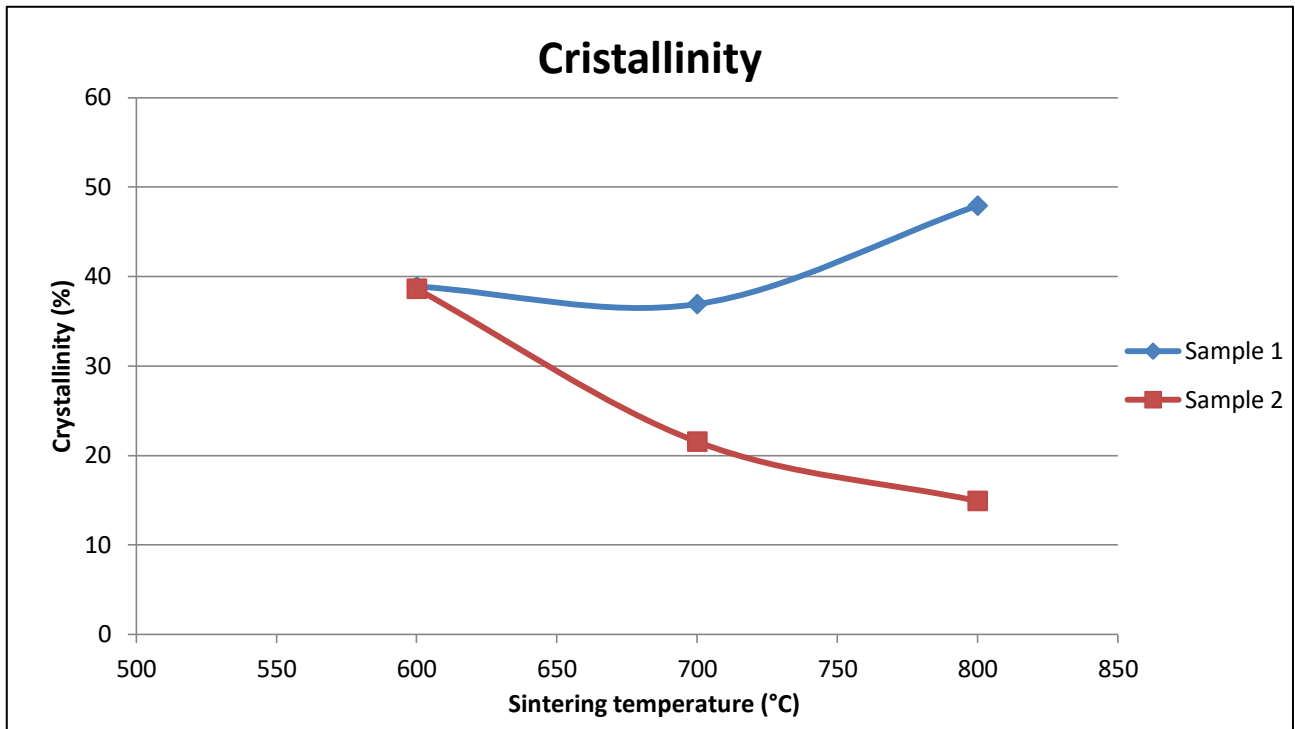


Fig. 3.7 Crystallinity vs sintering temperature for analysed hydroxyapatite powders.

### 3.2.2 Crystallite diameter

Using equation 2.1 is possible to calculate the diameter of crystallite of the synthesized powders. For each sample a different peak for the calculation is considered, every time the highest is chosen. In the table 3.2 is displayed the crystallite diameter, which shows the dimension of a continue crystalline dominion inside the material. Indeed, it is the dominion dimension in which a powder particle diffracts x-rays coherently.

Table 3.2 Crystallite diameter of sample 1 and 2 at different sintering temperature.

Sintering temperature	600°C	700°C	800°C
Sample 1	35	14	31
Sample 2	22	8	14

According to *Trinkunaite-Felsen et al.* [63] a reduction of crystallite diameter should occur if compared to the un-doped hydroxyapatite, because  $Fe^{2+}$  and  $Fe^{3+}$  ions with a smaller radius (0,77Å and 0,63 Å) substitute  $Ca^{2+}$  with a bigger radius (0,99 Å). This reduction in radius reduce the dimension of crystalline dominion.

According to *Fathi et al.* [62] higher diameter should be obtained at higher sintering temperature. This is not happening linearly in both sample 1 and 2. In fact in both case increasing the sintering temperature doesn't imply a linear increase in crystallite diameter.

What is interesting to underline, is that comparing sample 1 and 2 at the same sintering temperature, crystallite diameter of sample 1 is always higher than the diameter of the other one. Which follows the same trend of crystallinity, that it always bigger in case of sample 1 when compared to sample 2.

As a general conclusion probably the higher  $(Ca^{2+} + Fe^{2+} + Fe^{3+})/P$  ratio leads to a better crystallinity and crystallite diameter. This makes sense, because higher crystallinity means also less solubility which gets lower when increasing that ratio.

Finally, as general conclusions cannot be drawn for what concern the change in sintering temperature, the change in iron and the ratio lead to a different crystallinity in iron doped hydroxyapatite.

In fig. 3.8 is shown how crystallite diameter vary in changing sintering temperature for both samples.

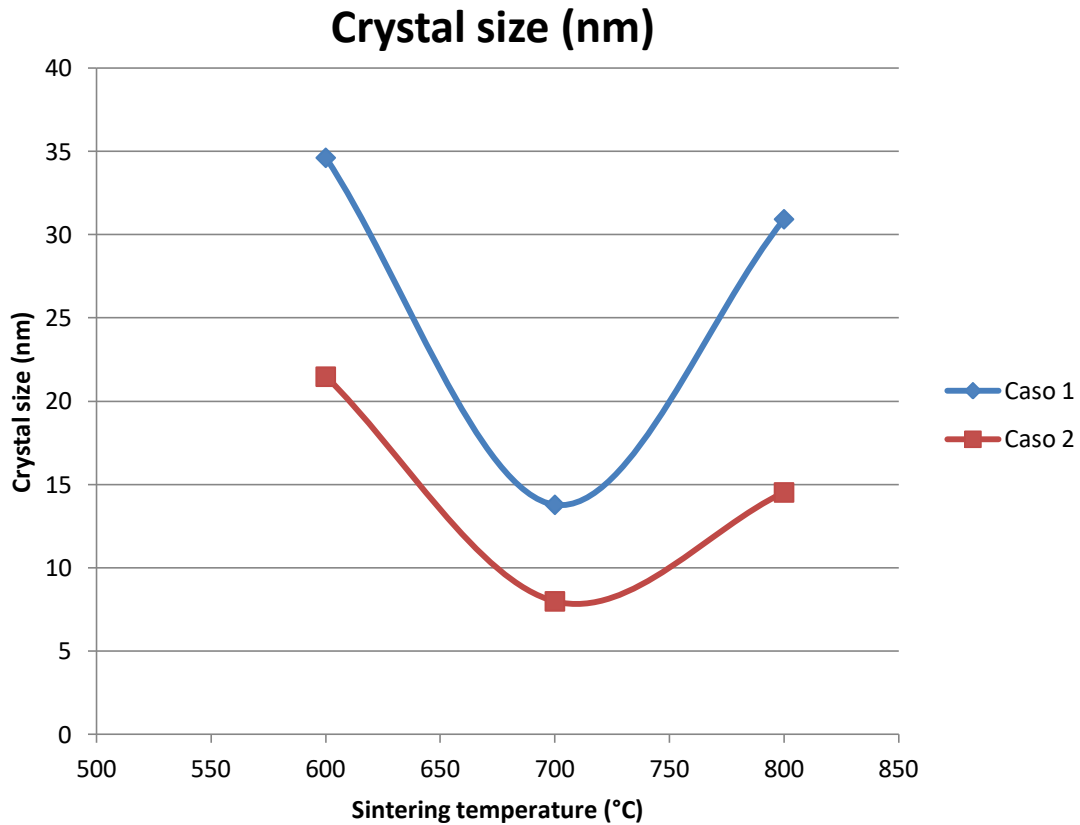


Fig. 3.8 Crystal size vs sintering temperature for both samples.

### 3.2.3 Cell parameters

Cell parameters of the hexagonal hydroxyapatite cell can be calculated adopting the two equations 2.2 and 2.3, choosing every time a diffraction peak which allows to obtain the value  $a$  ( $a = b$ ) and  $c$  of the lattice cell.

All the results are displayed in table 3.3 and table 3.4 below.

Table 3.3 Cell parameter  $a$  of both samples 1 and 2 at 3 sintering temperature.

Sintering temperature	600°C	700°C	800°C
Sample 1	1.83 nm	1.82 nm	1.83 nm
Sample 2	1.81nm	1.82 nm	1.81 nm

**Table 3.4** Cell parameter *c* of both samples 1 and 2 at all 3 sintering temperature.

Sintering temperature	600°C	700°C	800°C
Sample 1	1.39 nm	1.38 nm	1.38 nm
Sample 2	1.36 nm	1.35 nm	1.36 nm

At a first sight at table 3.3 and table 3.4 it is clear how small is the variation of both parameters *a* and *c* in changing sintering temperature, this statement being valid for both samples. Specifically, there is no correlation between the increasing in sintering temperature and both parameters *a* and *c*. In fact, as can be seen in figure 3.9, they vary in an oscillating way.

More interesting the comparison between the two hydroxyapatites with different iron content. In fact, firstly sample 1 always shows higher cell parameters when compared to sample 2, this being valid comparing the two samples at any sintering temperature.

In literature several studies about cell parameters change in doped hydroxyapatite can be found. Usually a change in lattice dimensions is related to difference in radius between the doping ion and  $\text{Ca}^{2+}$ .

*Trinkunaite-Felsen et al.* [63] investigated cell parameters in iron doped hydroxyapatite, concluding that they are lower in case of iron substitution due to the dimension of Fe ions which is lower than  $\text{Ca}^{2+}$  ions.

Moreover, *Kyriacou et al* [66] found out that cell parameters are lower when hydroxyapatite is doped with iron.

Authors also found out that *a* and *c* are lower in case of doped samples if compared to normal hydroxyapatite. Specifically, this increase can be ascribed to the geometric position of iron ions inside the hydroxyapatite structure. In fact Fe ions substituting Ca in the position Ca(1) can decrease the bond length perpendicular to *c* axe, consequently decreasing *a* axe [66].

*Low et al.* [65] also found out the same decrease in *a* axe.

On the other hand, *Kaygili et al.* [64] described a small increase in *a* and *c* axes for hydroxyapatite sintered at 800°C and more.

*Gomes et al.* [49] evidenced an interstitial insertion of Fe inside hydroxyapatite structure which determines a sharp expansion of *c* axe and the combined contraction of *a* axe, similar to what happens for Zn doping. The lattice variation also depends on Fe ions concentration. Finally the authors discovered that this huge lattice parameters variation takes place when powders are sintered in the range of temperature between 1000 and 1100°C.

In fig. 3.9 *a* lattice parameter is displayed for both samples at the 3 different sintering temperature.

As can be seen, even though differences are not so big in value, it is showed how sample 1 with a higher amount of iron lattice parameter is bigger than that of sample 2, for any value of sintering temperature. The same happens for *c* parameter as can be seen from fig. 3.10.

In both case, lattice parameters vary in an oscillating way when it is varied sintering temperature.

It is important to predict how doping influences crystalline structure, because this reflects on the final properties of the material that is synthesized.

It is interesting now to evaluate the phase percentage between hydroxyapatite and  $\beta$ -TCP in a bifasic composition like all the 3 cases of sample 1, in which the presence of  $\beta$ -TCP is evidenced by the XRD graphic.

In next paragraph it will be calculated.

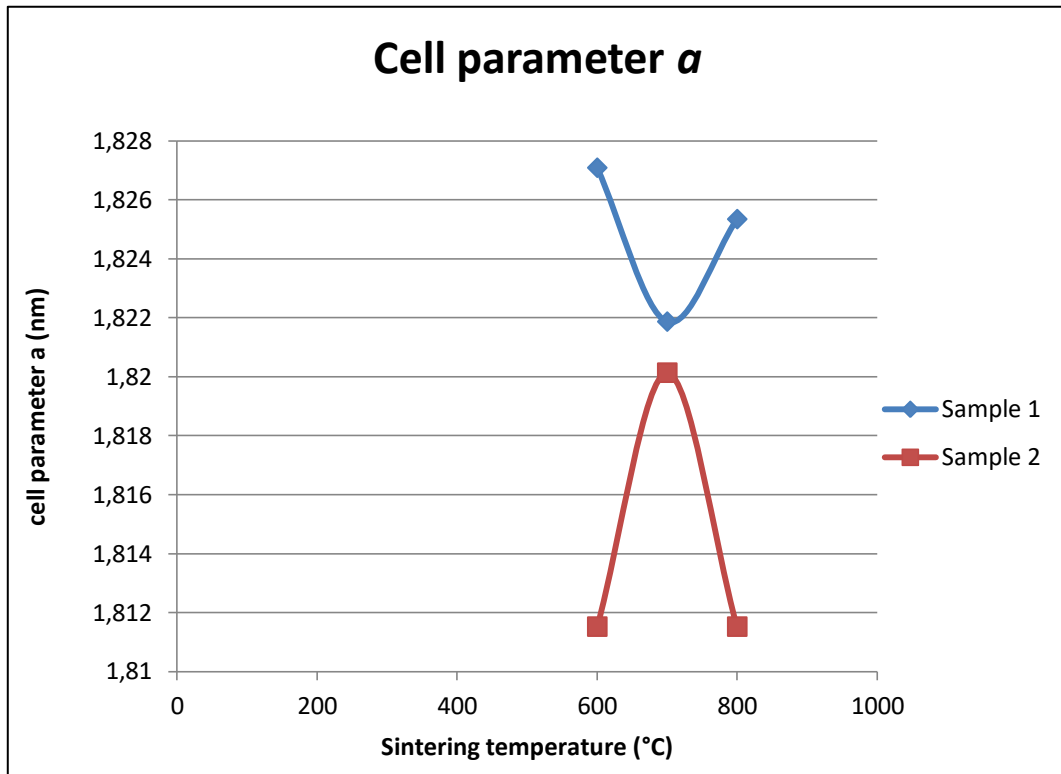


Fig. 3.9 Cell parameter  $a$  for all the six samples prepared.

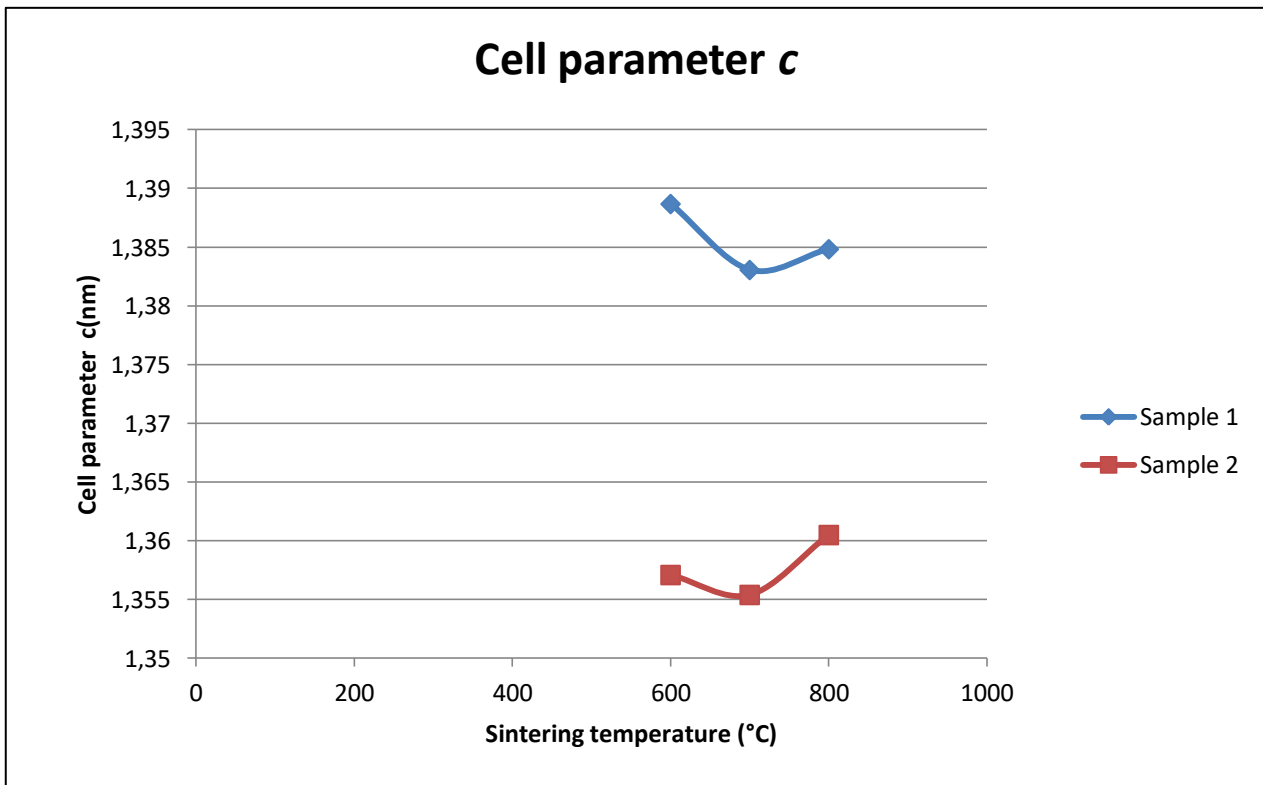


Fig. 3.10 Cell parameter  $c$  for all the six samples prepared.

### 3.2.4 Phase percentage HAp/ $\beta$ -TCP

In literature can be found examples of how calculate ratio between HAp and  $\beta$ -TCP in a material composed of both calcium phosphate components. Therefore, for some applications it is required to develop a certain ratio, so Equation 3.2 can be used to calculate it.

$$\text{HAp(\%)} = 100 * \frac{I_{211\text{of HAp}}}{I_{211\text{of HAp}} + I_{210\text{of } \beta\text{-TCP}}} \quad \text{Equation 3.2}$$

Using equation 3.3 it is possible to calculate all values of phase percentage HAp/ $\beta$ -TCP at three different sintering temperature for sample 1, the one in which traces of tricalcium phosphate were found.

As can be seen from fig. 3.11 where values obtained are plotted against sintering temperature, increasing in temperature is followed by a slow increase in hydroxyapatite percentage inside the sample.

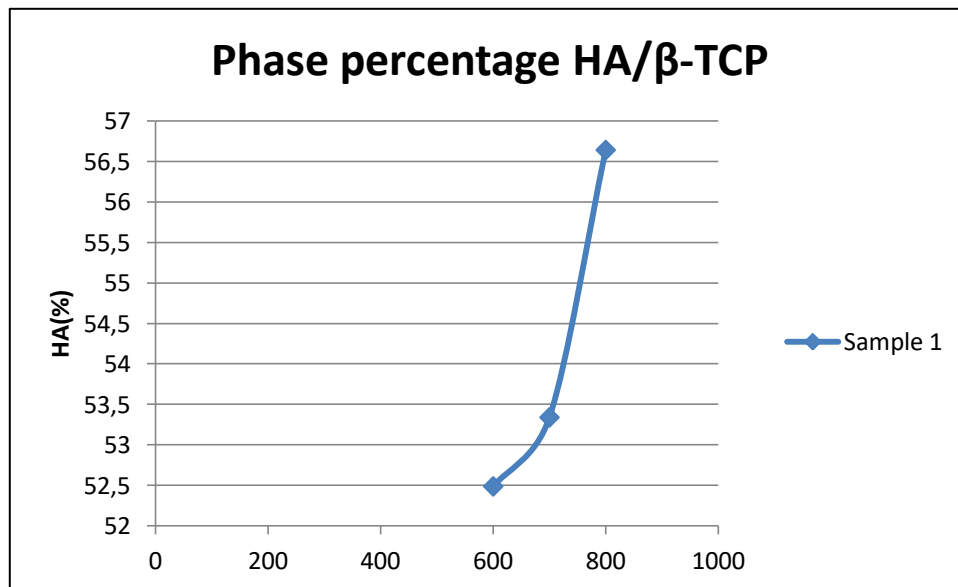


Fig. 3.11 Hydroxyapatite percentage plotted against sintering temperature for sample with composition 1.

Passing now to FTIR analysis, it is possible to get more information about compounds making up the powders.

### 3.3 FTIR analysis

FTIR analysis is performed looking for HAp functional groups, as well as other group belonging to other possible compounds that could be identified as a part of powders. FTIR is a good instrument to confirm the presence of compounds whose presence has been supposed before through XRD.

Moreover, FTIR is carried out on sample 1 and 2, considering all 3 different sintering temperature. Firstly, sample 1-600°C is analysed, trying to identify the most important peaks and the functional group they refer to.

As can be seen in fig. 3.12 all the peak of sample 1 - 600°C are analysed and labelled.

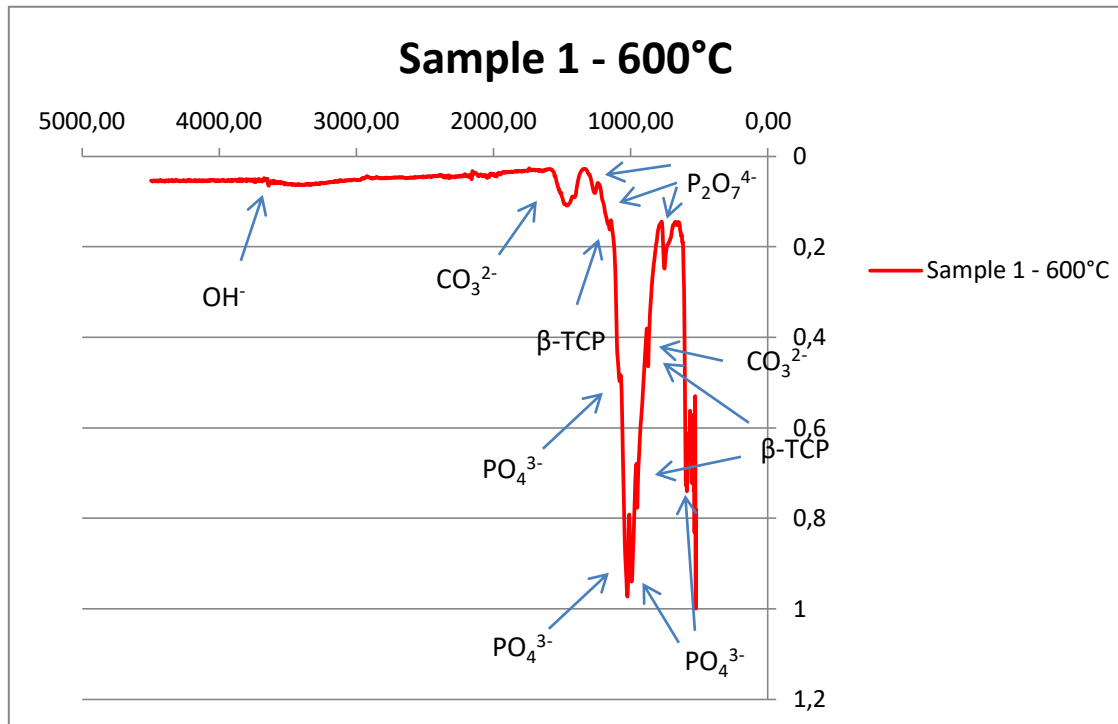


Fig. 3.12 FTIR of sample 1-600°C: all the important peaks are labelled showing the functional group they refer to.

Analysing fig. 3.12 all hydroxyapatite peaks are visible. Double peaks at  $1090\text{ cm}^{-1}$  and  $1040\text{ cm}^{-1}$ , as well as the shoulder at  $960\text{ cm}^{-1}$  are respectively the asymmetric and symmetric stretching of  $\text{PO}_4^{3-}$  ions. The peak at  $600\text{ cm}^{-1}$  is also due to  $\text{PO}_4^{3-}$ . At  $3600\text{ cm}^{-1}$  a short peak refers to  $\text{OH}^-$  vibration. It is not very intense and it is not easily detectable the other one at around  $600\text{ cm}^{-1}$ . This might be due to the presence of ions  $\text{CO}_3^{2-}$ , which could substitute  $\text{OH}^-$  or phosphate ions in hydroxyapatite lattice. In the band between  $1400\text{ cm}^{-1}$  and  $1500\text{ cm}^{-1}$  it is evidenced the presence of carbonate ions vibration, which is also visible at  $873\text{ cm}^{-1}$ .

This two are assigned to stretching and bending of  $\text{CO}_3^{2-}$ [68]. The peak at  $873\text{ cm}^{-1}$  can also be ascribed to  $\beta$ -TCP whose existence is proved also through the XRD spectrum. Probably this is further confirmation for the formation of tricalcium phosphate inside the material[67].

Other peaks deserve mention and are those at  $1200\text{ cm}^{-1}$ ,  $1160\text{ cm}^{-1}$  and  $730\text{ cm}^{-1}$ , this being a confirmation for the presence of another calcium phosphate, anhydrous dicalcium phosphate (DCPA,  $\text{Ca}_2\text{HPO}_4$ ). Those peaks indeed are due to the vibration of P-O bond in pyrophosphate, which are originated from the condensation of two different  $\text{HPO}_4^{2-}$  to  $\text{P}_2\text{O}_7^{4-}$ [68].

Now sample 2-600°C can be analysed as well, to see in which way 2 different iron tenor could affect functional group found in the powders.

FTIR spectrum is similar to sample 1-600°C, the main difference is that peaks described by  $\beta$ -TCP are absent, this being confirmed by XRD spectrum as well, in which in case of sample 2 no tricalcium phosphate was evidenced. In fact, all peaks related to hydroxyapatite, at  $1090\text{ cm}^{-1}$ ,  $1040\text{ cm}^{-1}$  and  $960\text{ cm}^{-1}$  are present. Moreover, it is detectable peak at  $3573\text{ cm}^{-1}$  for  $\text{OH}^-$  and two carbonate peaks, indicating also for sample a possible partial substitution of  $\text{OH}^-$  or  $\text{PO}_4^{3-}$  with  $\text{CO}_3^{2-}$ . This depending on the possible presence of carbon dioxide in the environment during the synthesis process or previous contamination of the powder which might lead to the formation of carbonate ions able to enter and dope hydroxyapatite lattice.

Again, peaks at  $\text{cm}^{-1}$ ,  $1160\text{ cm}^{-1}$  and  $730\text{ cm}^{-1}$  could be ascribed to the presence of DCPA, this determining the resonance in spectrum related to the functional group  $\text{P}_2\text{O}_7^{4-}$ , described before [68]. In fig. 3.13 is displayed sample 2-600°C

Finally Sample 1 sintered at 700°C and 800°C are compared together and with sample 1 -600°C, underlining differences and trying to look for changes related to sintering temperature. In fig.3.14 3 FTIR curves are displayed all together.

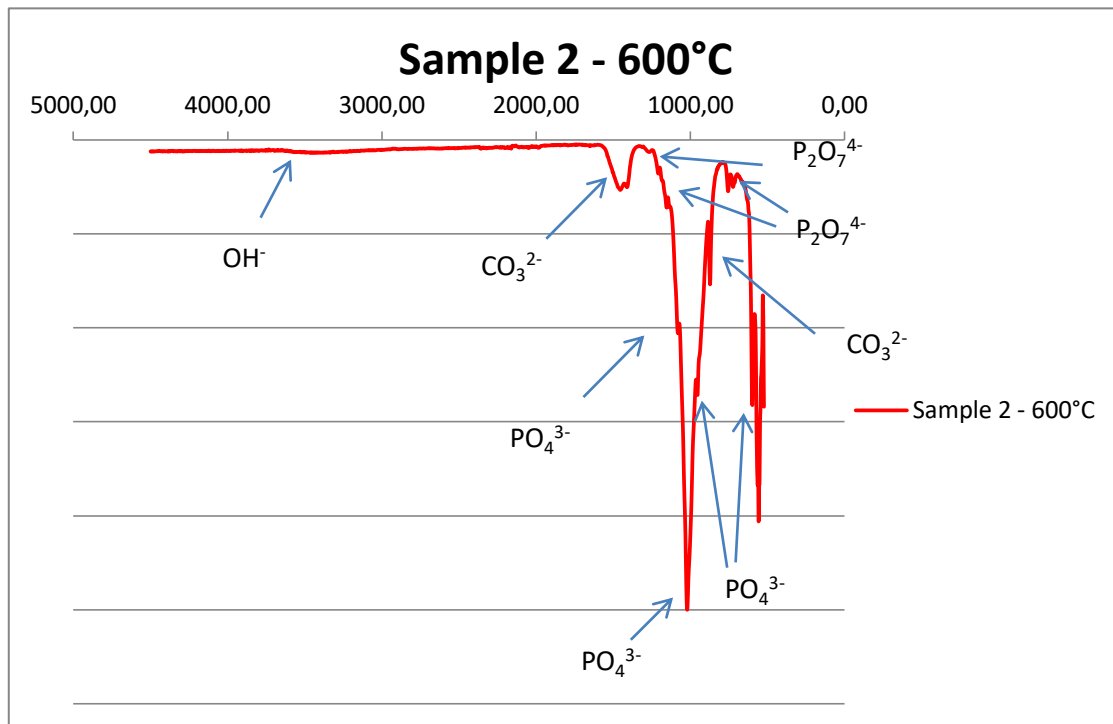
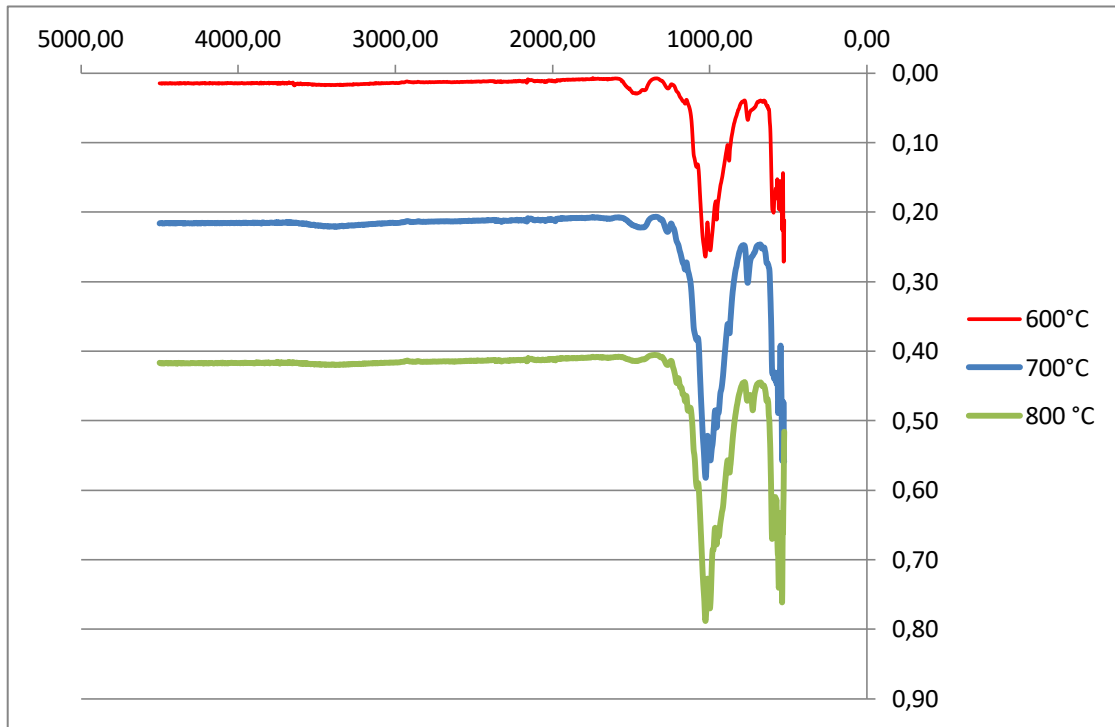


Fig. 3.13 FTIR of sample 2-600°C: all the important peaks are labelled showing the functional group they refer to.

All spectra are very similar, just some differences are clear and deserve to be deeper. First of all the broad peak between 1400 cm⁻¹ and 1500 cm⁻¹ gets shorter and a bit wider as sintering temperature is increased, meaning that CO₃²⁻ ions amount reduces with temperature. All the other peaks of hydroxyapatite and other phosphate compounds continue to be present at any sintering temperature. To conclude, it is interesting to analyse the big peak at 1000 cm⁻¹. In particular, as sintering temperature increases, it gets sharper and bigger, this meaning an increased crystallinity of the powder. It is evident for powder sintered at 800°C, this confirming what has been found out with XRD which showed an increase in crystallinity for sample 1 - 800°C when compared to Sample 1 – 600°C.

Same kind of approach and comparison can be done for Sample 2 sintered at 600°C, 700°C and 800°C, as it is displayed in fig. 3.15.



**Fig. 3.14** FTIR curves of sample 1 sintered at 3 different temperatures.



**Fig. 3.15** FTIR curves for sample 3 sintered at 600°C, 700°C and 800°C.

All 3 samples show the presence of typical peaks related to hydroxyapatite. A special focus should be done on sample 2-700°C. In fact, as  $\text{CO}_3^{2-}$  typical peaks almost disappear displaying a reduced in the quantity of this ion, other peaks related to  $\beta$ -TCP appear. In fact peaks at  $1130\text{ cm}^{-1}$  and  $960\text{ cm}^{-1}$  are typical for the presence of tricalcium phosphate [67]. Probably other phosphate such as anhydrous dicalcium phosphate is present in this sample, this being underlined by the increase in dimension of the peak at  $730\text{ cm}^{-1}$  and others at  $1205\text{ cm}^{-1}$  and  $1160\text{ cm}^{-1}$ . The same dicalcium phosphate is evidenced in sample sintered at  $600^\circ\text{C}$ , but seems to disappear in sample sintered at  $800^\circ\text{C}$ . In fact, no peaks related to DCPA or  $\beta$ -TCP can be evidenced in this sample.

For what concerns sample 2-700°C presence of  $\beta$ -TCP is evidenced also in XRD, this confirming its presence in this sample.

Finally, all FTIR spectra have been analysed, in general not big differences were found out in all the sample when compared to FTIR spectra of hydroxyapatite than can be found in literature [69].

Now in next paragraph results of magnetic hyperthermia test performed on samples are presented.

### ***3.4 Vibrating Sample Magnetometer (VSM) analysis***

Analyzing curves resulted from the VSM analysis is very useful to understand what is the magnetic behaviour of the particles. In fact, magnetic field is applied at different temperature and in this condition it is possible to evaluate how magnetic moment of particles changes in relation with the field applied. If magnetization remained also after the external field is removed, it is necessary to apply an opposite magnetic field to have the magnetization drop to zero again. The opposite magnetic field which is necessary to apply is called coercivity camp ( $H_c$ ). Moreover, it is necessary to estimate the value of the coercivity camp to classify the magnetic behaviour of particles : ferromagnetic ( $H_c > 0$ ) or superparamagnetic ( $H_c = 0$ ).

Also analysis in field cooled and zero field cooled are performed, useful to underline magnetic transition into samples, indicating blocking temperature as well.

Unluckily, due to a technical problem of the tool used for the analyses, it has not been possible to complete all the measurements. It is therefore possible to present some results and discuss them to present some conclusions.

Referring to sample 1-600°C, magnetization curves at two different temperatures are presented in fig.3.16. As can be seen in both case a paramagnetic behaviour is shown, while in the case of the test performed at 5 K , slope of the curve is bigger.

Interesting to present the comparison between sample 1-600°C and sample 2-600°C. In fact, in case of sample 2 – 600°C test has been performed just at 10 K.

The results is displayed in fig. 3.17.

As can be seen, the shape of the curve is different when compared to sample 1-600°C. In fact in case of sample 2 the curve present a small hysteresis, approximated to zero.

In this case, a weak super-paramagnetic behaviour can be underlined. Therefore, analyses at higher temperature should be performed also for sample 2-600°C, in order to understand the difference in behaviour and to have information about blocking temperature.

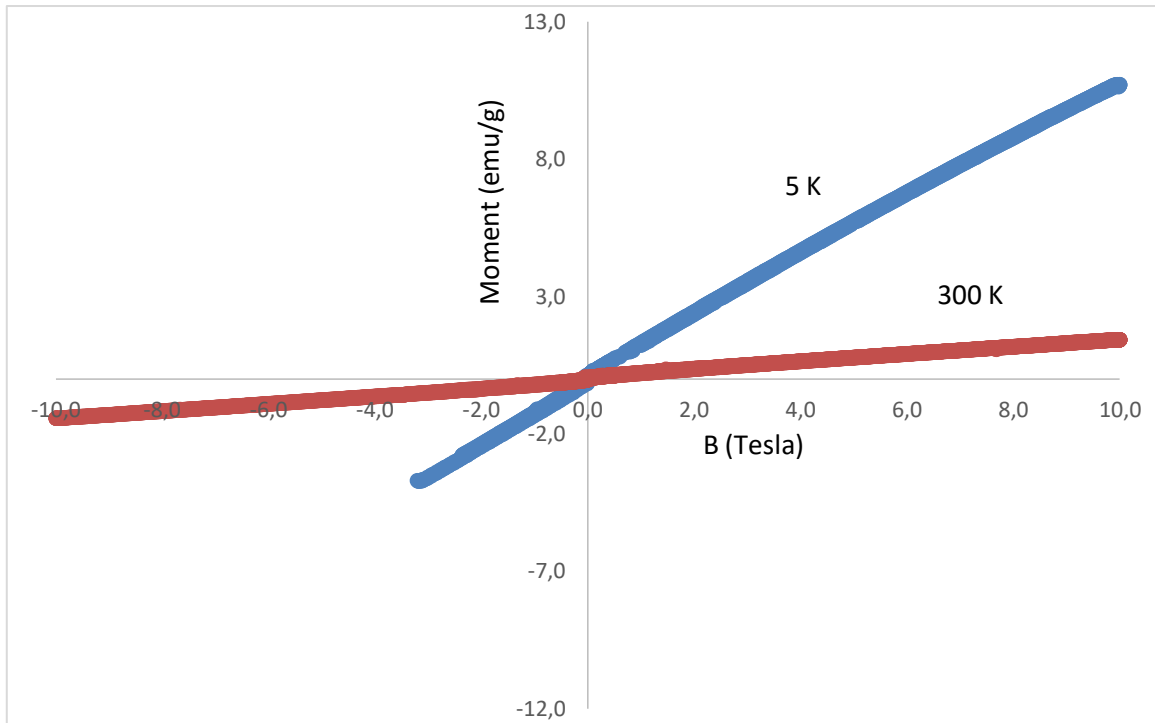


**Fig. 3.16** Magnetization vs applied field for sample 1 – 600°C. Test performed at 2 different temperature.

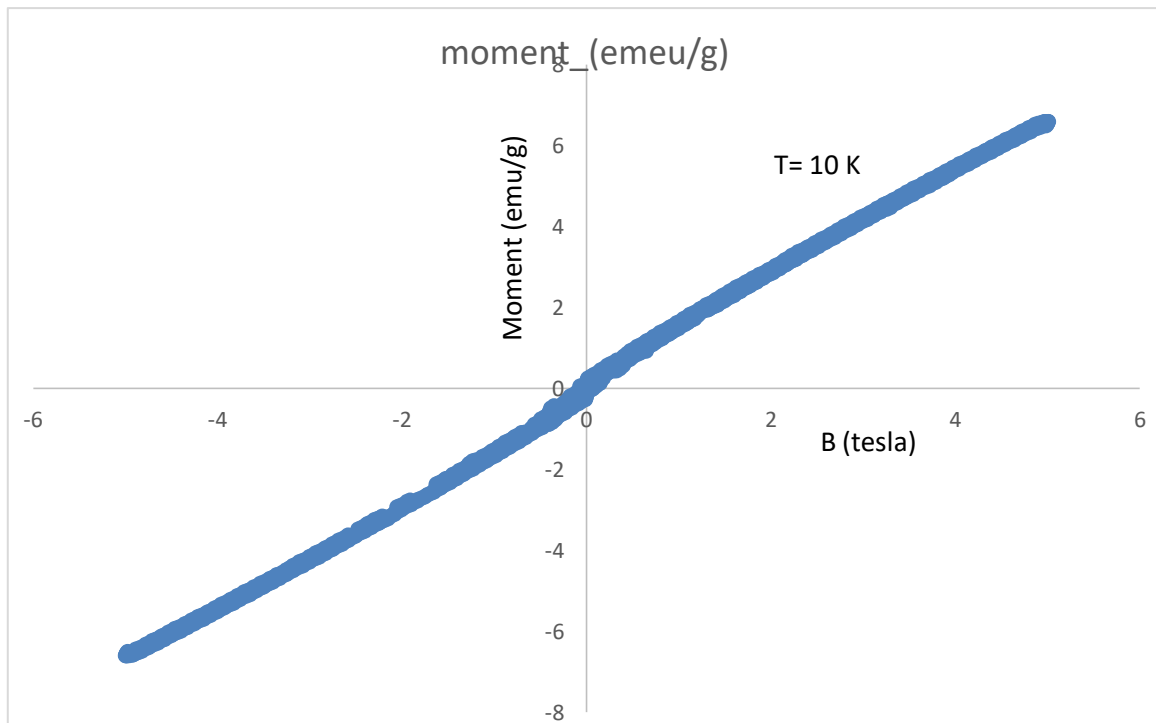


**Fig. 3.17** Magnetization vs applied field for sample 2-600°C.

In case of sample 2-600°C it is interesting to present also the curve that present variation of magnetic moment when temperature is varied, in test FC (field cooled) and ZFC (zero field cooled). 2 important conclusions can be drawn looking at the curve in fig. 3.18. Firstly, at 50K there is a magnetic transition. Which deserves to be studied more. Finally, since the two curves overlap at around the temperature of 100K, this can be considered the blocking temperature in the sample. This showing the different in magnetic behaviour for particles at different temperatures.

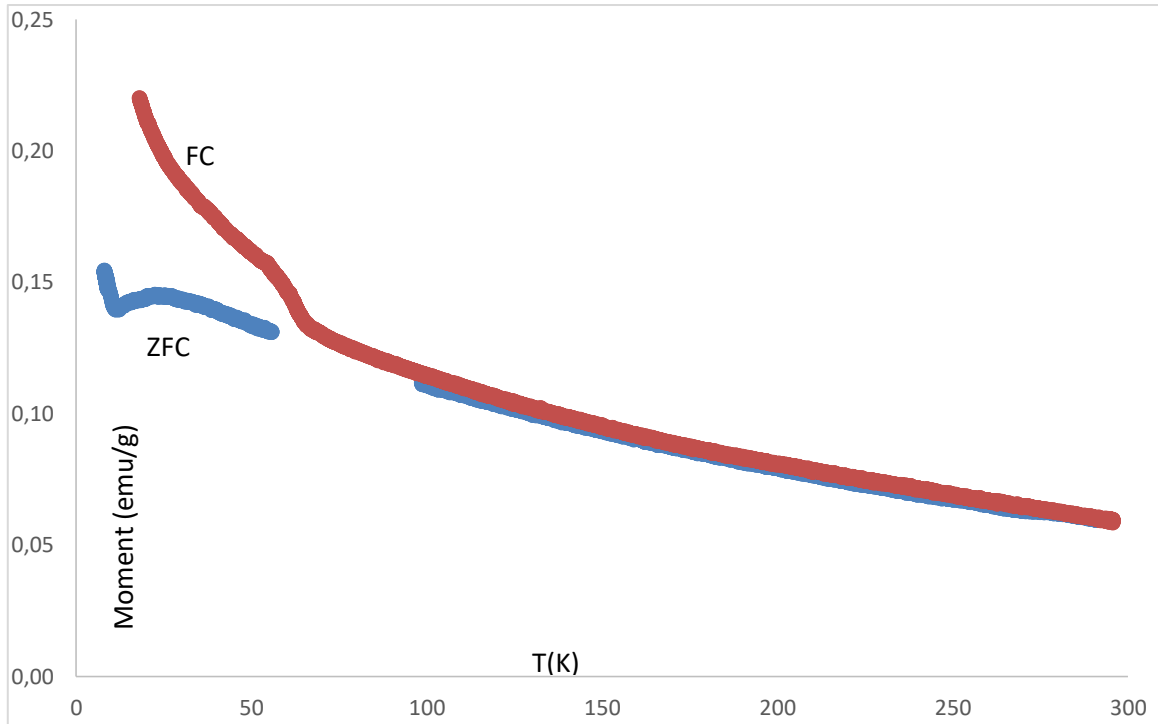


Fig. 3.18 Magnetic moment vs temperature for sample 2-600°C. Results of both FC and ZFC tests are displayed.

Very interesting is the behaviour of sample 1-700°C, whose resulting curve for the testing temperature of 300K is displayed in fig.3.19.

As can be seen, the shape of the curve is similar to sample 2-600°C, this showing a superparamagnetic behaviour of particles, while the  $H_c = 0$ . If compared to sample 2-600°C, behaviour seems stronger.

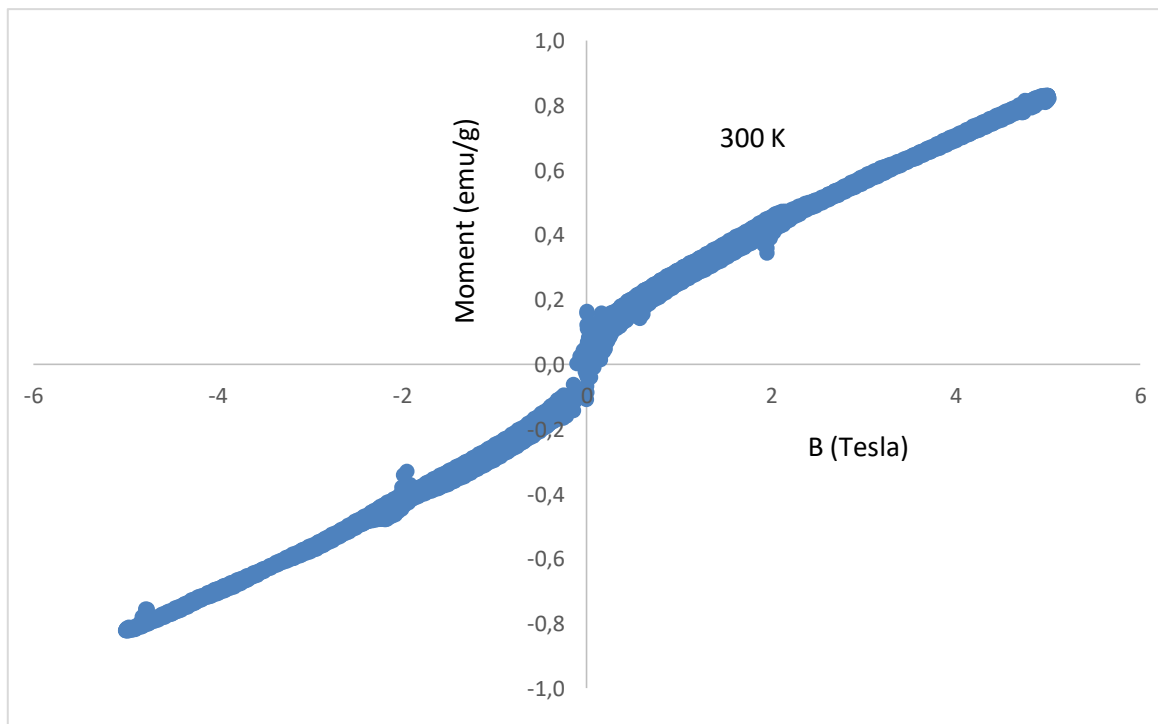


Fig. 3.19. Magnetic moment vs magnetic field applied for sample 1-700°C.

In fig. 3.20 the curve displaying variation of magnetic moment in varying the temperature.

Also in case of sample 1-700°C is presented a magnetic transition at 50K, similar to what has been found in case of sample 2-600°C.

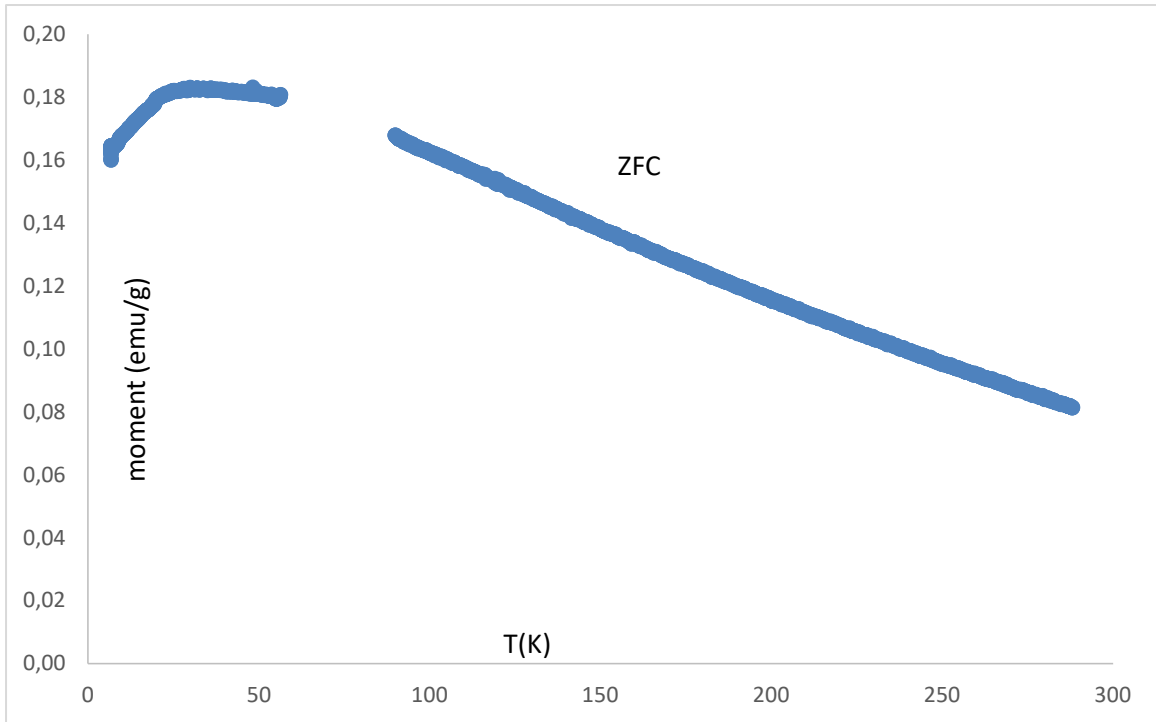


Fig. 3.20 Magnetic moment vs temperature in ZFC test for sample 1-700°C.

When analysing results of FC and ZFC test for sample 1 – 800°C it is possible to underline the presence of similar transition to those visualized for sample 2-600°C and sample 1 – 700°C. Results are presented in fig.3.21. The same magnetic transition at 50K is presented, as well as the overlap at 100K between the two curves. This setting the blocking temperature at around 100K also in case of sample 1-800°C.

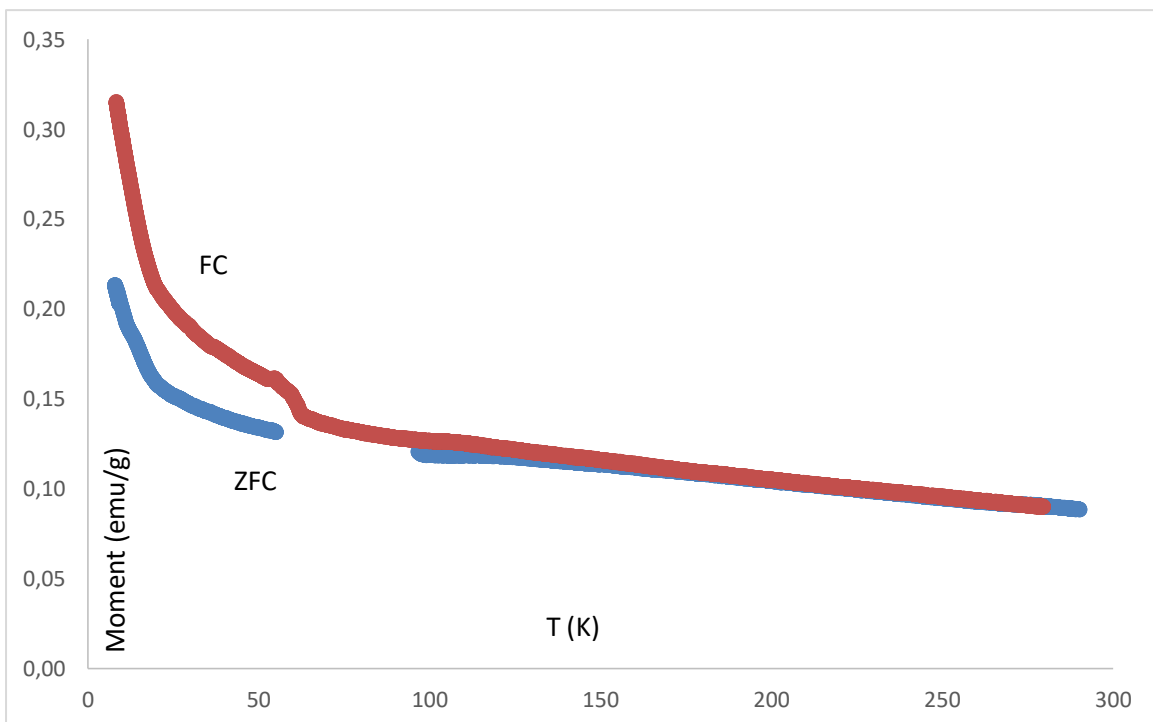


Fig. 3.21 Magnetic moment vs temperature in FC and ZFC tests for sample 1-800°C.

Finally, analysis on sample 2-800°C is carried out.

In fig. 3.22 is presented the resulting curve displaying variation of magnetic moment when external field is applied.

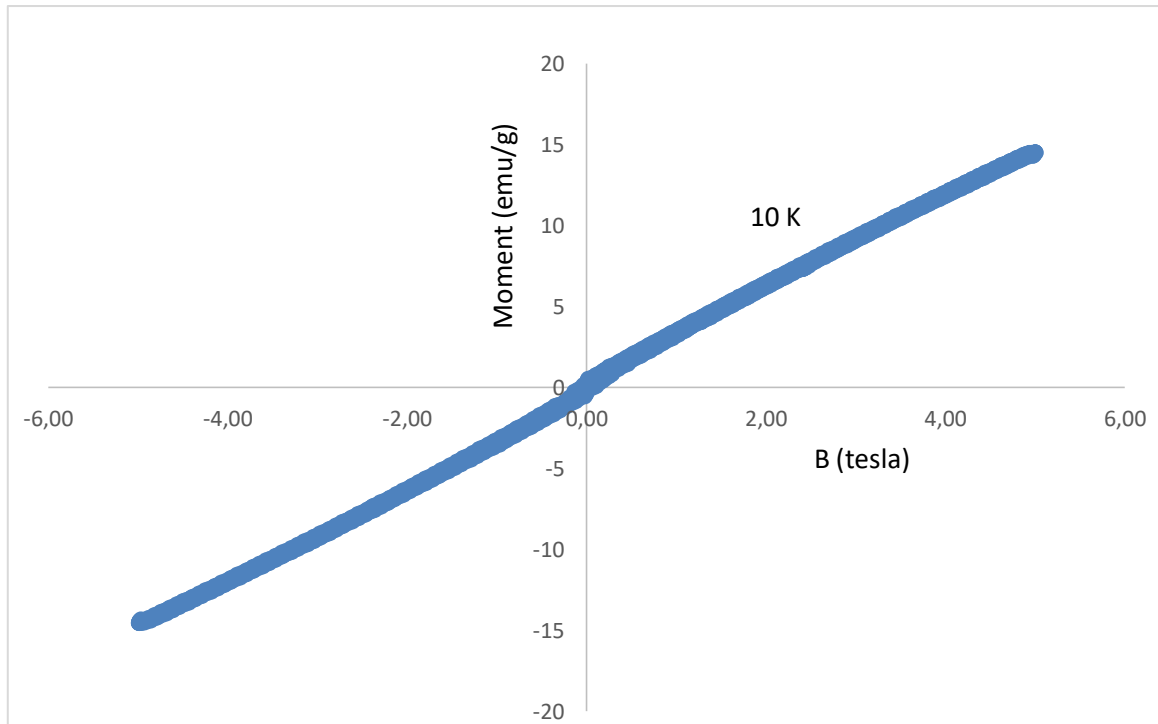


Fig. 3.22 Magnetic moment in presence of applied external field for sample 2-800°C at the temperature of 10K.

As can be seen in fig.3.22, super-paramagnetic behaviour similar to the one found in analysing other samples can be seen, with coercivity field equal to zero.

To conclude the analysis, it is interesting to present in fig.3.23 results of the FC and ZFC tests performed on sample 2-800°C.

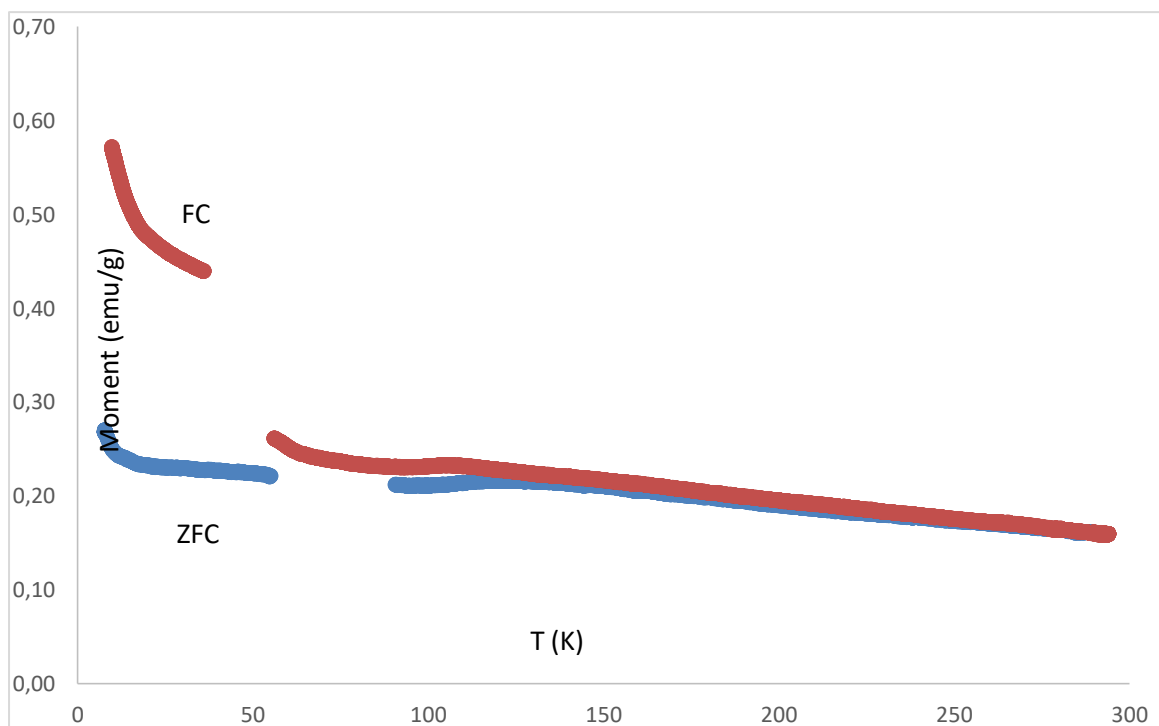


Fig. 3.23 Magnetic moment vs temperature in both tests FC and ZFC performed on sample 2-800°C.

Two discontinuities in both FC and ZFC curves represent a magnetic transition that should be deeper analysed in order to understand its nature. This probably being similar to the magnetic transition evidenced also in other samples at around the same temperature of 50K. In the same time, two curves overlap at 100K, confirming at this temperature the blocking temperature for this kind of prepared iron doped-hydroxyapatite.

*Chandra et al.*[74], and *Wu et al.*[75] has revealed super-paramagnetic behaviour in iron doped hydroxyapatite, this confirming the result of this thesis. In the same time, in *Chandra et al.*[74] investigation, some samples show an asymmetric hysteresis cycle, this probably due to a not uniform distribution of Fe ions into the structure.

As can be seen, several of samples analysed present a super-paramagnetic behaviour. This means that one of the main goal of the thesis project is fulfilled. For this reason, it is important for next investigations to strengthen some information underline in this analysis, trying to have more information about the magnetic transition displayed by the FC-ZFC curves.

For this reason, it proves to be important now to analyse results of the magnetic hyperthermia test performed on samples, to understand how they can be apply in case of hyperthermia application.

### 3.4 Magnetic thermal hyperthermia

Hyperthermia test, explained in chapter 2.2.6 *Magnetic hyperthermia analysis*, is performed on all six samples, testing the heating up tenor when an alternating magnetic field is applied.

Desired results are to increase temperature inside the body at around values of 41°C and 43°C, in an amount of time of 10 minutes. Unfortunately, considering a starting body temperature of 38°C, none of the powders has been proved able to reach this result, at the concentration of powders considered. However, some of them show a promising starting point for further development which leads to the desired goal. In fact, all samples 1 show an increase of at least 1 °C, while sample 2 show an increase in temperature just when considered the powder sintered at 800°C.

So both composition should be promising, even though probably for different reason. In fact, in case of sample 1 all sintering temperature, with different percentage of hydroxyapatite phase and some differences in structure still show an increase. On the other hand, when considering sample 2 it is important to notice and underline that the only sample showing a  $\Delta T$  is also the one in which possible traces of hematite has been found. Particularly important will be analysis related to biocompatibility of sample, to understand how this could affect biological behaviour.

By the way, sample 2 - 800°C is the one showing the biggest increase in temperature, this making it the most promising powders sintered for what concern hyperthermia. This being the reason why it is very important to evaluate its biocompatibility.

To have an improved behaviour when an alternate field is applied, it could be necessary to improve and refine powders composition and synthesis process, or simply the range of time (10 minutes) used is not enough for the desired result.

In fig. 3.24 all results are displayed, showing also relative errors.

As can be seen, no clear connection is present in the variation of  $\Delta T$  in case of sample 1, as it is oscillating when increasing sintering temperature. The only relation is that sample 1-700°C shows the biggest increase in temperature between all the sample 1, this being also the powder showing less crystallinity, smaller crystal size and smaller lattice parameters.

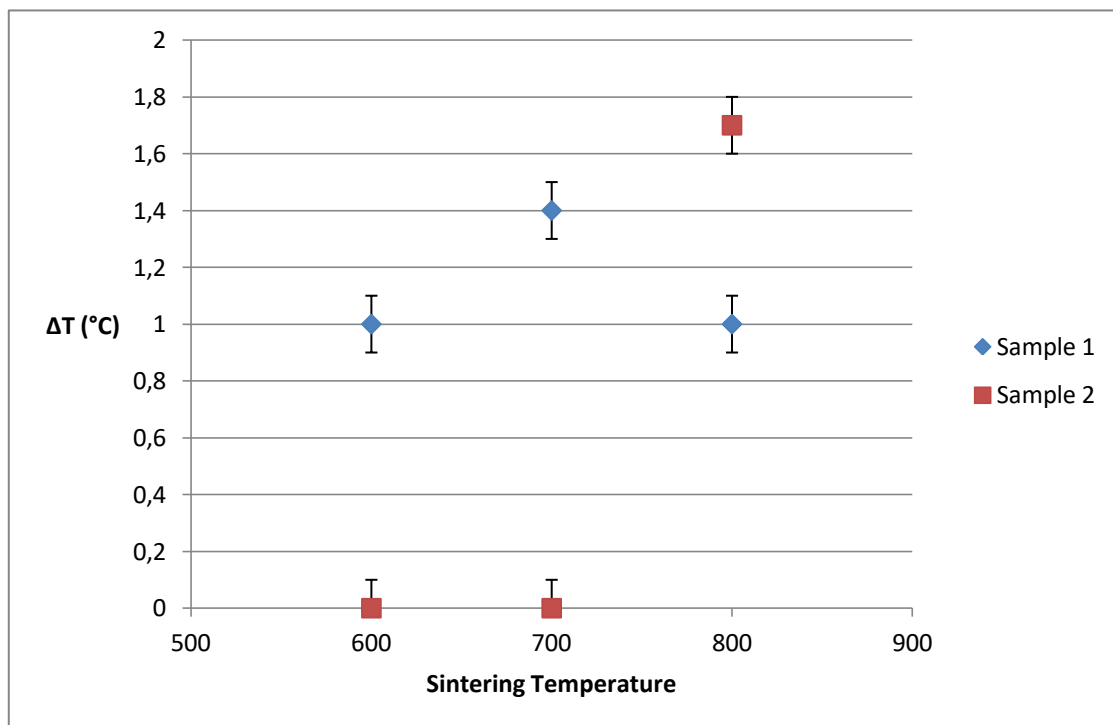


Fig. 3.24  $\Delta T$  measured for each sample when an alternate magnetic field is applied.

This still being a promising technique to produce iron doped hydroxyapatite able to show super – paramagnetic behaviour, as several successful results can be found in literature. To report one of them, *Hou et al.* [46] investigated the use of iron doped hydroxyapatite sintered through a precipitation process for cancer treatment through magnetic hyperthermia on mice. After 15 days cancer cell concentration decreases and the population reduced its growing rate.

In next chapter of characterisation technique biocompatibility tests results are displayed. This being a very important passage for the characterisation of a material which is supposed to work in contact with human body.

### 3.5 Bioactivity test

All six samples are put in SBF for 3 different timeframes: 24 hours, 3 days and 7 days. After they are removed from inside the fluid and dried, they are analysed with *Scanning Electron Microscope* looking for differences in surface morphology at different time of immersion in SBF.

Process of bioactivity follows different steps. Firstly, when hydroxyapatite is inserted inside the fluid media  $\text{Ca}^{2+}$  start getting released, followed by  $\text{PO}_4^{3-}$  ions. After that, when solubility limit for  $\text{Ca}^{2+}$  inside the medium is reached, it starts depositing again on HAp surface. This quickly determining an excess of positive charges on the surface, attracting  $\text{PO}_4^{3-}$  ions from inside the fluid. Finally, a layer of hydroxyapatite is created, being able to attract proteins from inside the fluid, that are responsible for the formation and growth of new bone [70].

Firstly Samples 1 – 600°C is analysed, in all the 3 pictures taken at 3 different exposure time to SBF. Moreover, as a comparison it is considered a picture of powder not exposed to the fluid as a comparison.

In fig. 3.25 is showed picture of Sample 1 – 600°C in form of powder.

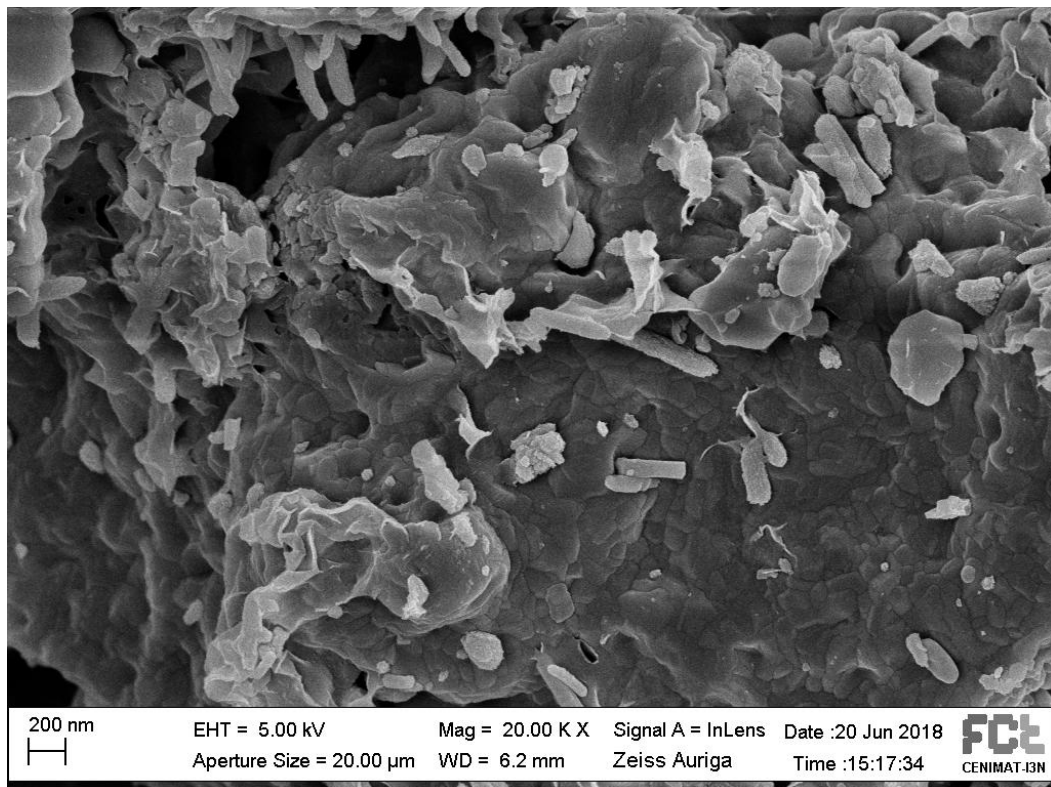
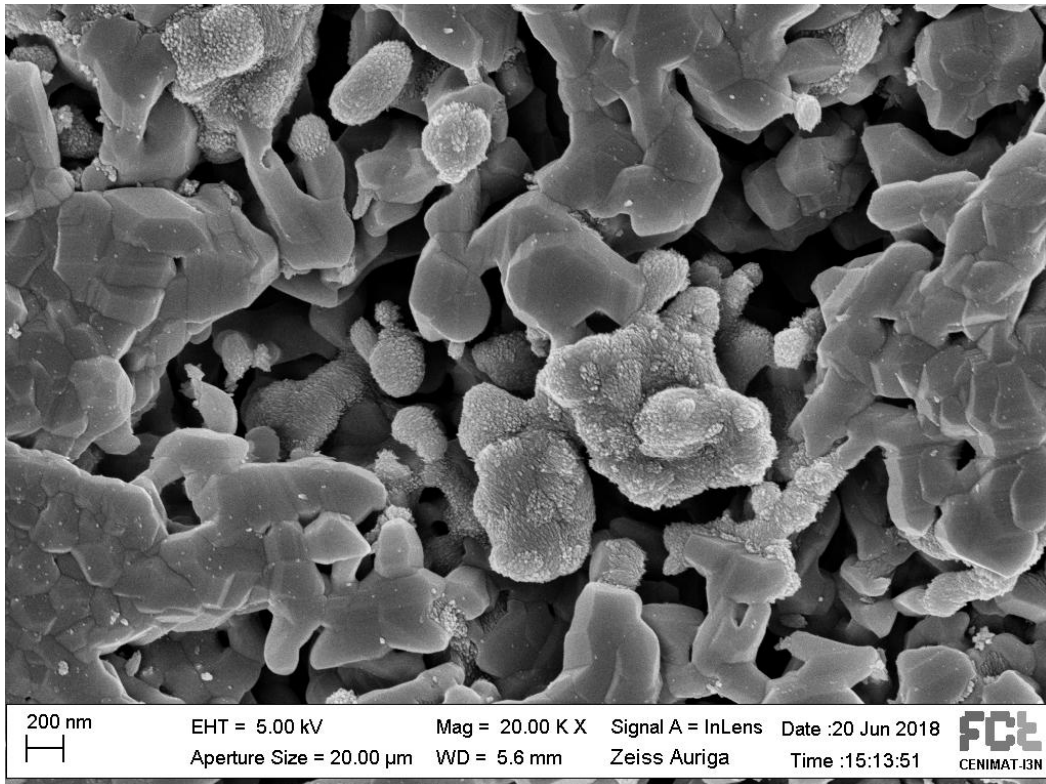


Fig. 3.25 SEM image of Sample 1 – 600°C not inserted in SBF.

A coherent structure can be seen, with the presence of elongated form of crystal. In fig. 3.26 is possible to see Sample 1 – 600°C after 24 hours inside the fluid.



**Fig 3.26** SEM image of Sample 1 – 600°C after 24 hours of immersion in SBF.

After 24 hours in SBF traces of interaction with the fluid can already be seen. In fact, those white spots on the surface of hydroxyapatite layers are the beginning of reaction between material and the fluid. In fig. 3.27 and 3.28 it is possible to see the bioactive interaction advancing and interesting larger part of the analysed material.

In the 3 days sample, larger part of material is covered with hydroxyapatite layer, not just some part like in the 24 hours sample, where probably just the beginning of reaction is visible.

It is also interesting to notice that even though layers of hydroxyapatite can be visualized more or less everywhere in the powder it doesn't seem to be so advanced locally.

Different situation is displayed for sample 1 – 600°C after 7 days. Reaction of formation of hydroxyapatite layer seems to be more advanced locally. In some areas of the analysed surface the bioactive reaction seems to be more advanced, this probably due to a smaller size (increased surface reactivity) or different local composition, this making particles itself more or less reactive according to it.

Therefore, it is interesting to notice how the reaction doesn't seem to follow a linear rule. In fact, it seems that even though the difference in structure appears to be important after the first 24 hours of immersion, it seems to reduce its speed while time is passing.

Moreover, in the first 24 hours the reaction seems to be fast, to then slow down. In fact, big difference can be seen between sample at 24 hours and powder not exposed to SBF, while small differences can be seen when compared to the 3 days sample and to the 7 days sample. This suggesting how in the first 24 hours the formation of hydroxyapatite layer seems to be very fast.

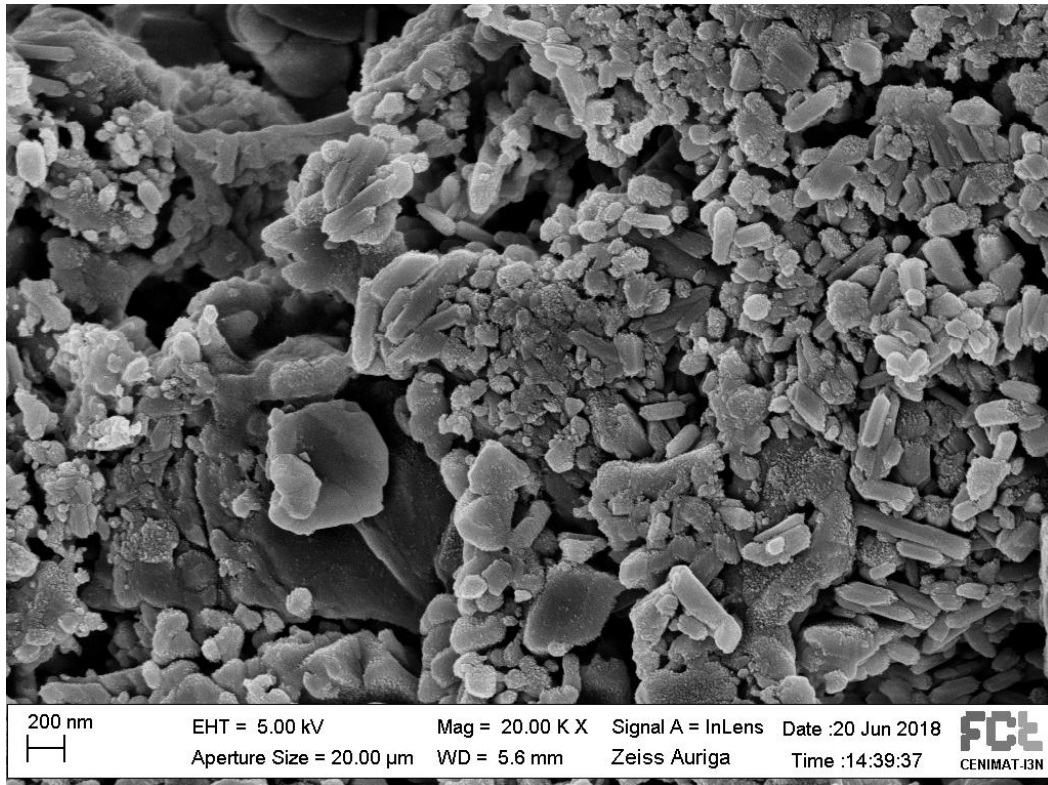


**Fig. 3.27** SEM image of Sample 1 – 600°C after 3 days immersed in SBF.

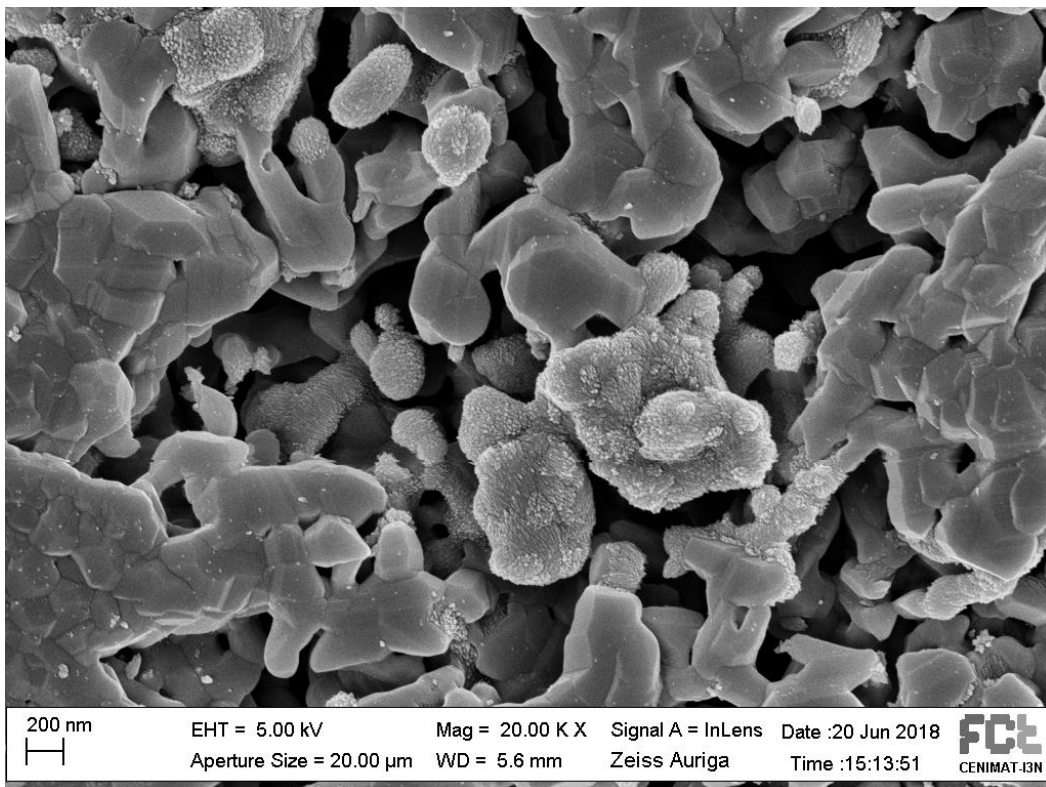


**Fig. 3.28** SEM image of the sample 1 – 600°C after 7 days of exposure time to SBF.

It is interesting to check the comparison between sample 1 – 600°C but with a different grade of magnification. In fig. 3.29, fig.3.30 and fig.3.31, images of Sample 1 – 600°C are displayed.

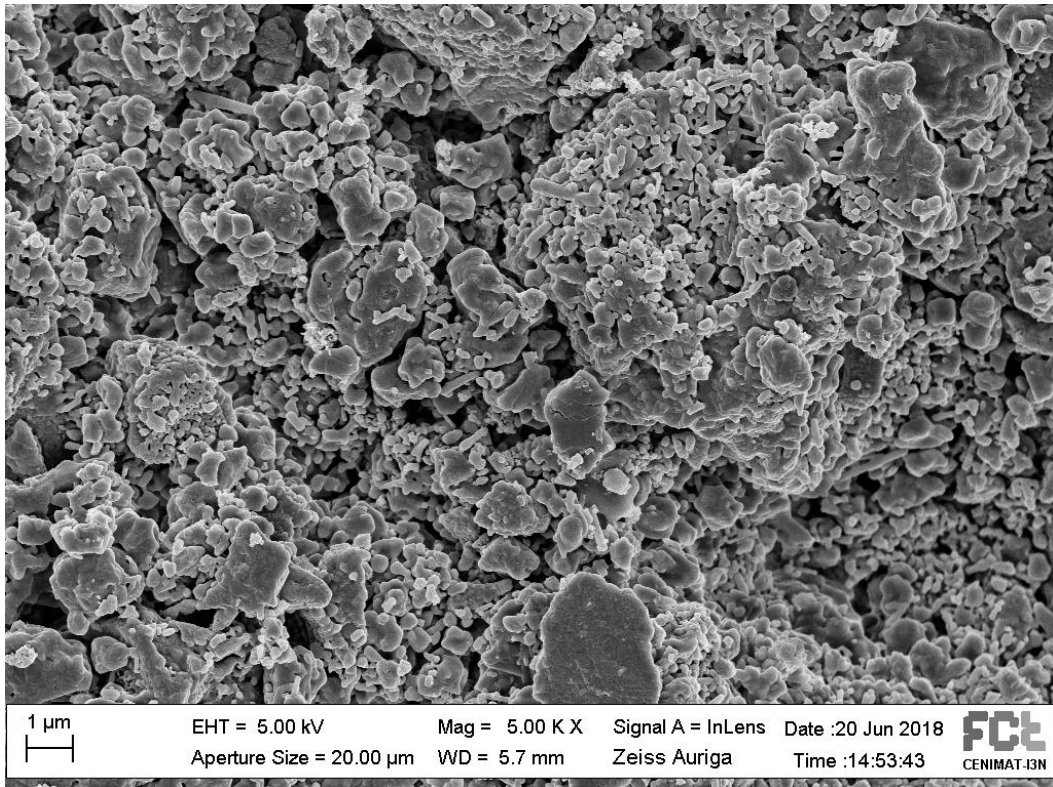


Fig. 3.29 SEM image of Sample 1 – 600°C after 24 hours of immersion in SBF.

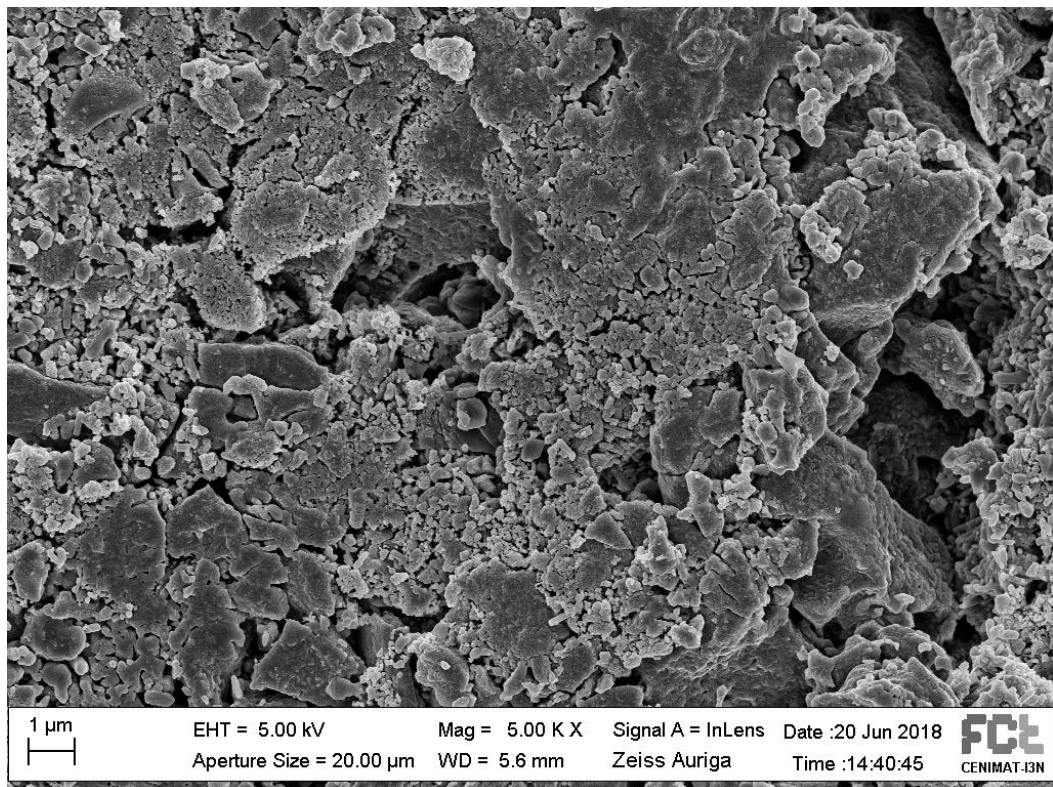
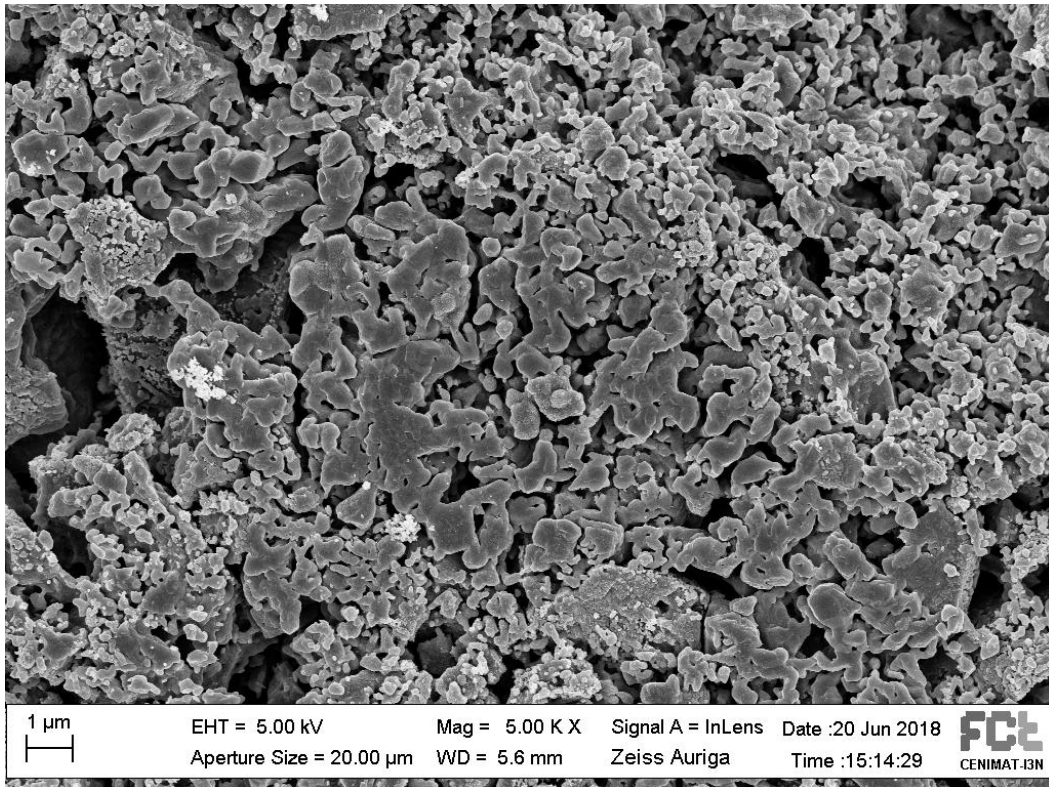


Fig. 3.30 SEM image of Sample 1 – 600°C after 3 days of immersion in SBF.



**Fig. 3.31** SEM image of Sample 1 – 600°C after 7 days of immersion in SBF.

Apparently, Grains appear to coalesce as increasing exposure time. In fact, as border between particles seem clear after 24 hours, they are not so clear after 7 days. Probably this is due to the advance of the reaction for formation of hydroxyapatite.

Before passing to the comparison between different sample composition, it is interesting to focus on sample 1 composition, considering behaviour of Sample 1 – 700°C in SBF.

In fig. 3.32 it is displayed image of Sample 1 – 700°C powders not exposed to the medium fluid.

First impression when compared to sample 1 – 600°C powders, it is of an increased coalescence between grains, this probably depending on the higher sintering temperature.

The overall idea of a hexagonal cell structure, considering the grain shape, is underlined.

When considering bioactivity and so samples exposed to SBF, the reaction advances and evolves in a very similar way in sample 1 – 700°C when compared to sample 1 – 600°C. Even though there are not big differences in the first step of the hydroxyapatite layer formation, this interesting the first 24 hours of exposure in the same way in both samples. It is quite different and deserves a small focus the aspect of powders after 7 days of exposure displayed in fig.3.33. In fact, reaction seems to be more advanced, as it interests in a deeper way more part of material.

That white structure that can be seen in the upper part of the picture, are apatite crystals growing due to the contact with the fluid.

From this it can be supposed that sample 1 -700°C shows more bioactivity on the long term when compared to sample 1 – 600°C.

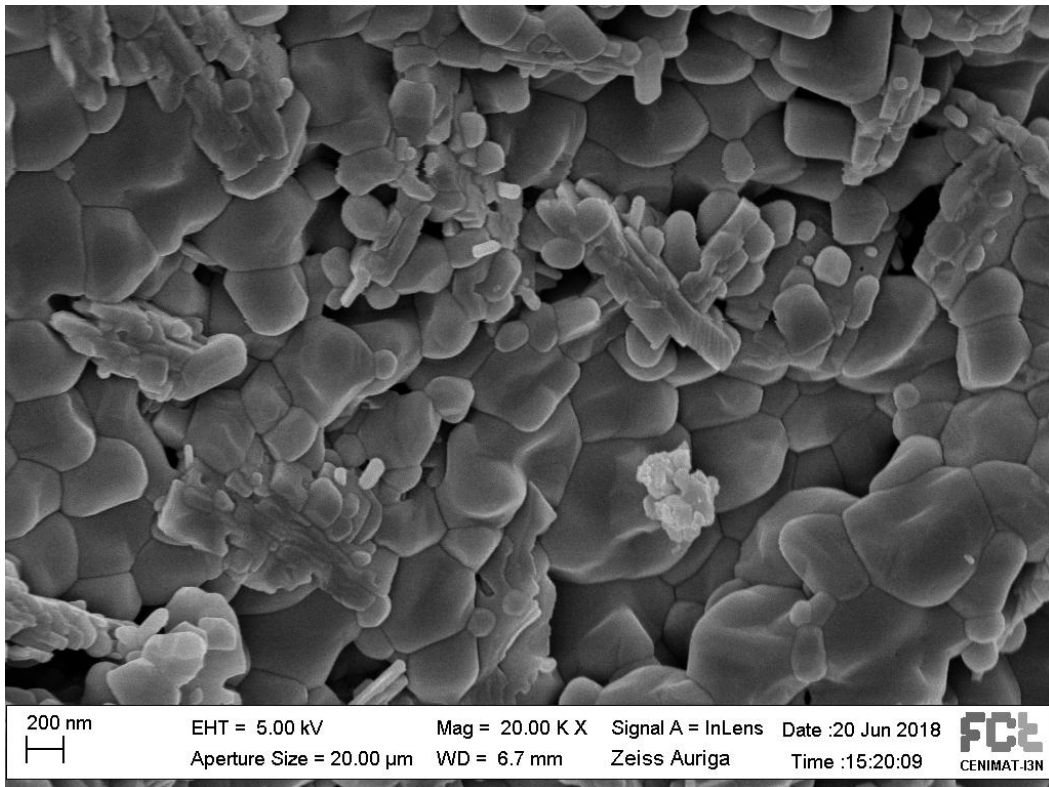


Fig. 3.32 SEM image of sample 1 – 700°C powders not exposed to SBF.

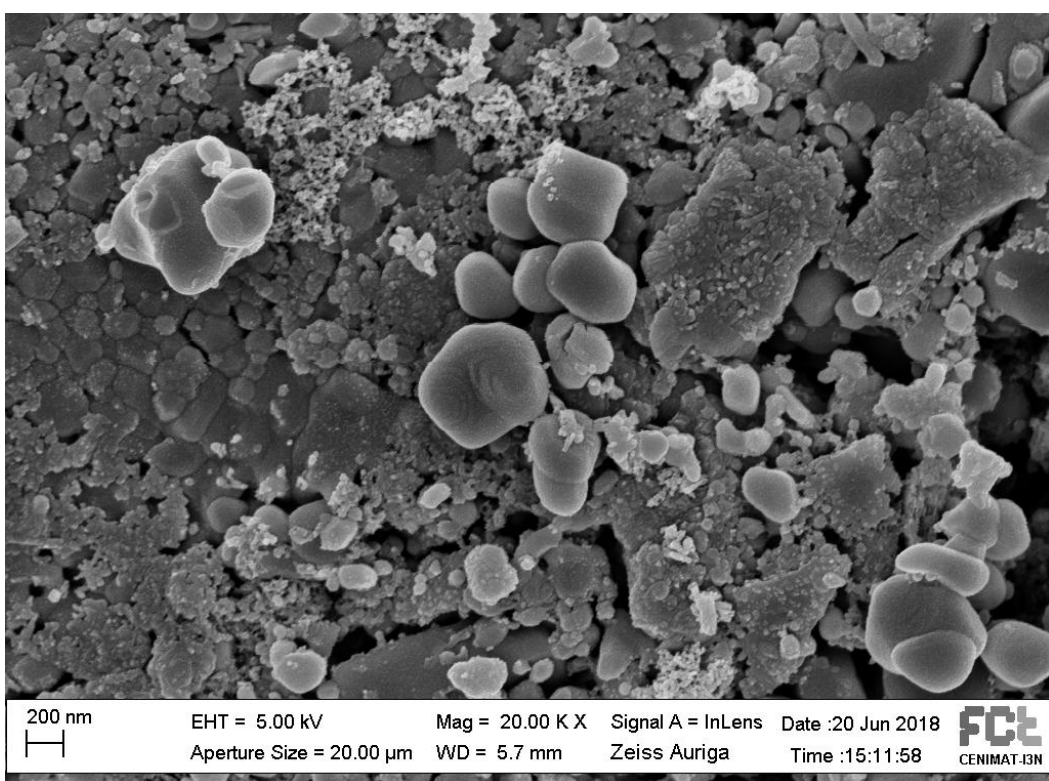


Fig. 3.33 SEM image of sample 1 – 700°C after 7 days of exposure to SBF.

Sample 1 – 800°C doesn't present similar behaviour when in contact with SBF, in fig. 3.34 is reported the image related to exposure time of 7 days.

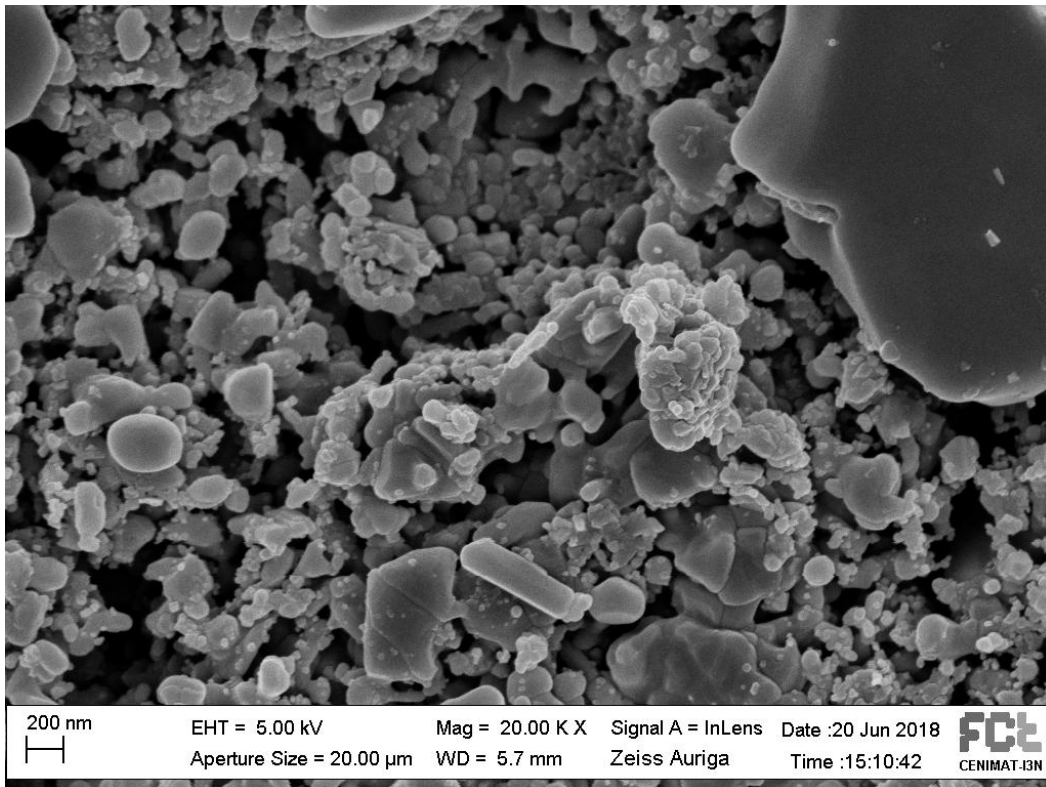


Fig. 3.34 SEM image of sample 1 – 800°C after 7 days of exposure to SBF.

As a comparison it is now interesting to evaluate bioactivity behaviour of sample 2 contains less amount of iron than in sample 1. It is therefore possible to estimate in which way bigger amount of iron could visibly affect bioactivity of the material.

Sample 2-600°C in form of powders have been analysed using SEM and is displayed in fig. 3.35. It has not been put in contact with SBF and can be used as a comparison with sample 2 – 600°C at different exposure time.

In fig. 3.36 is reported sample 2 – 600°C after 24 hours exposed to SBF.

It can be compared to not exposed powders and it can be easily noticed traces of apatite deposition on the surface, already after 24 hours.

Even though 24 hours is enough to see first steps of the reaction, it is less advanced compared to what happens in the same range of time to sample 1 – 600°C.

The aspect of the neo-formed apatite is the same as the one formed in all samples with composition 1, this meaning the same kind of reaction, even though at a different rate.

Sample 2 contained smaller amount of iron inside and it shows smaller biocompatibility or at least, smaller reaction speed. It can be supposed that a larger amount of iron favoured the formation of apatite on the surface, increasing in this way biocompatibility of the doped hydroxyapatite when compared to the normal one.

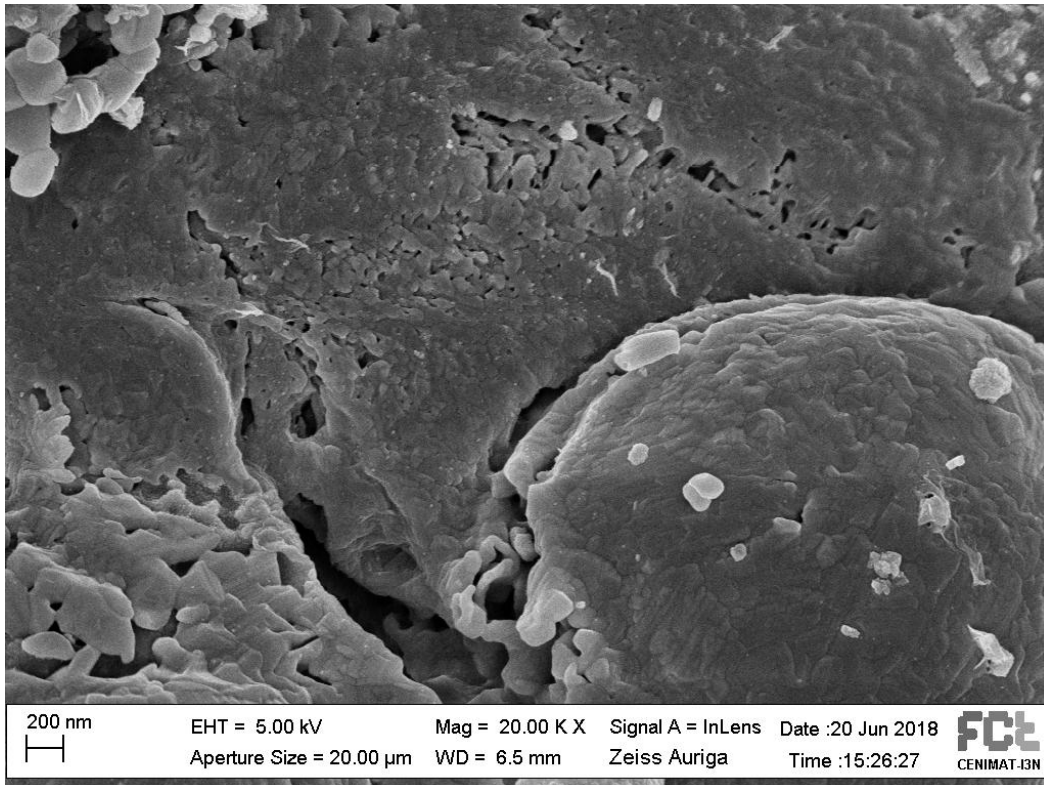


**Fig. 3.35** SEM image of Sample 2 – 600°C as powders, not put in contact with SBF.

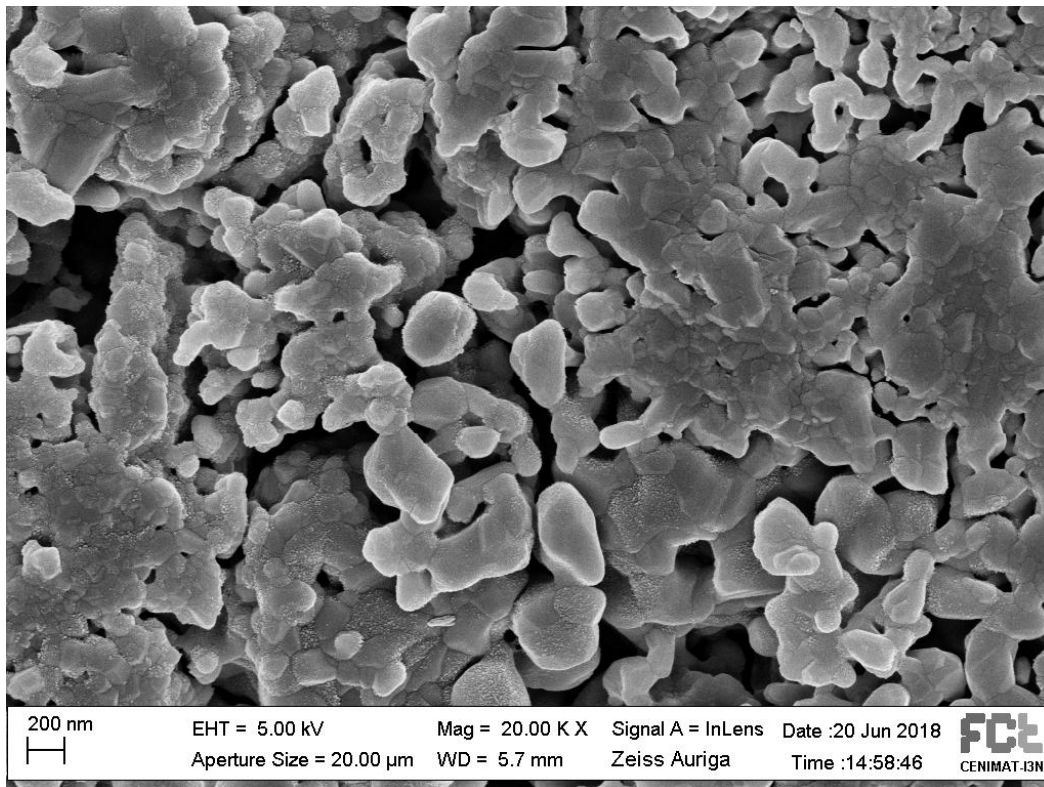


**Fig. 3.36** SEM image of sample 2- 600 °C after 24 hours of exposition to SBF.

In fig. 3.37 is displayed sample 2 – 600°C after 3 days of exposition to the fluid.

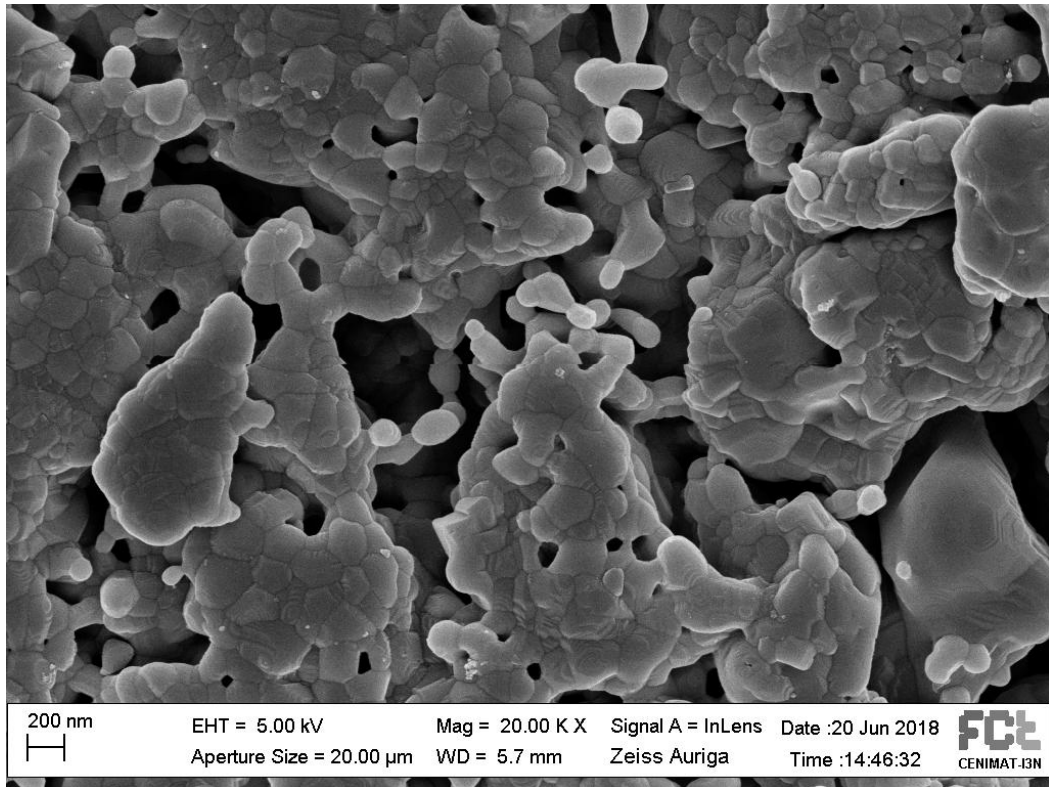


**Fig. 3.37** SEM image of sample 2-600°C after 3 days exposed to SBF.

Very few differences can be seen between sample after 3 days and the other one after 24 hours. In fact, just few small white crystals can be seen and the reaction didn't proceed so much when compared to sample after 24 hours. In fig. 3.38 sample 2 – 600°C after 7 days exposed to SBF is displayed.

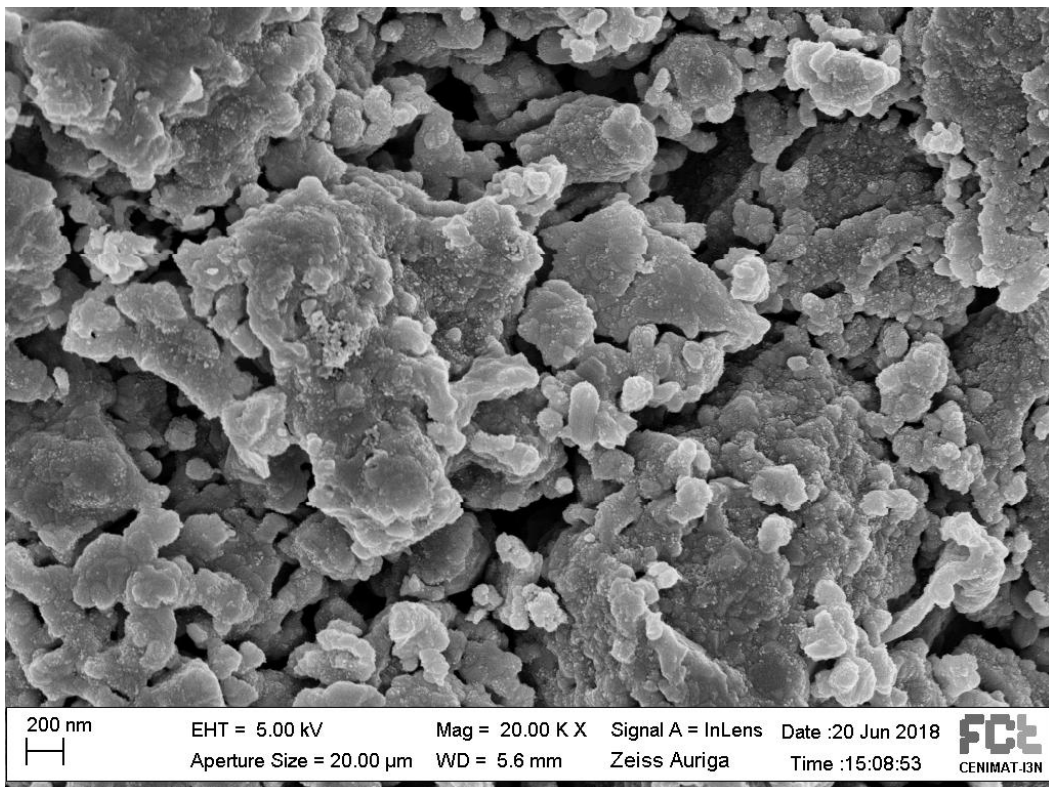


**Fig. 3.38** SEM image of sample 2 – 600°C after 7 days in SBF.

After 7 days, bigger differences can be seen, as the reaction advanced enough to reach all the surface, this being clear for the presence of white crystals and the rough aspect of the surface. Therefore, it continues to show less apatite than sample 1 – 600°C after the same exposure time.

It can therefore be supposed that higher amount of iron implies more bioactivity not just for what concern speed, but also on the long term. *Ereiba et al.* [71] reached the same conclusion in analysing HAp doped with different amount of iron.

Interestingly sample 2 – 700°C show lower bioactivity when compared to all other samples analysed. Probably it is due to the presence of  $\beta$ -TCP in larger quantities when compared to other sample with same composition.

In fig. 3.39 sample 2 – 700°C is presented. No deep evidence of bioactivity can be seen, this being totally different for what seen in all other samples.

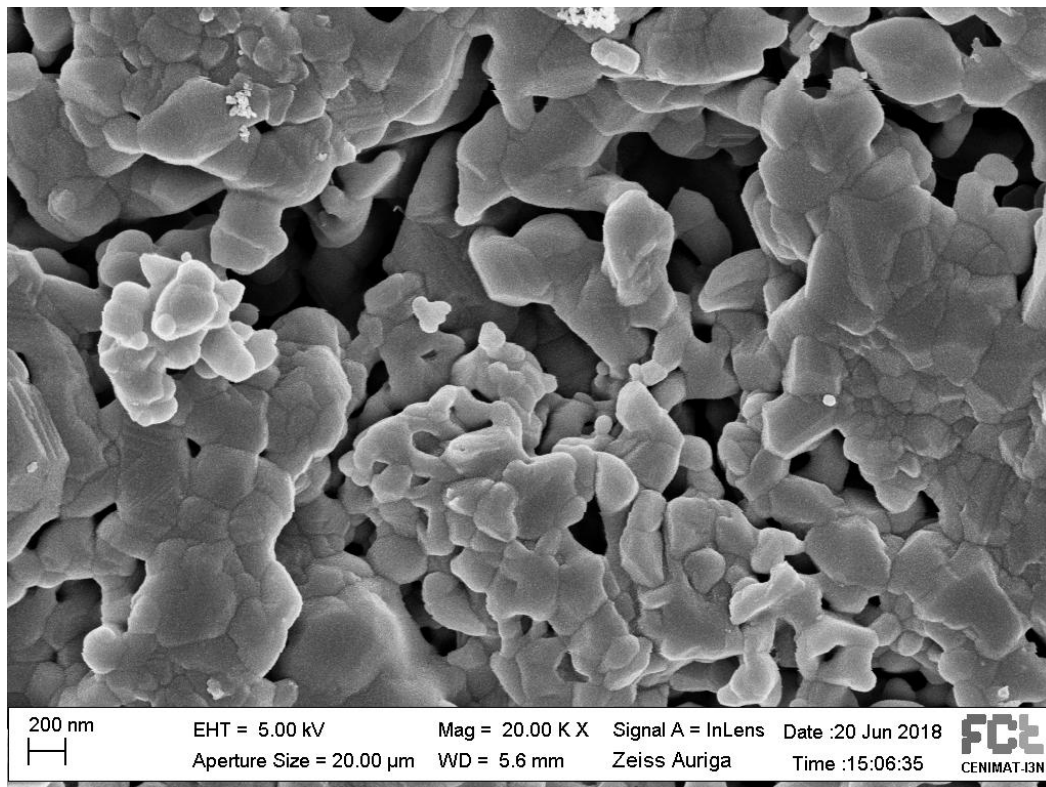


**Fig. 3.39** SEM image of sample 2 – 700°C after 7 days of exposition to SBF.

It is interesting to analyse deeper sample 2 – 800°C, that being more promising for what concern hyperthermia application.

After 24 hours of exposure to SBF sample 2 – 800°C present just few nuclei of reaction for formation of apatite on the surface, evidenced by very small white dots on the surface, as can be seen in fig. 3.40. Likewise to what happens with other sample 2, bioactivity and reaction speed seem to reduce. After 3 days of exposition the reaction is more advanced, this being evidenced by the rough and jagged surface, as can be visualized in fig. 3.41.

In fig. 3.42 the surface morphology of sample 2 – 800°C after 7 days of exposition to SBF is displayed.

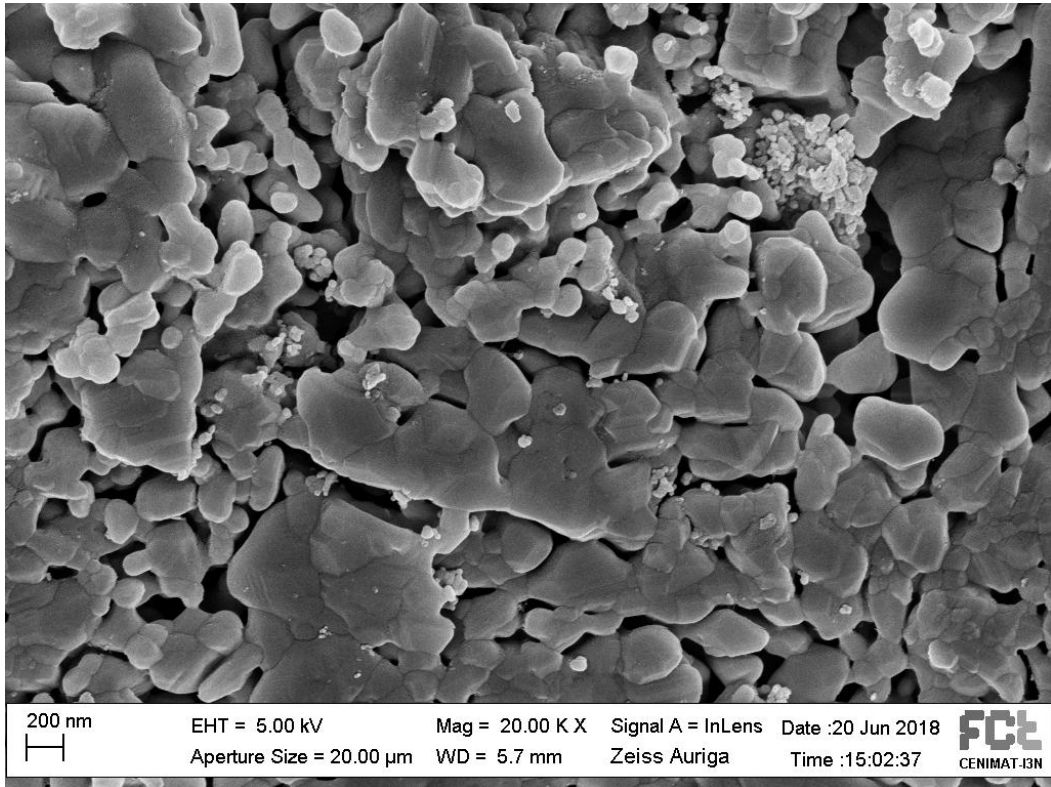


Fig. 3.40 SEM image of sample 2 – 800°C after 24 hours of exposition to SBF.

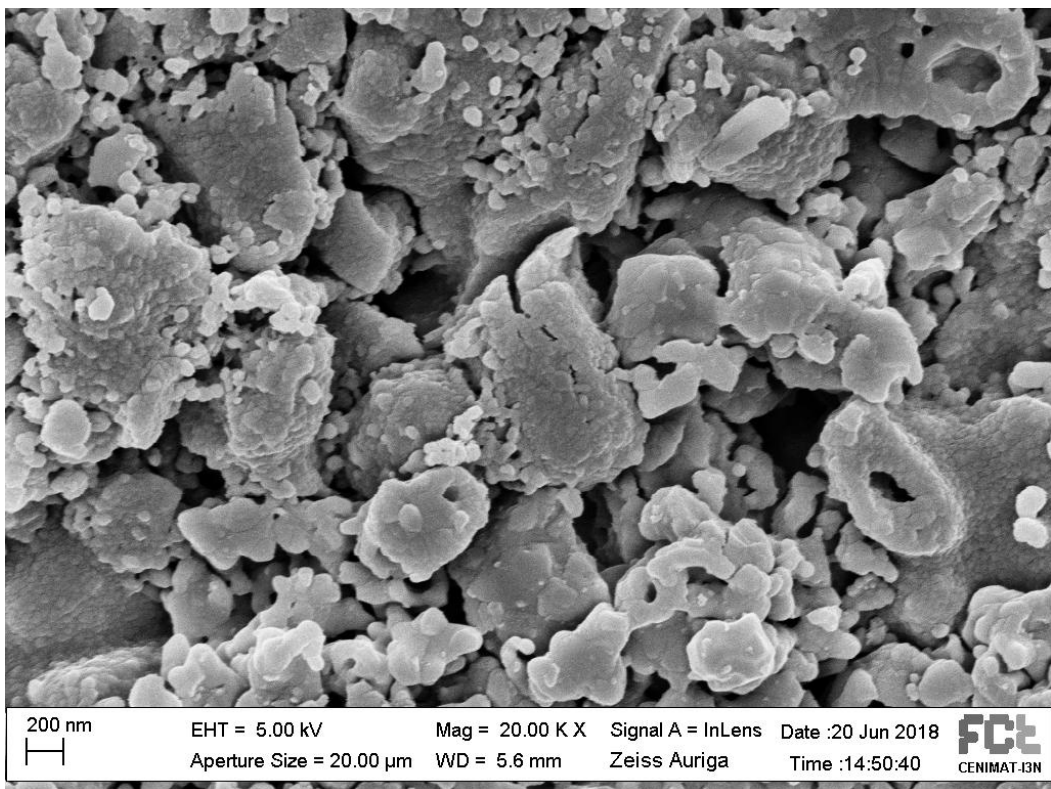


Fig. 3.41 SEM image of sample 2 – 800°C after 3 days exposed to SBF.

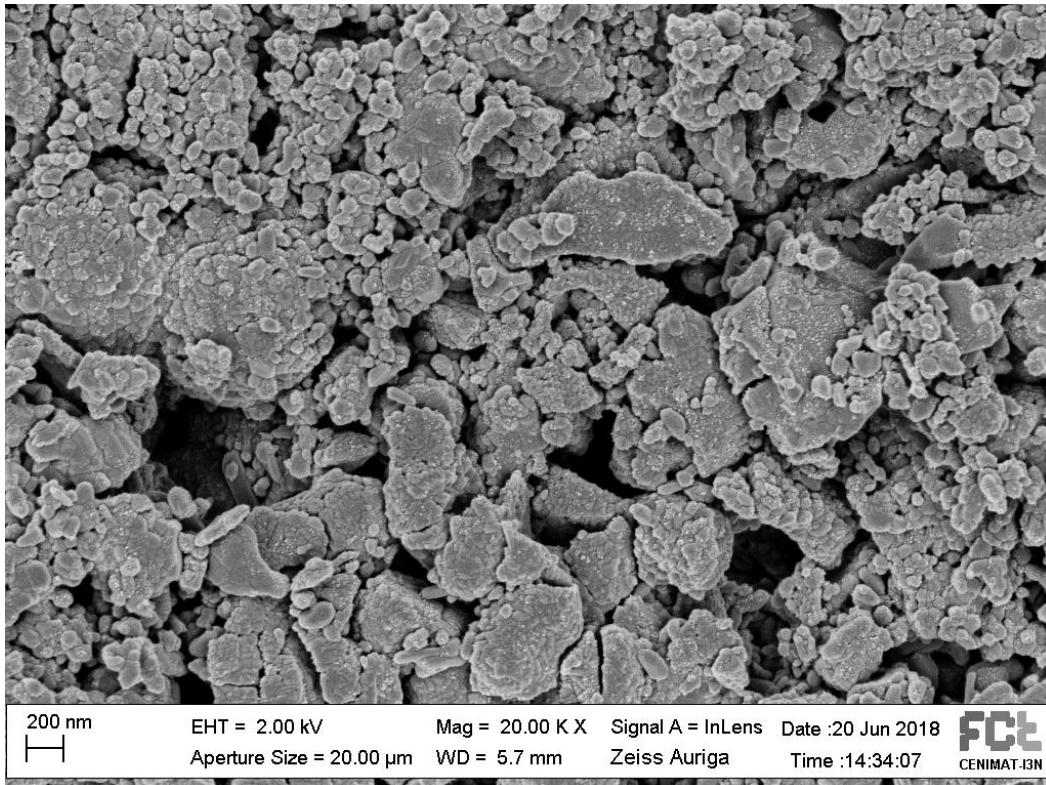


Fig. 3.42 SEM image of sample 2 – 800°C after 7 days of exposition to SBF.

After 7 days of exposition, the surface appears to be all covered by an apatite layer. Moreover, sample 2 – 800°C seems to present the highest bioactivity between all the sample 2 sintered at different temperature. It is still not the best result when compared to sample 1 sintered at different temperature. It is therefore possible to conclude that higher amount of iron in composition determines higher bioactivity of the sintered hydroxyapatite.

In both samples immersed for 3 days and 7 days an interesting structure can be found. Polygonal, elongated crystals appear to be formed, in a higher concentration, in the sample immersed for 7 days. Fig. 3.43 and fig. 3. present the structures of the sample exposed for 3 days and the structure of the sample exposed for 7 days, respectively.

As can be seen from fig. 3.35 and fig. 3.36, these structures are developed principally in one direction with a length of 10 µm. Apparently, bigger concentration of them can be found in the sample exposed 7 days to SBF.

It is hardly to explain what they are, it might be that a higher sintering temperature favoured the formation of this microstructure with an intrinsic order, or it is due to the formation of hematite inside the sample. It is interesting how they are organized between each other in case of sample 2 – 800°C exposed for 7 days, being several of them developed all around a common point, in different position inside the powders.

This being the only sample showing this microstructure, it might be connected to the higher thermal activity when exposed to a magnetic field.

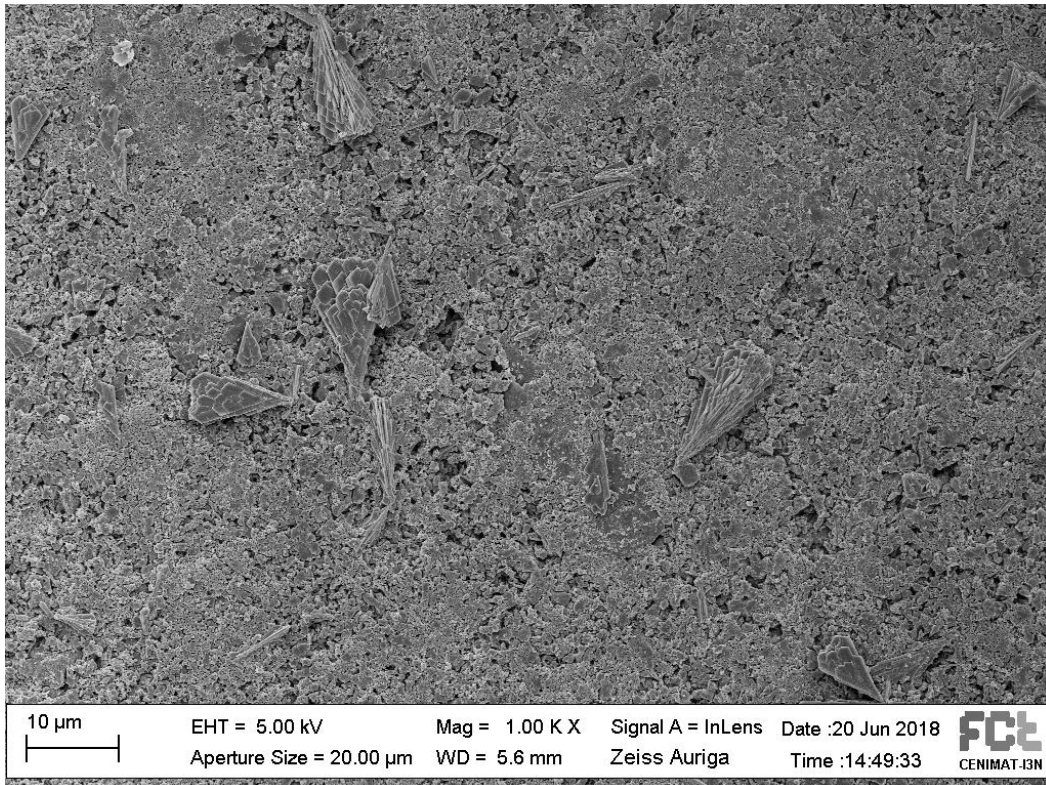


**Fig. 3.43** SEM image of structures located in sample 2 – 800°C immersed for 3 days in SBF.

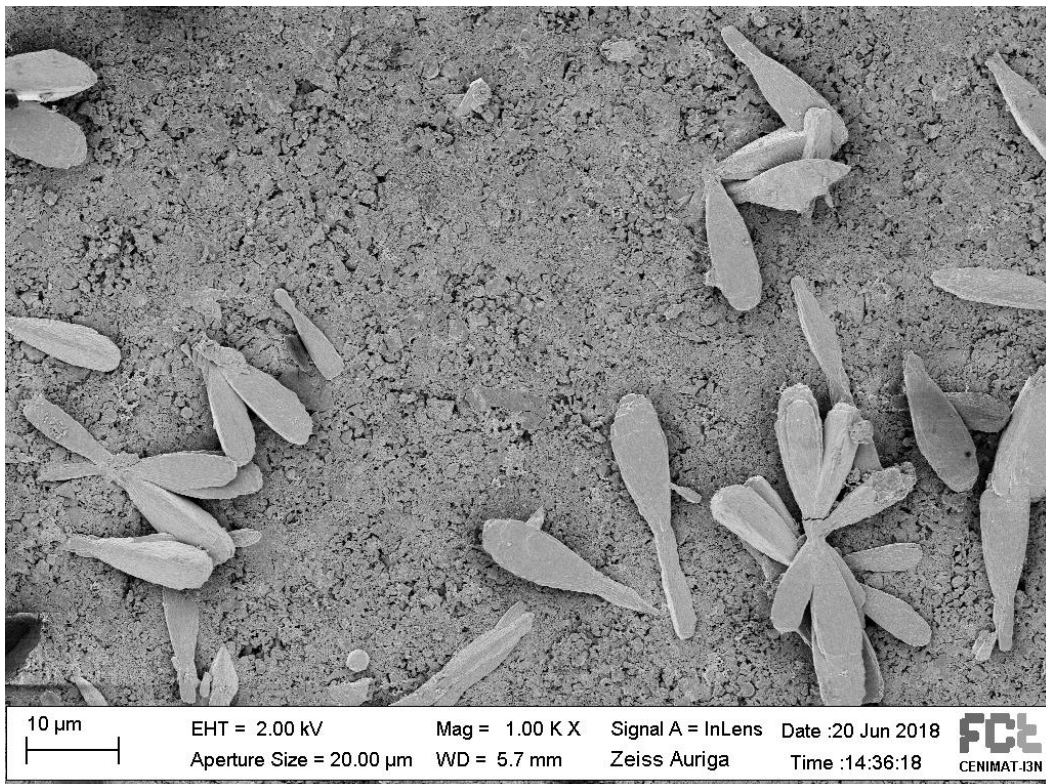


**Fig. 3.44** SEM image of structures located in sample 2 – 800°C exposed to SBF for 7 days.

EDX analysis was also performed on a wide surface that can be used to determine the atomic presence in that area, having an idea of the average composition in the powder.

It has been performed to all samples and in table 3.5 below results for sample 1 – 600°C are showed.

**Table 3.5** Result of scan composition performed on sample 1 – 600°C.

Element	Line Type	Apparent Concentration	k Ratio	Wt%	Wt% Sigma	Atomic %	Standard Label	Factory Standard	Standard Calibration Date
C	K series	0.08	0.00084	5.78	0.28	11.41	C Vit	Yes	
O	K series	1.97	0.00664	34.70	0.23	51.42	SiO <sub>2</sub>	Yes	
P	K series	2.46	0.01376	19.30	0.12	14.77	GaP	Yes	
Cl	K series	0.36	0.00315	4.50	0.06	3.01	NaCl	Yes	
Ca	K series	2.17	0.01937	25.29	0.14	14.96	Wollastonite	Yes	
Fe	K series	0.73	0.00728	10.44	0.14	4.43	Fe	Yes	
Total:				100.00		100.00			

Chlorine is present in all the six samples. It can be due to several reason such as powder contamination, or more probably it is due to the atmosphere composition where the synthesis is performed. To avoid it and have a purer result, synthesis should be done in controlled atmosphere.

As a comparison compositional scanning of sample 2 – 800°C is reported in table 3.6 and visualized in fig. 3.45.

When compared to each other, both compositional results are coherent with the initial intentions in the synthesis process. In fact, sample 1 is characterized by the presence of more iron, almost double amount of it if compared to sample 2. In the same time, similar percentage of phosphorous and calcium are detected, this being coherent with the quantities of reactors used for the synthesis.

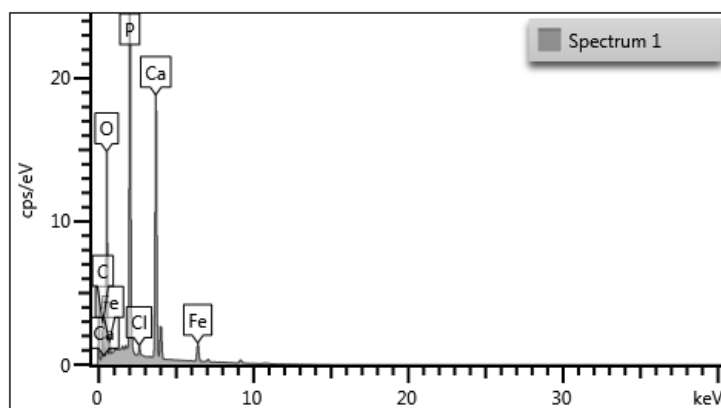


**Fig. 3.45** SEM-EDX analysis results for sample 2 – 800°C.

**Table 3.6** Results of composition scan performed with SEM on sample 2 – 800°C.

Element	Line Type	Apparent Concentration	k Ratio	Wt%	Wt% Sigma	Atomic %	Standard Label	Factory Standard	Standard Calibration Date
C	K series	0.13	0.00125	6.98	0.25	13.15	C Vit	Yes	
O	K series	2.11	0.00711	37.70	0.23	53.35	SiO <sub>2</sub>	Yes	
P	K series	2.55	0.01425	19.35	0.12	14.14	GaP	Yes	
Cl	K series	0.06	0.00054	0.75	0.04	0.48	NaCl	Yes	
Ca	K series	2.56	0.02284	28.85	0.15	16.30	Wollastonite	Yes	
Fe	K series	0.45	0.00454	6.37	0.11	2.58	Fe	Yes	
Total:				100.00		100.00			

In next paragraph cytotoxicity results are evaluated, understanding more about the biocompatibility of all powders synthesized.

### 3.6 Cytotoxicity test

To evaluate toxicity of powders, cytotoxicity test has been carried out, checking how toxic synthesized materials are when in contact with Vero cells.

As stated before in **Material and Methods** chapter resazurin and resofurin need to be measured for this purpose. In fact, amount of resazurin converted is an indication of the quantity of viable cells present in the considered well.

Cell viability (as shown in equation 3.3) is calculated proportionate to the control sample C- through the ratio between the amount of converted resazurin in each well and the amount of resazurin converted in control sample C-.

$$\text{Cell viability} = \frac{(D_{570}-D_{600})-(D_{MC570}-D_{MC600})}{(D_{C-570}-D_{C-600})-(D_{MC570}-D_{MC600})} * 100 \quad \text{Equation 3.3}$$

Where D represents the absorbance at the indicated wavelength, while MC refers to the control medium.

5 replica of each sample has been tested, in order to have a statistical analysis of the result.

For each replica  $(D_{570}-D_{600})$  is calculated and starting from that the relative standard deviation  $\sigma$ . The same process is applied for all replica of medium control and for control sample C-. Standard deviation  $\sigma_{C-}$  and  $\sigma_{MC}$  are calculated in this way.

Finally, it is possible to calculate the uncertainty associated to the measures performed, using equation 3.4.

$$\Delta = \sqrt{\sigma^2 + \sigma_{MC}^2} \quad \text{Equation 3.4}$$

Applying equation 3.4 it is possible to build the graphic visualized in fig. 3.46.

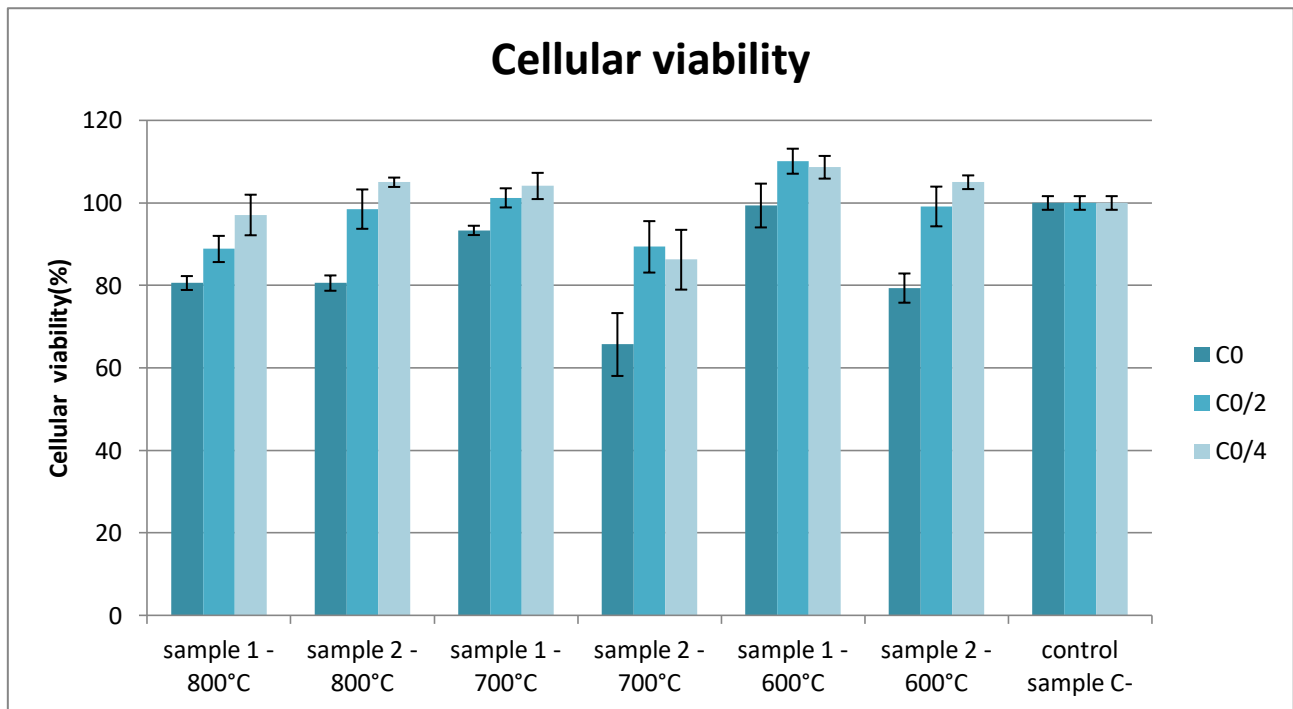


Fig 3.46 Cellular viability calculated for each sample at 3 different powder concentration in the medium.

Error lines present in the graphic are calculated through equation 3.5.

Some considerations can be done about the information in the graphic. Firstly, by observing sample 1, the one with a bigger amount of iron, cell viability increases when sintering temperature decreases. From this it can be supposed that increasing sintering temperature new compounds formed that increase toxicity of the powders.

For what concern all sample 2, apparently there is an oscillating behaviour in increasing sintering temperature.

Sample 2 -700°C is quite critic, showing a cellular viability of just 60%, this bring quite low and for this reason that powder can be classified as quite toxic.

Moreover, sample 2 – 700°C shows small compatibility as it has been seen analysing SEM images. It is therefore possible to conclude that the least biocompatible of all the powders prepared is sample – 700°C.

By looking at the results displayed in fig.3.46, it appears that comparing toxicity registered for sample 1, it is always higher than its counterpart treated at the same temperature with composition 2.

Therefore, it can be concluded that samples 1 present generally lower toxicity when compared to samples with composition 2.

This, together with lower bioactivity shown in SEM analysis, leads to the conclusion that in general samples 1 is more biocompatible than samples 2. Finally, it seems that to higher amount of iron inside hydroxyapatite is associated higher biocompatibility as it is confirmed in literature as well [71].

## 4. Conclusions

In several studies has been investigated the possibility to use iron doped hydroxyapatite, synthesized in different ways, in magnetic hyperthermia application.

It is proved that Fe-hydroxyapatite shows magnetic behaviour and in particular for this application the requirement is the synthesis of HAp in the form of nanoparticle, in order to show superparamagnetic behaviour. This kind of material has been proved to show magnetic activity in presence of an external alternating field, heating up till the temperature of 43° needed to kill cancer cells preserving alive the viable ones. For example, *Hou et al.* [46] have achieved great results in vivo application of magnetic hydroxyapatite nanoparticles on mice, reducing consistently the amount of cancer cells in 15 days of treatment. In this case particles have been produced through a co-precipitation process, adding just Fe<sup>3+</sup> ions.

Changing the synthesis process can heavily influenced final properties of the material and for this reason implementing a sol-gel process able to offer the same result as the precipitation process, microwave assisted process or other (which in general are more expensive and complicate) is not always easy.

The principal goal of the dissertation was to create Fe-doped hydroxyapatite nanoparticles able to show super-paramagnetic behaviour, using a simple and easily controlled sol-gel process.

Six samples have been prepared, starting from two different composition and 3 different sintering process have been applied. In fact, it has been used 600°C, 700°C ad 800°C as sintering temperature. After that, all powders have been deeply analysed, with the objective to understand how different composition combine with different thermal process can influence hydroxyapatite structure and consequently its final properties.

Besides of all characterization analyses to understand as more as possible about powder composition and structure, also biocompatible tests were performed. This being critical aspect in producing material supposed to stay close in contact with human body.

Very different results can be found in literature, since the synthesis process and the change in some parameters can heavily affect final properties. This is also clear in the case of this project, as interesting and not negligible differences show up just changing sintering temperature, time range of processes and quantity of iron used for the doping process.

In this way, material with different composition, different structure (interesting is how much lattice parameters vary changing few synthesis conditions) and consequently different magnetic behaviour and biocompatibility.

Indeed, very interesting is what happens with samples of composition 2 sintered at 3 different temperature. In fact, even though sample 2-600°C and sample 2-700°C don't show magnetic behaviour, the one sintered at 800°C is the most promising material in this sense, showing the highest increase in temperature when hyperthermia test is applied on it among all samples synthesized.

As process parameters can heavily affect final properties, it is interesting for future studies to evaluate how changing some of the conditions could affect them.

For example, one important change it would be performing synthesis inside controlled atmosphere, this reducing the risk of formation of residual hematite due to the combination between iron and oxygen provided by the environment. In the same way it can reduce the amount of chlorine incorporated inside hydroxyapatite, reducing in this way the formation of residual chlorine in powders, which could determine the formation of cloroapatite as well.

It could therefore be useful a specific future investigation on the crystalline structure deeply, using *Rietveld analysis* and Mossbauer spectrometry. It is in fact very important to understand how different amount of doping and sintering temperature could affect more precisely crystalline

structure. This would provide a better understanding of how doping affect structure and consequently final properties.

In this work, sol-gel process has been carried out without an ageing phase.

Moreover, it would be interesting to analyse in future studies how different ageing time performed on iron doped hydroxyapatite could affect the final sintered materials. In fact, it is a kind of condition that is not usually investigated in scientific researches as few examples can be found in literature.

It is interesting to notice that in this work has been proved that increasing the amount of iron incorporated inside hydroxyapatite can clearly increase biocompatibility of powders. This resulting from the toxicity evaluation of powders, where samples with more iron show less toxicity. Moreover, SEM images show the higher bioactivity of samples 1, which have incorporated more iron in their structure.

This final statement can be very useful also for other applications in which iron doped hydroxyapatite can be applied when in contact with human body and not just in cancer treatments. For instance, it can be used in drug delivery application, where biocompatibility is a crucial requirement.

Finally, none of the samples shows an increment in temperature big enough to be applied in cancer cell treatment when the test is performed in a timeframe of 10 minutes and with the chosen concentration of powders. However, by using bigger concentration and/or higher timeframe, the desired result might be obtained. It would be interesting for future investigations to go deeper into this kind of analyses, specifically in the cases of samples sintered in this project. In fact, all of them appear to present paramagnetic and/or super-paramagnetic behaviour. So the main goal of this project has been reached: iron-doped hydroxyapatite showing super-paramagnetic behaviour has been synthesized. This setting an important starting point for future investigations with the aim of sharpen the synthesis process, making it better-balanced.

Next goal, it should be trying to improve magnetic behaviour of the sintered powders keeping them bioactive as shows in this work.

Moreover, this innovative material is one of the most interesting material for future development in super-paramagnetic material for biocompatible applications.

## Bibliography

- [1] F-Fluoride PET/CT and Tc-MDP SPECT/CT can detect bone cancer at early stage in rodents Christiano R.R. Alvesa , Daniele de P. Fariac , Camila de G. Carneiroc , Alexandre T. Garcez , Vanessa P. Gutierrezd , Willian das Nevesa , Ney R. de Almeidaa , Yara Curyd , Roger Chammasc , Patricia C. Bruma, Life science (2018).
- [2] Magnetic nanoparticle-based hyperthermia for cancer treatment Manuel Banobre-López, Antonio Teijeiro, Jose Rivas, reports of practical oncology and radiotherapy 18 (2013).
- [3] Breast cancer bone metastases: pathogenesis and therapeutic targets, Naomi Brooka, Emily Brooka, Arun Dharmarajana , Crispin R. Dassa, Arlene Chanc, International Journal of Biochemistry and Cell Biology 96 (2018) 63–78.
- [4] Bone structure and metabolism, Stuart H Ralston, Medicine Volume 45, Issue 9, September 2017, Pages 560-564.
- [5] <https://boneandspine.com/cortical-bone-and-cancellous-bone/>
- [6] <https://biologydictionary.net/spongy-bone/>
- [7 ] Calcium Orthophosphate-Based Bioceramics, Sergey V. Dorozhkin, September 2013.
- [8] D. Belluci, A. Sola, M. Gazzarri, F. Chiellini, V. Cannillo, A new hydroxyapatite based biocomposite for bone replacement, Mater. Sci. Eng. C 33 (2013) 1091 e 1101.
- [9] M. Jiang, J. Terra, A. M. Rossi, et al., “Fe<sup>2+</sup>/Fe<sup>3+</sup> substitution in hydroxyapatite: Theory and experiment,” Am. Phys. Soc., vol. 66, p. 224107, 2002.
- [10] T. Batista and J. Santos-Filho, Hidroxiapatita e  $\beta$ -Fosfato Tricálcio como absorvedores do ultravioleta, 1st ed. Sergipe: Instituto Federal de Sergipe, 2016.
- [11] <https://search.proquest.com/openview/3f421c3e66961b3e8cc957da6013b548/1?pq-origsite=gscholar&cbl=18750&diss=y>
- [12] João Paulo Borges, Slides from biomaterial course, University NOVA of Lisbon, academic year 2017/2018.
- [13] H. Zhou and J. Lee, “Nanoscale hydroxyapatite particles for bone tissue engineering,” Acta Biomater., vol. 7, pp. 2769–2781, 2011.
- [14] Prolonged local antibiotics delivery from hydroxyapatite functionalised with cyclodextrin polymers, Stephane Lepretre , Feng Chai , Jean-Christophe Hornez , Guillaume Vermet , Christel Neut ,nMichel Descamps , Hartmut F. Hildebrand , Bernard Martel , Biomaterials 30 (2009) 6086–6093.
- [15] Sugar-decorated hydroxyapatite: an inorganic material bioactivated with carbohydrates Laura Russo , Elena Landi , Anna Tampieri , Antonino Natalello , Silvia M. Doglia , Luca Gabrielli , Laura Cipolla , Francesco Nicotra , Carbohydrate Research 346 (2011) 1564–1568.

- [16] Evaluation and characterization of nanostructure hydroxyapatite powder prepared by simple sol–gel method, M.H. Fathi, A. Hanifi, *Materials Letters* 61 (2007) 3978–3983.
- [17] Bio-inspired hydroxyapatite dual core-shell structure for bone substitutes ,Shaan Chamary, Dominique Hautcoeur, Jean-Christophe Hornez, Anne Leriche, Francis Cambier, *Journal of the European Ceramic Society* 37 (2017) 5321–5327.
- [18] Polymer-assisted synthesis of hydroxyapatite nanoparticle, Yao-Hsuan Tseng, Chien-Sheng Kuo, Yuan-Yao Li, Chin-Pao Huang, *Materials Science and Engineering C* 29 (2009) 819–822.
- [19] <https://www.ncbi.nlm.nih.gov/pmc/articles/PMC3458931/>
- [20] Wet chemical precipitation synthesis of hydroxyapatite (HA) powders, Azade Yelten-Yilmaz, Suat Yilmaz, *Ceramics International* 44 (2018) 9703–9710.
- [21] Combined precipitation and spray drying for the synthesis of hydroxyapatite nanopowders as soft spherical granules, Ömer Yıldız, *ceramic international*.
- [22] Effect of Different Calcium Precursors on Biomimetic Hydroxyapatite Powder Properties, A. Karakaş, A.B. Hazar Yoruç, D. Ceylan Erdoğan, M. Doğan, *ACTA PHYSICA POLONICA A* Vol. 121 (2012).
- [23] Formation and Characterization of Hydroxyapatite Coating Prepared by Pulsed Electrochemical Deposition, Jia Linan, Liang Chenghao, Huang Naibao, Duan Feng, Wang Lixia, *Rare Metal Materials and Engineering*, 2015, 44(3): 0592-0598.
- [24] Influence of deposition temperature on the properties of hydroxyapatite obtained by electrochemical assisted deposition, Cosmin M. Cotrut, Alina Vladescu, Mihaela Dinu, Diana M. Vranceanu, *Ceramics International* Volume 44, Issue 1, January 2018, Pages 669-677.
- [25] [https://www.uio.no/studier/emner/matnat/kjemi/KJM5100/h06/undervisningsmateriale/10KJM5100\\_2006\\_sol\\_gel\\_d.pdf](https://www.uio.no/studier/emner/matnat/kjemi/KJM5100/h06/undervisningsmateriale/10KJM5100_2006_sol_gel_d.pdf)
- [26] Comparative analysis of hydroxyapatite synthesized by sol-gel, ultrasonication and microwave assisted technique, Sidra Waheed , Misbah Sultan, Tahir Jamil, Tousif Hussain, *Materials Today: Proceedings* 2 ( 2015 ) 5477 – 5484.
- [27] Nanotechnology and Nanomedicine: Start small, think big Saeid Kargozar, Masoud Mozafari, *Materials Today: Proceedings* 5 (2018) 15492–15500.
- [28] Valentina Cauda, Slides from ‘introduction to nanotechnologies’ course, Polytechnic university of Turin, academic year 2015/2016.
- [29] Analytical Nanoscience and Nanotechnology: Where we are and where we are heading, María Laura Soriano, Mohammed Zougagh, Miguel Valcárcel, Ángel Ríose, *Talanta* 177 (2018) 104–121.
- [30] magnetism and magnetic materials, J.M.D Coey, 2009.
- [31] <https://nptel.ac.in/courses/113106032/15%20-%20Magnetic%20Properties.pdf>
- [32] <http://www.chimica.unipd.it/fabrizio.mancin/pubblica/Galileiana/VI%20lezione.pdf>

- [33] <http://mriquestions.com/what-is-ferromagnetism.html>
- [34] <http://www.physics-and-radio-electronics.com/physics/magnetism/ferrimagnetism.html>
- [35] [https://en.wikibooks.org/wiki/Introduction\\_to\\_Inorganic\\_Chemistry/Metals\\_and\\_Alloys:\\_Structure,\\_Bonding,\\_Electronic\\_and\\_Magnetic\\_Properties](https://en.wikibooks.org/wiki/Introduction_to_Inorganic_Chemistry/Metals_and_Alloys:_Structure,_Bonding,_Electronic_and_Magnetic_Properties)
- [36] Superparamagnetism : Theory and Applications - Discussion of Two Papers on Magnetic Nanoparticles, Manuel Benz, December 14, 2012.
- [37] E. Francisquini, J. Schoenmaker, and J. A. Souza, “Nanopartículas Magnéticas e suas Aplicações,” in *Química Supramolecular e Nanotecnologia*, 1st ed., W. A. Alves, Ed. São Paulo: Atheneu, 2014, pp. 269–288.
- [38] [http://www.ifmpan.poznan.pl/~urbaniak/Wyklady2012/urbifmpan2012lect6\\_04.pdf](http://www.ifmpan.poznan.pl/~urbaniak/Wyklady2012/urbifmpan2012lect6_04.pdf)
- [39] <https://www.accessscience.com/content/langevin-function/370300>
- [40] HEATING OF SUPERPARAMAGNETIC COLLOID IN HIGH-FREQUENCY MAGNETIC FIELD: IMPLICATIONS FOR ELECTROMAGNETIC HYPERTHERMIA, M. BABINCOV, E. USTEKOV, P. BABINEC, P. CIMANEC, V. CRACIUN, D. LESZCZYNSKA, 21 March 2000.
- [41] The role of dipole interactions in hyperthermia heating colloidal clusters of densely-packed superparamagnetic nanoparticles, Rong Fu, Yuying Yan, Clive Roberts, Zeyu Liu & Yiyi Chen, *Scientific Reports* volume 8, Article number: 4704 (2018).
- [42] Investigation of Brownian and Néel relaxation in magnetic fluids, R. Kötitz, W. Weitschies, L. Trahms, W. Semmler, *Journal of Magnetism and Magnetic Materials* Volume 201, Issues 1–3, July 1999, Pages 102–104.
- [43] SUPERPARAMAGNETIC IRON OXIDE NANOPARTICLE HEATING: A BASIC TUTORIAL M.L. Etheridge, N. Manucherabadi, R. Franklin J.C. Bischof, 2011.
- [44] Preparation and characterization of an iron oxide-hydroxyapatite nanocomposite for potential bone cancer therapy, Murugesan Sneha, Nachiappan Meenakshi Sundaram, 2015.
- [45] Intrinsically superparamagnetic Fe-hydroxyapatite nanoparticles positively influence osteoblast-like cell behaviour, Silvia Panseri, Carla Cunha, Teresa D’Alessandro, Monica Sandri, Gianluca Giavaresi, Maurilio Marcacci, Clark T Hung and Anna Tampieri, *Journal of Nanobiotechnology* 2012.
- [46] The in vivo performance of biomagnetic hydroxyapatite nanoparticles in cancer hyperthermia therapy, Chun-Han Hou, Sheng-Mou Hou, Yu-Sheng Hsueh, Jinn Lin, Hsi-Chin Wu, Feng-Huei Lin, *Biomaterials* 30 (2009) 3956–3960.
- [47] Intrinsic magnetism and hyperthermia in bioactive Fe-doped hydroxyapatite, Anna Tampieri, Teresa D’Alessandro, Monica Sandri, Simone Sprio, Elena Landi, Luca Bertinetti, Silvia Panseri, Giancarlo Pepponi, Joerg Goettlicher, Manuel Bañobre-López, Jose Rivas, *Acta Biomaterialia* 8 (2012) 843–851.

- [48] Impact of magnetic field on the mineralization of iron doped calcium phosphates, Baskar S., Ramana Ramya J., Thanigai Arul K., Nivethaa E.A.K., Mahadevan Pillai V.P., Narayana Kalkura S., *Materials Chemistry and Physics* 218 (2018) 166–171.
- [49] Fe<sup>2+</sup>/Fe<sup>3+</sup> substitution in hydroxyapatite: Theory and experiment, Ming Jiang, J. Terra, A. M. Rossi, M. A. Morales, E. M. Baggio Saitovitch and D. E. Ellis, *PHYSICAL REVIEW B* 66, 224107 - 2002.
- [49] Atomic scale modeling of iron-doped biphasic calcium phosphate bioceramics Sandrine Gomes, Amandeep Kaur, Jean-Marc Grenèche, Jean-Marie Nedelec, Guillaume Renaudin, *Acta Biomaterialia* 50 (2017) 78–88.
- [50] Effect of cation doping on the structure of hydroxyapatite and the mechanism of defluoridation Zhenzhen Chen, Yiling Liu, Lianzhen Mao, Lianyuan Gong, Wenjin Sun, Li Feng, *Ceramics International* 44 (2018) 6002–6009.
- [51] A simple sol–gel technique for preparing hydroxyapatite nanopowders, Wang Fenga, Li Musesa, Lu Yu-peng, Qi Yong-xin, *Materials Letters* 59 (2005) 916– 919.
- [52] [https://chem.libretexts.org/Textbook\\_Maps/Physical\\_and\\_Theoretical\\_Chemistry\\_Textbook\\_Maps/Supplemental\\_Modules\\_\(Physical\\_and\\_Theoretical\\_Chemistry\)/Spectroscopy/Vibrational\\_Spectroscopy/Infrared\\_Spectroscopy/How\\_an\\_FTIR\\_Spectrometer\\_Operates](https://chem.libretexts.org/Textbook_Maps/Physical_and_Theoretical_Chemistry_Textbook_Maps/Supplemental_Modules_(Physical_and_Theoretical_Chemistry)/Spectroscopy/Vibrational_Spectroscopy/Infrared_Spectroscopy/How_an_FTIR_Spectrometer_Operates)
- [53] Slides from the course “fundamentals of organic chemistry”, Roberta Bongiovanni, Politecnico di Torino, 2015.
- [54] Vibrating Sample Magnetometry: Analysis and Construction, Syed Alamdar Hussain Shah, Friday, December, 13, 2013.
- [55] Sigma, “Fundamental techniques in cell culture”, Sigma-Aldrich, 2018.
- [56] Cell Viability Assays, Riss TL, Moravec RA, Niles AL, Duellman S, Benink HA, Worzella TJ, Minor L, Assay Guidance Manual [Internet]. Bethesda (MD): Eli Lilly & Company and the National Center for Advancing Translational Sciences; 2004-2013 May 1 [updated 2016 Jul 1].
- [57] Slides from the course “Tissue engineering”, University NOVA of Lisbon, 2018.
- [58] Modelling the Crystal Structure of a 30 nm Sized Particle based Hydroxyapatite Powder Synthesised under the Influence of Ultrasound Irradiation from X-ray powder Diffraction Data, Ravi Krishna Brundavanam, G errard Eddy Jai Poinern, Derek Fawcett, *American Journal of Materials Science* 2013, 3(4): 84-90.
- [59] The influence of Ca/P ratio on the properties of hydroxyapatite bioceramics, S. Ramesh, C. Y. Tan, M. Hamdi, I. Sopyan, W. D. Teng, Jan 06, 2014.
- [60] Effect of Thermal Treatment of the Hydroxyapatite Powders on the Micropore and Microstructure of Porous Biphasic Calcium Phosphate Composite Granules, David S. H. Lee, Yuni Pai, Steve Chang, *Journal of Biomaterials and Nanobiotechnology*, 2013, 4, 114-118.
- [61] Kinetics of the CaO/Ca(OH)<sub>2</sub> hydration/dehydration reaction for thermochemical energy storage applications Yolanda A. Criado, M onica Alonso, J. Carlos Abanades, Instituto Nacional del Carb on, CSIC-INCAR, C/ Francisco Pintado Fe, 26, 33011, Oviedo. Spain.

- [62] Preparation and bioactivity evaluation of bone-like hydroxyapatite nanopowder, M.H.Fathi, A.Hanifi, V.Mortazavi, *Journal of Materials Processing Technology*, Volume 202, Issues 1–3, 20 June 2008, Pages 536-542.
- [63] Synthesis and characterization of iron-doped/substituted calcium hydroxyapatite from seashells *Macoma balthica* (L.), Juste Trinkunaite-Felsen, Aleksandra Prichodko, Miroslav Semasko, Ramunas Skaudzius, Aldona Beganskiene, Aivaras Kareiva, *Advanced Powder Technology* 26 (2015) 1287–1293
- [64] Dielectric properties of Fe doped hydroxyapatite prepared by sol–gel method, Omer Kaygili, Sergey V. Dorozhkin, Tankut Ates, Ahmed A. Al-Ghamdi, Fahrettin Yakuphanoglu, *Ceramics International* 40 (2014) 9395–9402.
- [65] The Crystal Chemistry of Ferric Oxyhydroxyapatite, H. R. Low, N. Phonthammachai, A. Maignan, G. A. Stewart, T. J. Bastow, L. L. Ma and T. J. White, *Inorg.Chem.*, 2008, 47 (24), pp 11774–11782.
- [66] Combined X-ray and neutron diffraction, Rietveld refinement in iron-substituted nano-hydroxyapatite, A. Kyriacou, Th. Leventouri, B. C. Chakoumakos, V. O. Garlea, C. B. dela Cruz, A. J. Rondinone & K. D. Sorge, *J Mater Sci* (2013) 48:3535-3545.
- [67] Research of Calcium Phosphates Using Fourier Transform Infrared Spectroscopy, Liga Berzina-Cimdina and Natalija Borodajenko, Riga Technical University, Institute of General Chemical Engineering, Latvia.
- [68] Zirconia/Hydroxyapatite Composites Synthesized Via Sol-Gel: Influence of Hydroxyapatite Content and Heating on Their Biological Properties, Flavia Bollino 1, Emilia Armenia 2 and Elisabetta Tranquillo 1, 5 July 2017.
- [69] Synthesis and characterization of nano-hydroxyapatite (n-HAp) using the wet chemical technique, Arunseshan Chandrasekaran, Sagadevan Suresh, Arivuoli Dakshanamoorthy, August 2013.
- [70] Evolution of the influence of electrical polarization on the bioactivity of hydroxyapatite nanopowders, Barros bernardo, Brachetti Enrico, Mesturino Fabio, Monteiro Carlos, *Faculdade de Ciencia e Tecnologia, Universidade NOVA de Lisboa*, 2017.
- [71] In Vitro Study of Iron Doped Hydroxyapatite, Khairy Mohamed Tohamy Ereiba, A. G. Mostafa, G. A. Gamal, A. H. Said, 5 September 2013.
- [72] Abbas Fahami, Gary W. Beall, Tania Betancourt, Synthesis, bioactivity and zeta potential investigations of chlorine and fluorine substituted hydroxyapatite, *Materials Science and Engineering C* 59 (2016) 78–85.
- [73] [http://shodhganga.inflibnet.ac.in/bitstream/10603/93513/11/11\\_chapter6.pdf](http://shodhganga.inflibnet.ac.in/bitstream/10603/93513/11/11_chapter6.pdf)
- [74] Blood Compatibility of Iron-Doped Nanosize Hydroxyapatite and Its Drug Release,

V. Sarath Chandra, Ganga Baskar, R. V. Suganthi, K. Elayaraja, M. I. Ahymah Joshy, W. Sofi Beaula, R. Mythili, Ganesh Venkatraman and S. Narayana Kalkura, *ACS Appl. Mater. Interfaces*, 2012, 4 (3), pp 1200–1210.

[75] A novel biomagnetic nanoparticle based on hydroxyapatite, Hsi-Chin Wu, Tzu-Wei Wang, Jui-Sheng Sun, Wen-Hsi Wang and Feng-Huei Lin, 23 March 2007.

[76] Abridged acid–base wet–milling synthesis of high purity hydroxyapatite, Sandi Carolina Ruiz–Mendoza, Luis Carlos Moreno–Aldana, Edgar Delgado–Mejía, *Mat. Res.* vol.11 no.2 São Carlos Apr./June 2008